University of Southampton

# Numerical Modelling and Stability Analysis of Convective Flows In Weld Pools

by

Anthony William Belgrove

Doctor of Philosophy

Faculty of Mathematical Studies

March 1996

One must still have chaos in one to give birth to a dancing star

-Nietzsche

UNIVERSITY OF SOUTHAMPTON

## ABSTRACT

FACULTY OF MATHEMATICAL STUDIES

Doctor of Philosophy

# NUMERICAL MODELLING AND STABILITY ANALYSIS OF CONVECTIVE FLOWS IN WELD POOLS

By Anthony William Belgrove

In arc welding electromagnetic forces were traditionally thought to be the major cause of fluid motion in the weld pool. Experiments have shown, however, that under some circumstances the surface tension forces can produce a radically different flow pattern from that produced by electromagnetic forces only. Additionally, it is now known that the magnitude of the surface tension gradient with respect to temperature can vary greatly, even changing sign, with the addition into the metal of very small amounts of impurities. As a consequence of these observations the axisymmetic motion of a semi-infinite region of fluid is investigated in this thesis, under the action of the electromagnetic and surface tension forces arising from coincident point sources of heat and current. A similarity solution can be obtained in this case and the resulting ordinary differential equations are solved numerically. Results indicate that when the surface tension gradient is large, but still within the experimentally obtained range, it dominates the flow for most values of the applied current. However, flow breakdown caused by the velocity down the axis of symmetry becoming infinite, which has been a problem with a similar model containing the electromagnetic force only, still occurs. It is shown that the value of the current at which this happens can be altered by several orders of magnitude through changing the magnitude and sign of the surface tension gradient.

Under certain experimental conditions the spontaneous rotation of the molten metal in the weld pool when the current is increased has been observed. In addition some 'hysteresis' effects have been noticed when making measurements of the weld pool size. These observations suggest the possible occurrence of flow bifurcation and the existence of multiple steady-state solutions. To investigate these possibilities a very small azimuthal component is added to the electromagnetic force considered in the previous model and, on approaching the expected flow breakdown, it is found that the azimuthal velocity of the fluid increases sufficiently to prevent the appearance of the infinite velocity down the axis.

Next an axisymmetric solution in a finite region is considered, with the coupled fluid and heat flow in a hemisphere being investigated. The fluid motion is induced by the electromagnetic, surface tension and buoyancy forces, due to coincident point sources of heat and current. A set of coupled partial differential equations are obtained, which are then solved using a finite difference method, and the effect of the three forces on the fluid flow is examined. Finally, a linear stability analysis of these solutions subjected to a three-dimensional perturbation is investigated numerically.

# Table of Contents

# Acknowledgements

I would like to thank Dr. R.E. Craine and Dr. D.R.J. Chillingworth for their supervision of this thesis, particularly for finding typing errors in large programs.

I am indebted to the Science and Engineering Research Council and Nuclear Electric for the award of a CASE studentship.

# Chapter 1: Introduction

Welding is a process which joins two materials, by fusing them together at their surfaces, and is used in the construction of a great many items, eg. bridges, cars and nuclear power stations. In the USA welding is utilised in 50% of industrial, commercial and consumer products that make up the GNP [ 3 ]. Several methods are used to perform the welding, including the use of gas torches, electric arcs, electron beams and lasers . With increasing mass production, a reliable method of predicting the quality of the weld would be very useful in industry, rather than having to rely on the judgement of skilled craftsmen. This objective has started off a train of research into welding processes. In particular much attention has been paid to TIG (Tungsten electrode with an Inert Gas shield) welding, since its use is quite widespread, especially in automatic welding processes.

In TIG welding a high current electric arc is struck between a tungsten electrode and the two workpieces that are to be joined. The tungsten electrode is non-consumable, whereas using a different metal can provide a steady flow of molten drops into the weld. The electric arc produces a strong source of heat sufficient to melt the workpieces in a small pool under the electrode. The electrode is traversed along the edges of the materials to make a complete join. To produce a strong weld the weld pool has to penetrate all the way through the workpieces and be of sufficient size on the backface to produce a good join. The penetration can be controlled by altering the current in the arc, and hence the heat input, and the rate of traversal of the electrode.

A method for predicting the size and shape of the weld pool in the TIG welding process would be of great use in ensuring that strong welds are produced first time, without lengthy and costly experimental work.

Recently research has been carried out into computer control of arc welding using high speed cameras, image processing and neural networks, to measure the size and shape of the weld pool surface in real-time, and hence determine the overall shape of the weld pool [ 8 ], [ 56 ], [ 78 ].

The first attempt at modelling the welding process was made by Rosenthal [ 88 ], [ 89 ], who constructed an analytical solution for the heat flow due to a point source of heat traversing the surface of a semi-infinite block of material. Extensions of this work to finite plates and including latent heat of fusion at the solid-liquid boundary, distributed heat sources, surface heat loss due to convection and radiation, and temperature dependent thermal properties have been carried out by many authors, and good predictions have been made for the case of welding thin plates [ 36 ], [ 47 ], [ 54 ], [ 64 ], [ 92 ], [ 105 ].

Experimental evidence, however, indicates the presence of motion in the weld pool [ 14 ], [ 15 ], [ 113 ]. When convection becomes the dominant means of heat transfer, the fluid flow can affect the temperature distribution and hence the shape of the weld pool. This occurs when the Peclet number

$$P_e = \frac{\rho v L c_p}{\kappa}$$

is in the region of 10 or more, where $\rho$ is the density, v the velocity, L is a typical length, $c_p$ the specific heat and $\kappa$ the thermal conductivity. When arc-welding steel the values of Pe can range from about 10 to over 1000, so convection will normally dominate over conduction in determining the temperature distribution. Mills [ 68 ], [ 69 ] showed this to be the case in practice, when he spectroscopically measured the temperature distribution in an arc during a series of welds, and measured the depth to width ratio of the resulting welds. He observed that the depth to width ratio could change by up to 80%, without the temperature distribution measured in the arc changing significantly.

Experimental results published by Woods and Milner [ 113 ] show the complicated flows that can exist under a variety of welding conditions. They performed experiments where a drop of dissimilar metal was added to a weld pool, which was then left to mix for a few seconds (between 5 and 20 depending on the metals and method used). The resulting solidified weld was then examined to check the homogeneity of the metal mix, giving an indication of the strength of the fluid motion and the patterns of material differences which are caused by the fluid motion. Comparison between arc and oxyacetylene welding methods showed that in all cases arc welding produced substantially more mixing than with a torch. This implies that the fluid flow is much more vigorous when using the electric arc. The major difference in the forces acting in the two methods is the electromagnetic force produced during arc welding.

Woods and Milner then investigated the possible effect of the arc pressure on the flow by blowing a jet of nitrogen on to the surface of a heated pool, so that it produced the same pressure distribution as the plasma jet present in arc welding. Some mixing occurred, but considerably less than when using an electric arc. Woods and Milner also investigated the case with just a current present, by touching the surface of a weld pool with a 1cm diameter disk electrode, the size shown by Nestor [ 74 ] to be the one over which the majority of the current enters the weld pool when using a 1.2cm arc, the size used in their experiments. Rapid mixing was observed, in some cases more rapid than when using the arc, again showing the importance of the electromagnetic force in determining the flow in the weld pool.

Further, Woods and Milner observed the flows produced in thin sheets (0.075 in.) of various metals, and they were able to take pictures of the flow on the underside of the sheet. All the metals tested produced qualitatively similar results. At low currents (~30A) a double circulation was set up, which often rotated. As the current was increased this eventually gave way to a purely rotational flow. It was discovered that the metals that produced higher degrees of mixing in the previous experiments showed very rapid motion, with erratic changes in flow pattern. Iron and steel produced particularly intense flows, with a hot spot visible on the underside which rapidly changed shape and position, indicating the presence of a complicated, possibly turbulent, flow.

The motion present in the weld pool could come from one of the following mechanisms:

(1) The strong electric current will produce an electromotive (or Lorentz) force due to the interaction of the current with its own self-induced magnetic field or any imposed fields.

(2) The surface tension of a fluid will normally change as the temperature changes, and since there are large temperature gradients present in a weld pool, a significant (Marangoni) force could be produced on the top surface.

(3) The temperature differences in the fluid can cause changes in the density of the molten metal, and hence a buoyancy force could be produced when welding under gravity.

(4) The arc plasma jet and the surrounding gas flow could induce movement in the molten metal as they flow over the surface of the weld pool.

The Reynolds number

$$\mathrm{Re} = \frac{vL}{\nu}$$

gives a measure of the degree of turbulence in the flow, where $\nu$ is the kinematic viscosity. If the number is over about 2000, then the flow is likely to be turbulent. For TIG welding Re is often of order 100 and the flow is likely to be purely laminar, although for other types of welding, eg. submerged arc welding, this may not be the case.

Work on the effect of the Lorentz force on motion of the molten metal was started by Shercliff [ 94 ], who considered a point source of current discharging through a solid wall into a semi-infinite region of electrically conducting, inviscid fluid. However, this model caused the velocity field to be infinite down the axis of symmetry for all current values. Later, Sozou [ 97 ] studied a viscous fluid under the same conditions. This time the velocity field is finite everywhere for small values of a non-dimensional parameter K, but when the latter is increased to about 300, the velocity down the axis again becomes infinite. On considering the physical properties of molten steel, for instance, this critical value of K corresponds to a current of about 3.7 amps. This loss of solution existence has been observed in other conically similar flows, and was first mathematically proved in the interaction between a line vortex and a plane wall by Goldshtik [ 33 ] and studied more recently in [ 34 ], [ 35 ].

Narain and Uberoi [ 72 ], [ 73 ] modified the Shercliff and Sozou solutions to consider flow in a conical region, and Sozou and Pickering [ 102 ] investigated numerically the transient build-up of the steady problem solved by Sozou. In an attempt to increase the value of $K_{crit}$, Sozou and English [ 99 ] considered the problem of Sozou [ 97 ] but included the effect of the velocity on the electromagnetic field. The authors found that the back e.m.f. effect resulted in $K_{crit}$ becoming a monotonically increasing function of $\alpha = 4\pi\nu\sigma$, where $\sigma$ and $\nu$ are the electrical conductivity and the kinematic viscosity of the fluid respectively. If $\alpha > 1$ interaction effects are significant, whereas if $\alpha << 1$, which is the case in welding, then there is negligible coupling between the two effects.

Sozou [ 101 ] investigated the flow confined to a cone and a central column and found that $K_{crit}$ decreases as the angle of the cone in which the current is being discharged decreases.

The problem was placed into finite geometry by Sozou and Pickering [ 103 ], with a point source of current discharging into the centre of the plane free surface of a hemispherical bowl of incompressible, conducting fluid. The authors obtained an analytical solution to the linear slow viscous flow problem and a numerical solution for the full non-linear problem. As in the previous papers, a breakdown in the velocity field was found. In fact the authors were unable to get solutions for parameter values even as high as that found by Sozou earlier[ 97 ], reaching a value for K of only about 90, corresponding to about one amp.

The use of a point source for the input current arc is obviously physically incorrect since, in practice, the current entering the weld pool will be distributed over a significant region of the surface. Many authors have tried different models for the current input.

Andrews and Craine [ 4 ], [ 5 ] proposed a current distribution arising from a point source of current above the weld pool, and either a point, or ring, sink below. In this model, the current enters the weld pool over the entire free surface. The authors investigated the slow flow problem in a hemispherical bowl, and found a smooth analytical solution for the velocity field. The poloidal flows obtained revealed that the fluid could move up or down the axis of the pool, depending on the geometry of the current distribution. Typically for welding, their solution breaks down when the applied current exceeds 15A. Closer investigation of the source-sink model reveals that, for the parameters used, only about 10% of the current issuing from the point source actually enters the pool. The maximum current entering the pool for the solution of Andrews and Craine therefore appears little higher than that of Sozou and Pickering [ 103 ]. However, the breakdown of the two different solutions occurs for fundamentally different reasons. A singularity appearing in the velocity field causes the breakdown of the Sozou and Pickering solution, whereas the linearisation inherent in the Andrews and Craine solution becomes invalid as the current is increased.

Sozou and Pickering [ 104 ] also considered the flow in an oblate hemispheroidal bowl of equatorial radius a, with a disc source of current of radius k (where k<a). They obtained an analytical solution when the inertial terms in the governing Navier-Stokes equations are neglected, and displayed solutions for various values of a/k. However, on considering parameter values appropriate to the welding of steel, their solutions are again only valid for low currents.

The flow in a hemispheroidal bowl due to the current discharge from a disk electrode touching the surface of the fluid has been solved numerically by Sozou [ 101 ], Sozou and Pickering [ 104 ] and Ajayi, Sozou and Pickering [ 1 ]. It was observed that the larger the electrode the slower the flow that is produced, and the larger the current at which flow breakdown occurrs. This was attributed to the fact that with a larger electrode a greater portion of the electromagnetic force is irrotational, and as such it is balanced by the fluid pressure and does not cause any motion. Hence, a smaller proportion of the applied current drives the fluid flow. This argument provides one reason why the breakdown currents for the point source model are so low, since the entire force present there is rotational, and hence drives the fluid flow. In practice, of course, with finite electrode size, a proportion of the electromagnetic force will be irrotational, and hence will not drive the flow.

Bojarevics et al. [ 11 ] considered the flow in a hemisphere, where the current is provided by a smaller hemispherical electrode. Again they discovered that as the size of the electrode increases, the velocities decrease and solutions can be obtained at higher currents. Atthey [ 7 ] considered the flow in a hemisphere, with the current supplied by a

Gaussian distribution on the top surface. The fluid velocities obtained decreased when supplying more distributed current densities.

In practical terms none of these models precisely model the electric arc. The arc forms a bell shaped structure in welding, and figure 1.1 shows a plot of the isotherms present during practical arc welding [ 32 ]. There are experimental difficulties in obtaining the values of the current density in the arc under practical conditions, but measurements have been made using a water cooled copper electrode instead of a workpiece [ 38 ], [ 65 ]. The current distributions measured at the surface have been compared with appropriate Gaussian distributions, and show a marked difference in all cases, sometimes quite pronounced [ 63 ]. The structure of an electric arc is quite complicated, but several researchers have tried to model it. Published work shows some models have produced good correlations with experimental results under certain conditions [ 44 ], [ 65 ].

In all the modelling work mentioned earlier the surface of the weld pool is considered to be flat, which Lin and Eagar found to be the case for TIG welds with applied current of less than about 240A [ 62 ]. As the current increases from 240A to 300A the size of the

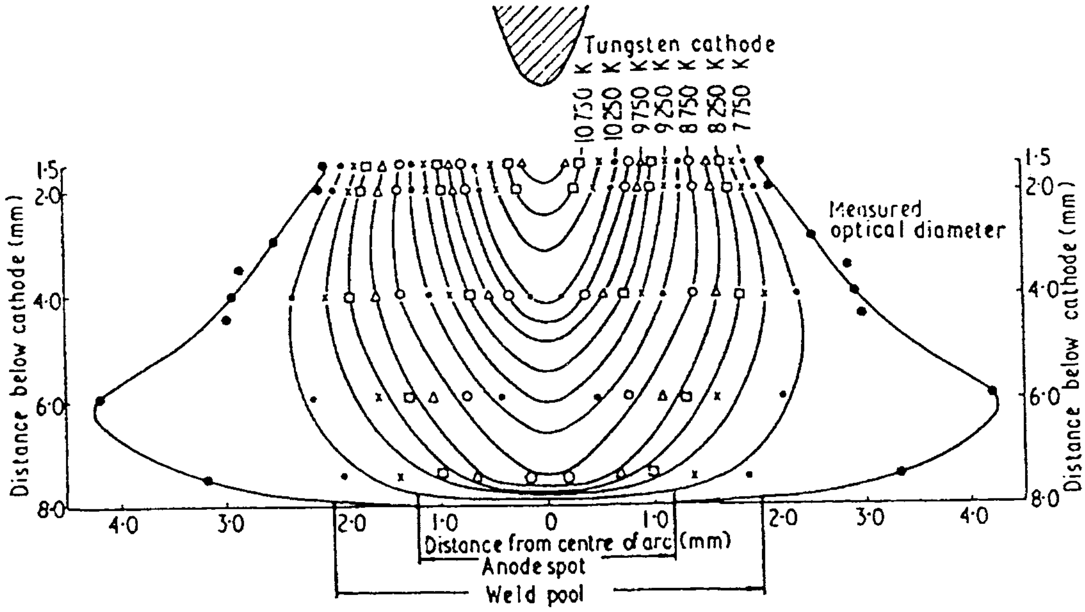

**Figure 1.1**- Isothermal map of a 100A GTA arc (from [ 32 ])

depression under the arc increases fivefold [ 87 ]. This could not have been produced by the pressure of the arc, which has been shown to increase parabolically with current [ 13 ] [ 37 ]. This indicates the possible existence of a bifurcation in the fluid velocity field.

Tsai and Kou [ 106 ] considered the effect on the free surface caused by the flow induced by electromagnetic forces. They considered two current distributions, a point source and a Gaussian distribution. With a point source a slight dip in the surface was caused at the origin, but when using a Gaussian distribution for the current a slight bump was caused at the origin. In both cases the deviation from a flat surface was only a few percent of the weld pool depth.

The importance of surface tension forces in TIG welding was first shown by Heiple and Roper [ 41 ], who examined the results of adding selenium or sulphur to a particular type of stainless steel (type 21-6-9). This steel produces weld pools which have a poor depth to width ratio, and possesses a negative surface tension gradient, which would be expected to produce an outward flow on the free surface. Keene et al [ 49 ] measured $\frac{\partial \gamma}{\partial T}$ for steels producing welds with both high and low depth to width ratios, and found values of $8*10^{-5}$ and $-3*10^{-4}$ respectively. Both sulphur and selenium are surface active, i.e. they tend to segregate preferentially on the surface of the weld pool. Since surface tension forces can depend on the makeup of the fluid at the surface, addition of the above elements to the metal can change the surface forces present. A positive surface tension gradient has been produced in molten iron by the addition of 40-60 ppm of sulphur, oxygen or selenium ( [ 2 ], [ 12 ], [ 29 ], [ 42 ], [ 43 ], [ 90 ] ) and the same was assumed to be the case for the steel examined by Heiple and Roper, as none of the alloying materials are particularly surface active. Figure 1.2 shows the variation of surface tension with temperature for two liquid steels. The data labelled "high d/w heat" is for material having approximately 160ppm more sulphur than for the material labelled "low d/w heat." The dashed lines illustrate proposed behaviour of the surface tension above the maximum temperature studied (from [ 12 ], data from [ 70 ]).

In Heiple and Roper's experiments, sulphur was added in the form of iron sulphide placed in small holes drilled in the surface of a block of steel. The distribution of oxide

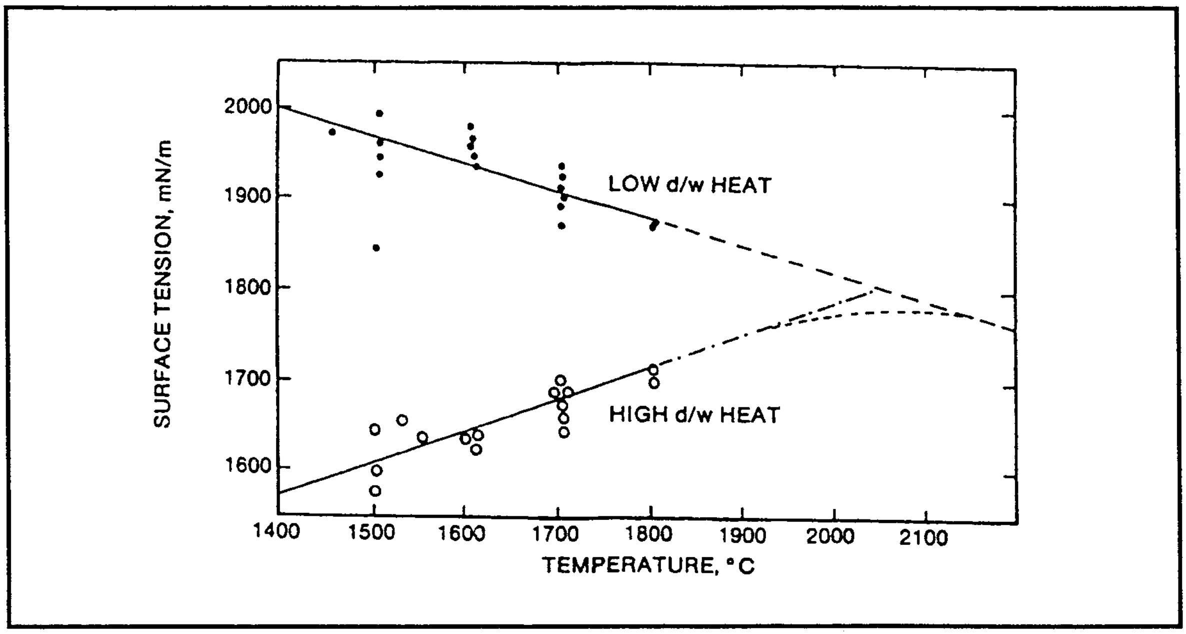

**Figure 1.2** - Surface tension verses temperature for two liquid steels [ 12 ], [ 70 ]

particles on the surface of the molten metal was observed to change from a ring around the outside of the weld pool, concomitant with a flow outward from the centre of the weld and producing a wide flat weld, to gathering in the centre of the pool, indicating an inward flow. In the latter case the weld formed was also deeper and narrower. More detailed results were obtained when adding small amounts of selenium (40-140ppm) in strips across a stainless steel plate. An arc was then traversed across the plate and a significant increase in depth to width ratio of up to 160% occurred in those strips. These changes could not be caused other than by a change in surface tension, and a resulting change in the flow direction from being outward on the surface to inward. Additionally, surface tension forces have been shown to be very important in determining the flow patterns in laser welds [ 16 ].

Lancaster [ 57 ] superimposed a spherically symmetric temperature distribution on to the semi-infinite problem of Sozou [ 97 ], and included the Marangoni surface tension forces. With this model he was able to calculate a non-dimensional quantity $\frac{A}{K} = -\frac{2\pi Q \frac{\partial \gamma}{\partial T}}{\mu_0 I^2 k}$

which determines the character of the flow. The symbols denote: Q the strength of the heat source, $\frac{\partial\gamma}{\partial T}$ the surface tension gradient with respect to temperature, $\mu_0$ the permeability of free space, I the applied current, and k the thermal conductivity. Lancaster argued that if A/K is less than (3-4ln2) convergent flow is produced, for (3-4ln2) < A/K < (2ln2-1) a double circulation occurs, and for A/K > (2ln2-1) a single divergent flow is produced. Various models suggest that when $\left|\frac{\partial\gamma}{\partial T}\right| = O\,(10^{-4})$ the surface tension forces produce higher surface velocities than electromagnetic forces associated with currents of 100-200A [ 24 ].

In Chapter 2 of this thesis an extension to Lancaster's model is presented. Since, as mentioned earlier, the Peclet number for arc welding steel indicates that the fluid flow affects the temperature distribution, a model for the arc welding process is presented in which the coupled solutions for both the temperature distribution and the velocity field are sought. A similarity solution is obtained for the stream function and the temperature in a semi-infinite region of electrically and thermally conducting material. A point source of heat and current is placed at the origin, and the fluid flow is determined under the action of the Lorentz and Marangoni forces only, for a range of values for the current and surface tension gradient.

The buoyancy force has been shown to be smaller than the electromagnetic forces [ 58 ], but Craine [ 20 ] determined that for a current of 50A buoyancy was strong enough to partially counter the effects of the electromagnetic forces. When present, buoyancy forces will tend to produce a wider shallower pool , and Kou and Sun [ 55 ] calculated a depth to width ratio of 0.344 for pure conduction and 0.326 on including buoyancy, for an arc current of 150A.

None of the above work included the possibility of an azimuthal component in the fluid velocity, although this has been shown to exist in some experiments. Bojarevics and Shcherbinin [ 10 ] investigated the flow in a hemispherical bowl of mercury under an electric current made by touching the surface of the pool with an electrode. They observed the flow of graphite particles scattered on the surface of the liquid, and discovered that with a positive electrode an inward flow could be produced at low currents, but as the current increased the fluid started to spin. With current supplied to the surface from below using a submerged electrode, the flow was outwards on the surface, and the authors were unable to observe any azimuthal flow.

Woods and Milner [ 113 ] performed an experiment with a similar hemispherical pool of mercury, where the current is tapped off on one side, perpendicular to the arc - often the case under practical welding conditions. They found that by altering the position of the bar taking the current from the pool, they could induce rotation in either direction, or produce no rotation at all.

Bojarevics and Scherbinin [ 10 ] and Bojarevics et. al. [ 11 ] looked at the semi-infinite problem of Sozou [ 97 ], but included a small azimuthal forcing term through the addition of a small applied meridional magnetic field. This extra force caused the fluid in the weld pool to rotate, hence causing an outward centrifugal force to oppose the Lorentz force. Bojarevics and Scherbinin discovered that on approaching the parameter value of K=300 (the value at which the Sozou solution broke down) the rotation of the weld pool increased, and the conflicting forces prevented the velocity becoming infinite down the axis. They also noticed that above a certain parameter value, as the size of the additional meridional magnetic field tended to zero, the azimuthal velocity did not approach zero. This suggests that a purely poloidal flow could be unstable to an azimuthal perturbation in the velocity.

In Chapter 3 of this thesis the model of Chapter 2 is extended by adding a small meridional component to the magnetic field, creating an azimuthal force, and therefore an azimuthal velocity. Solutions will be obtained with current values above the point where flow breakdown occurs without the azimuthal force in Chapter 2.

In Chapter 4 the problem from Chapter 2 is placed in a confined geometry, a hemisphere. The forces included are the Lorentz force, the Marangoni force and, additionally, buoyancy. The situation investigated is axisymmetric, with no azimuthal force present.

One of the fundamental problems concerning experimentalists and welding practitioners alike , is the non-repeatability of the welding process. Under apparently identical welding conditions, measurable parameters which characterise a finished weld show significant deviations from experiment to experiment. To be more precise the standard deviation of a given parameter is significantly large. A criterion, described by Willgoss [ 110 ], to help determine the quality of a weld on a plate of finite thickness for a given metal, is to measure the backface width perpendicular to the traverse direction. The standard deviation about the mean for several experiments is calculated, and the weld quality is classified as good if the standard deviation is small (typically on a mean of 3mm is less than about 0.3mm). A large standard deviation, signifying large variations in the backface width and hence large variations in the structural properties of the weld is, for obvious reasons, classed as a poor weld. In the extreme, if the standard deviation is very large, then there is a significant probability that the weld will either not fully penetrate the plate, leaving a region where the two plates are not bonded together, or the molten metal will fall completely through the plate. Structurally, either could have disastrous results.

Willgoss [ 110 ] proposed the application of an additional external magnetic field sufficiently strong so that the electromagnetic force produced dominates over all other forces present. This was observed to considerably reduce the standard deviation of the backface widths of welds. The flows observed had a strong rotational component, and a low depth to width ratio. This situation was modelled by Weatherill [ 108 ] and Craine and Weatherill [ 21 ]. There is some evidence, however, that under these conditions the flow is no longer laminar, but has some degree of turbulence present [ 19 ], [ 66 ].

A more sophisticated approach would involve carrying out a full stability analysis of the problem. This might also show the existence of multiple steady-state solutions, which have been suggested by hysteresis effects observed under certain welding conditions [ 62 ]. Researchers at Marchwood Laboratories (before its closure) also believed this to be the case, as a result of experiments they performed in vibrating the weld pool to determine if it had penetrated through the metal. They observed that after vibration the depth of the weld increased considerably, out of proportion to the small increase in applied energy. A first step towards a full investigation of stability is carried out in Chapter 5, where the linear stability of the solutions found in Chapter 4 is investigated.

# Chapter 2: A Similarity Solution

## 2.1 Introduction

Most of the published work on modelling the process of arc welding has been concerned with the flows driven by electromagnetic forces only. Experimental work by Heiple and Roper [ 41 ] has shown that adding a relatively small amount of an impurity to liquid metals can change the variation of surface tension with temperature, and drastically change the shape of the weld pool produced, thus suggesting that the change in surface tension has changed the qualitative character of the flow. In this chapter a model for the flow of molten metal in the arc welding process is presented with the two major forces, the Lorentz and surface tension forces, included. The model is an extension of the work by Sozou [ 97 ], which contained just the electromagnetic force.

## 2.2 The Model

Solutions to the coupled heat and fluid flow equations are sought in a semi-infinite region of incompressible, electrically and thermally conducting fluid.

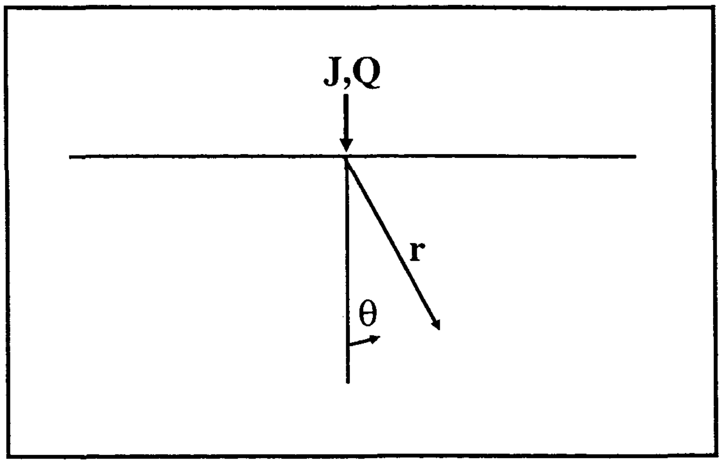

**Figure 2.1** The geometry for the similarity solution

The electric arc is modelled by a point source of heat and current placed at the origin. This is not a particularly good assumption, in that the arc has been shown experimentally to have a roughly Gaussian distribution under some conditions [ 63 ]. However, the point source assumption allows a similarity solution to be found, whereas the use of a Gaussian distribution would lead to a much more difficult problem since a similarity solution would not then exist. Published models of arc welding using just the electromagnetic forces have shown that the use of a physically realistic Gaussian distribution, as opposed to a point source, allows a solution to be found at higher current values, but the qualitative structure of the flows are not greatly different [ 11 ], [ 7 ]. Since the principal aim of the work presented here is to provide insight into the flow structure in the weld pool and to decide what has to be included to give an accurate model, not to provide precise but complicated numerical predictions about particular welding cases, the point source assumption is introduced in this work.

The top surface is assumed to be flat, which has been shown experimentally to be reasonable for low currents, less than ~200A [ 62 ]. The geometry is illustrated in Figure 2.1, using spherical polar coordinates.

The model presented in this chapter includes the electromagnetic forces, arising from the current in the weld pool and its self-induced magnetic field, and the surface tension forces on the top surface of the pool, formed from temperature gradients. These two forces are considered to be the largest of the forces present in the weld pool [ 24 ].

The derivation of the MHD equations governing the flow of the types of conducting liquids used in practical or laboratory applications (eg liquid metals, fused salts) has been given many times before (eg Shercliff [ 93 ]), so only the assumptions necessary for the derivation are included here. The liquid is assumed to be an incompressible Newtonian fluid and to have physical properties that are homogeneous and isotropic and, with the exception of the surface tension, to be independent of the temperature. The liquid's permeability differs little from the permeability of free space, its electrical conductivity is high and it has a small dielectric permittivity so that polarization can be neglected. For slowly varying processes, and for velocities much smaller than the velocity of light, the displacement and convection currents can be neglected in comparison to the conduction current.

Buoyancy is not included at this stage, because a similarity solution cannot be found with it in the model. This is probably not a major omission as it has been shown that the buoyancy force is usually significantly smaller than the electromagnetic and surface tension forces (eg. [ 24 ]). The buoyancy force is included in the numerical solution obtained in Chapter 4. A steady state solution is sought so all time derivatives are assumed zero.

The current flowing from the point source induces a magnetic field within the fluid. The current and its induced magnetic field are assumed to be unaffected by the flow, and hence the current distribution is spherically symmetric. The self-induced magnetic field can be calculated in this case, and the electromagnetic forcing term can then be worked out analytically. After seeking a similarity solution the resulting ordinary differential equations governing the fluid flow and the temperature distribution can be solved numerically.

## 2.3 Derivation of the Equations

The governing equations are:

the momentum transport - Navier-Stokes equation

$$(\mathbf{v}.\ \nabla)\mathbf{v} + \frac{1}{\rho}\nabla p - \nu\nabla^2\ \mathbf{v} - \frac{1}{\rho}\boldsymbol{J}\times\boldsymbol{B} = 0, \qquad (2.1)$$

where the first term describes the inertial forces, the second the pressure gradient, the third the viscous forces, and the fourth the electromagnetic forces;

the fluid is incompressible

$$\nabla.\mathbf{v} \equiv 0\ ; \qquad (2.2)$$

the heat transfer equation

$$\mathbf{v}\ .\nabla T\ =\ \kappa\nabla^2 T, \qquad (2.3)$$

where the left hand side describes heat transfer due to convection, and the right hand side gives heat transfer due to conduction. Ohmic heating has been ignored because a similarity solution cannot be found if the term is present and, due to the high electrical conductivity of the fluid, it will in any case be considerably smaller than the heat input of the arc.

In the above equations

$\mathbf{v}$ is the fluid velocity, p is the pressure,
$\rho$ is the density, $\nu$ is the kinematic viscosity, **J** is the current,
**B** is the magnetic field, $\kappa$ is the thermal diffusivity,
and T is the temperature.

As the value of the pressure is not required explicitly, taking the curl of equation (2.1) eliminates it from the equation, to give

$$-\nabla\times(\mathbf{v}\times(\nabla\times\mathbf{v})) = -\nu\nabla\times(\nabla\times(\nabla\times\mathbf{v})) + \frac{1}{\rho}\nabla\times(\mathbf{J}\times\mathbf{B}). \qquad (2.4)$$

Equations (2.4) and (2.3) are to be solved subject to the following boundary conditions:

There is no motion across the top surface

$$v_\theta = 0 \quad \text{on} \quad \theta = \frac{\pi}{2}. \tag{2.5}$$

There is no fluid crossing the axis $\theta=0$

$$v_\theta = 0 \quad \text{on} \quad \theta = 0. \tag{2.6}$$

There is no heat flux across the top surface

$$\frac{\partial T}{\partial \theta} = 0 \quad \text{on} \quad \theta = \frac{\pi}{2}. \tag{2.7}$$

The stress on the top surface due to surface tension is

$$\sigma_{r\theta} = \frac{\partial \gamma}{\partial r} = \frac{\partial \gamma}{\partial T}\frac{\partial T}{\partial r}, \tag{2.8}$$

where $\gamma$ is the surface tension, assumed to have a linear relationship with temperature (see figure 1.2).

The assumed spherically symmetric current distribution is described by

$$J = \hat{r}\, J_0 \frac{1}{2\pi r^2}, \tag{2.9}$$

where $J_0$ is the total current input to the system. From this the self-magnetic field can be calculated by using Ampere's law

$$\nabla \times \mathbf{B} = \mu_0 \mathbf{J},$$

where $\mu_0$ is the permeability of free space. Since **J** is purely radial, only the r-component of the above equation is non-zero, and so it follows that

$$\frac{1}{r \sin\theta}\left(\frac{\partial}{\partial \theta}\left[B_\varphi \sin\theta\right] - \frac{\partial B_\theta}{\partial \varphi}\right) = \frac{\mu_0 J_0}{2\pi r^2}. \tag{2.10}$$

Since the problem is axisymmetric all $\phi$-derivatives are identically zero. Then, integrating (2.10) once with respect to $\theta$ gives

$$B_\varphi \sin\theta = \frac{\mu_0 J_0}{2\pi r}\int \sin\theta d\,\theta = \frac{\mu_0 J_0}{2\pi r}\left(-\cos\theta + C(r)\right).$$

Evaluating this at $\theta=0$ shows that C is a constant with value 1. Introducing a new coordinate $\mu = \cos\theta$, **B** can be expressed as

$$B = \frac{J_0\, \mu_0\, (1-\mu)}{2\pi r(1-\mu^2)^{1/2}}\hat{\varphi}.$$

Observing that **J** is purely radial and **B** is purely azimuthal, **JxB** has only one non-zero component:

$$J\times B = -\hat{\theta}\,\frac{J_0^2\, \mu_0(1-\mu)}{4\pi^2 r^3(1-\mu^2)^{1/2}},$$

and hence

$$\frac{1}{\rho}\nabla\times(J\times B) = \hat{\Phi}\,\frac{J_0^2\, \mu_0(1-\mu)}{2\pi^2 \rho r^4(1-\mu^2)^{1/2}}. \qquad (2.11)$$

Equation (2.2) and the axisymmetric nature of the problem implies the existence of a streamfunction $\psi$ such that

$$\mathrm{v} = -\left(\frac{1}{r^2}\frac{\partial\psi}{\partial\mu},\, \frac{1}{r(1-\mu^2)^{1/2}}\frac{\partial\psi}{\partial r},\, 0\right). \qquad (2.12)$$

A similarity solution for the stream function can now be found by assuming the stream function to be separable in r and $\mu$

$$\psi = \mathrm{l(r)f(\mu)}. \qquad (2.13)$$

The velocity can be written using (2.13) as

$$\mathrm{v} = -\left(\frac{1}{r^2}\, l(r)f'(\mu),\, \frac{1}{r(1-\mu^2)^{1/2}}\, l'(r)f(\mu),\, 0\right),$$

where a dash denotes differentiation of a function with respect to the variable on which it depends.

Next consider the inertial and viscous terms in equation (2.4):

inertial term:

$$\nabla\times\mathrm{v} = \hat{\Phi}\left(\frac{1}{r}\frac{\partial}{\partial r}(r\,\mathrm{v}_\theta) + \frac{(1-\mu^2)^{1/2}}{r}\frac{\partial \mathrm{v_r}}{\partial\mu}\right)$$
$$= -\hat{\Phi}\left(\frac{1}{r}\frac{l''f}{(1-\mu^2)^{1/2}} + \frac{(1-\mu^2)^{1/2}}{r^3}\, lf''\right).$$

$$\mathbf{v}\times(\nabla\times\mathbf{v})=\hat{\mathbf{r}}\frac{1}{r^2}l'f\left(\frac{l''f}{(1-\mu^2)}+\frac{lf''}{r^2}\right)-\hat{\theta}\frac{1}{r^3}lf'\left(\frac{l''f}{(1-\mu^2)^{1/2}}+\frac{(1-\mu^2)^{1/2}}{r^2}lf''\right).$$

$$\nabla\times(\mathbf{v}\times(\nabla\times\mathbf{v}))=\hat{\Phi}\left(\frac{1}{r}\frac{\partial}{\partial r}\left[\frac{-1}{r^2}lf'\left(\frac{l''f}{(1-\mu^2)^{1/2}}+\frac{(1-\mu^2)^{1/2}}{r^2}lf''\right)\right]\right.$$
$$\left.+\frac{(1-\mu^2)^{1/2}}{r}\frac{\partial}{\partial\mu}\left[\frac{1}{r^2}l'f\left(\frac{l''f}{(1-\mu^2)}+\frac{lf''}{r^2}\right)\right]\right)$$
$$=\hat{\Phi}\left(\frac{-lf'}{r}\left[\left(\frac{l''}{r^2}\right)'\frac{f}{(1-\mu^2)^{1/2}}+(1-\mu^2)^{1/2}f''\left(\frac{l}{r^4}\right)'\right]+(1-\mu^2)^{1/2}l'f\left[\frac{l''}{r^3}\left(\frac{f}{(1-\mu^2)}\right)'+\frac{lf'''}{r^5}\right]\right);\ (2.14)$$

viscous term:

$$\nabla\times(\nabla\times\mathbf{v})=-\hat{\mathbf{r}}\frac{1}{r}\left(\frac{\partial}{\partial\mu}\left[\frac{-1}{r}\left(\frac{l''f}{(1-\mu^2)^{1/2}}+\frac{(1-\mu^2)^{1/2}}{r^2}lf''\right)(1-\mu^2)^{1/2}\right]\right)$$
$$-\hat{\theta}\frac{1}{r}\left(\frac{\partial}{\partial r}\left[\frac{-1}{r}\left(\frac{l''f}{(1-\mu^2)^{1/2}}+\frac{(1-\mu^2)^{1/2}}{r^3}lf''\right)r\right]\right)$$
$$=\hat{\mathbf{r}}\frac{1}{r}\left(\frac{l''f'}{r}+\frac{l}{r^3}[f''(1-\mu^2)]'\right)$$
$$+\hat{\theta}\frac{1}{r}\left(\frac{l'''f}{(1-\mu^2)^{1/2}}+(1-\mu^2)^{1/2}f''\left(\frac{l}{r^2}\right)'\right),$$

$$\nabla\times(\nabla\times(\nabla\times\mathbf{v}))=\hat{\Phi}\left(\frac{1}{r}\frac{\partial}{\partial r}\left[\frac{l'''f}{(1-\mu^2)^{1/2}}+(1-\mu^2)^{1/2}f''\left(\frac{l}{r^2}\right)'\right]\right.$$
$$\left.+\frac{(1-\mu^2)^{1/2}}{r}\frac{\partial}{\partial\mu}\left[\frac{1}{r}\left(\frac{l''f'}{r}+\frac{l}{r^3}[f''(1-\mu^2)]'\right)\right]\right)$$
$$=\hat{\Phi}\left(\frac{l^{IV}}{r}\frac{f}{(1-\mu^2)^{1/2}}+\frac{(1-\mu^2)^{1/2}f''}{r}\left(\frac{l}{r^2}\right)''+\frac{(1-\mu^2)^{1/2}}{r}\left(\frac{l''}{r^2}f''+\frac{l}{r^4}[f''(1-\mu^2)]'\right)\right).(2.15)$$

To separate the variables in the viscosity term (2.15), it is essential that the factors depending on r are proportional to each other, clearly this is possible when *l* is a power of r ($l$~$r^a$). Substituting such an expression in to (2.14) and (2.15), we find that the inertial term is of order $r^{(2a-6)}$ and the viscous term is of order $r^{(a-5)}$, and these are only equal when a=1. Therefore $l = Cr$, where C is a constant. Since the dimension of the stream function is $L^3/T$ the dimension of C must be $L^2/T$ in order for f to be non-dimensional. Setting C to be the kinematic viscosity, which also has dimension of $L^2/T$, the assumed form for the stream function is

$$\psi=\nu rf(\mu).\qquad(2.16)$$

From (2.12) and (2.16) it follows that

$$\mathrm{v} = -\frac{\nu}{r}\left(f'(\mu)\,,\ \frac{1}{(1-\mu^2)^{1/2}}f(\mu)\,,\ 0\right). \tag{2.17}$$

Looking at (2.11), (2.14) and (2.15) it is obvious that (2.4) has only one non-zero component, and after multiplying through by $\frac{r^4}{\nu^2}$ the resulting ODE is

$$3\,(1-\mu^2)^{1/2}f'f'' + (1-\mu^2)^{1/2}ff''' - 2(1-\mu^2)^{1/2}f'' - (1-\mu^2)^{1/2}[f''(1-\mu^2)]'' + \frac{J_0^2\,\mu_0(1-\mu)}{2\pi^2\nu^2\rho(1-\mu^2)^{1/2}} = 0.$$

Alternatively this can be written as

$$\left(f^2\right)''' = 4f' + 2\,[f''(1-\mu^2)]'' - \frac{J_0^2\,\mu_0}{\pi^2\nu^2\rho(1+\mu)}\,. \tag{2.18}$$

This equation can easily be integrated twice with respect to μ to become

$$\left(f^2\right)' = 2(1-\mu^2)f'' + 4f + 2a\mu + b - F'(\mu), \tag{2.19}$$

and integrated once more to give

$$f^2 = 2\,(1-\mu^2)f' + 4\mu f + a\,\mu^2 + b\,\mu + c - F(\mu)\,, \tag{2.20}$$

where

$$F(\mu) = \frac{J_0{}^2\mu_0}{\rho\nu^2\pi^2}\left[\frac{1}{2}(1+\mu)^2\ln(1+\mu) - \frac{\mu}{2}\left(1+\frac{3\mu}{2}\right)\right] \tag{2.21}$$

and the values of the three constants of integration a,b and c, are evaluated later (see (2.32), (2.33) and (2.34)). Equation (2.20) is essentially the same as that obtained by Sozou in his original paper [ 97 ]. If the term F(μ) is removed from the right hand side, equation (2.20) becomes that obtained by Slezkin [ 96 ], discussed by Batchelor [ 9 ], for the momentum transfer through a viscous jet.

Now consider the temperature. Assuming that T can be expressed as

$$T = h(r)g(\mu),$$

(c.f. (2.13)), and recalling the velocity definition (2.17) , the radial stress can be written as

$$\begin{aligned}\sigma_{r\theta} &= \rho\nu\left(\frac{1}{r}\frac{\partial v_r}{\partial\theta} - \frac{v_\theta}{r} + \frac{\partial v_\theta}{\partial r}\right)\\ &= \frac{\rho\nu^2}{r^2}\left(\frac{2f}{(1-\mu^2)^{1/2}} + (1-\mu^2)^{1/2}f''\right).\end{aligned} \tag{2.22}$$

Evaluating (2.22) at $\mu$=0 and making use of (2.28), boundary condition (2.8) can now be written as

$$\frac{\rho\nu^2}{r^2}f''(0) = \frac{\partial\gamma}{\partial T}h'(r)g(0). \tag{2.23}$$

From (2.23) h(r) has to have the form 1/r. Hence T is given by

$$T = \frac{1}{r}\,g(\mu). \tag{2.24}$$

It is not possible to write g($\mu$) in non-dimensional form due to the lack of a length or time scale in the formulation of the problem.

The convection term in equation (2.3) can now be written as

$$\begin{aligned}\mathrm{v}.\nabla T &= \left(\frac{-\nu}{r}f',\ \frac{-\nu}{r(1-\mu^2)^{1/2}}f,\ 0\right)\cdot\left(\frac{\partial}{\partial r}\left[\frac{g}{r}\right],\ \frac{-(1-\mu^2)^{1/2}}{r}\frac{\partial}{\partial\mu}\left[\frac{g}{r}\right],\ 0\right)\\ &= \frac{\nu}{r^3}(fg'+f'g).\end{aligned} \tag{2.25}$$

The diffusion term in (2.3) can be written

$$\begin{aligned}\kappa\nabla^2 T &= \kappa\left(\frac{\partial^2}{\partial r^2}\left[\frac{g}{r}\right] + \frac{2}{r}\frac{\partial}{\partial r}\left[\frac{g}{r}\right] - \frac{2\mu}{r^2}\frac{\partial}{\partial\mu}\left[\frac{g}{r}\right] + \frac{(1-\mu^2)}{r^2}\frac{\partial^2}{\partial\mu^2}\left[\frac{g}{r}\right]\right)\\ &= \frac{\kappa}{r^3}\left((1-\mu^2)g'' - 2\mu g'\right)\end{aligned} \tag{2.26}$$

and this means that the temperature equation (2.3) is now given by

$$(1-\mu^2)\kappa g'' - 2\mu\kappa g' = \nu g'f + \nu g f'.$$

This can be integrated once with respect to $\mu$ to become

$$g' = \frac{\nu f g}{\kappa(1-\mu^2)}, \tag{2.27}$$

with boundary conditions (2.28) and (2.30) showing that the constant of integration is zero.

Given the definitions (2.17) and (2.24), the boundary conditions (2.5), (2.6), (2.7) and (2.8) can be written respectively as

$$v_\theta(0) = 0 \;\Rightarrow\; f(0) = 0, \tag{2.28}$$

$$v_\theta(1) = 0 \;\Rightarrow\; f(1) = 0, \tag{2.29}$$

$$\frac{\partial T}{\partial \theta} = 0 \;\Rightarrow\; g'(0) = 0, \tag{2.30}$$

$$-\rho\nu^2 f''(0) = \frac{\partial \gamma}{\partial T}\, g(0). \tag{2.31}$$

It is now possible to determine the constants of integration a, b and c in equation (2.20). Evaluating equations (2.19) and (2.20) at $\mu$=0 and $\mu$=1, making use of boundary conditions (2.28) and (2.29), and the fact that F(0) and F′(0) are both equal to zero, the following four equations are obtained:

$$\begin{aligned} b &= -2f''(0), \\ 2a + b &= F'(1), \\ c &= -2f'(0), \\ a + b + c &= F(1). \end{aligned}$$

From these equations the values for a, b and c in terms of f′(0) can be obtained,

$$\begin{aligned} a &= F'(1) - F(1) - 2f'(0) \\ &= \frac{J_0{}^2\mu_0}{\rho\nu^2\pi^2}\frac{1}{4} - 2f'(0) \end{aligned} \tag{2.32}$$

$$\begin{aligned} b &= 2F(1) - F'(1) + 4f'(0) \\ &= \frac{J_0{}^2\mu_0}{\rho\nu^2\pi^2}(2\ln 2 - 3/2) + 4f'(0) \end{aligned} \tag{2.33}$$

$$c = -2f'(0). \tag{2.34}$$

Bearing in mind that $b = -2f''(0)$, boundary condition (2.31) can alternatively be expressed

$$b = \frac{J_0{}^2\mu_0}{2\rho\nu^2\pi^2}(2\ln 2 - 3/2) + 4f'(0) = 2\,\frac{\partial\gamma}{\partial T}\,\frac{1}{\rho\nu^2}\,g(0). \tag{2.35}$$

Since equation (2.20) is of Ricatti-type, it can be transformed to a second order linear equation by the introduction of a new variable u(μ) which is related to f(μ) by

$$f(\mu) = -2\,(1-\mu^2)\frac{u'(\mu)}{u\,(\mu)}. \tag{2.36}$$

Equation (2.20) then becomes

$$u'' = \frac{u}{4(1-\mu^2)^2}[a\,\mu^2 + b\,\mu + c - F(\mu)], \tag{2.37}$$

which is solved subject to the boundary conditions

$$u'(0) = 0,\;\; u(0) = 1. \tag{2.38}$$

The first condition in (2.38) follows from (2.28) and the definition of u, whereas the second condition is chosen for normalisation.

A minor inconvenience is the fact that to evaluate the boundary condition (2.23) and the coefficients a, b, and c in equation (2.37) the value of f′(0) is required, but this cannot be determined from the prescribed boundary conditions. The extra condition that is imposed in order to calculate the correct value for f′(0) is that the total heat input into the system in GTA welding has been experimentally found to be approximately six times the current input [ 57 ].

To calculate the heat input produced by a given value of f′(0), the total heat flux through a small hemisphere around the origin is calculated. The heat flux is due to two mechanisms, conduction and convection. The heat conducted is determined by the temperature gradient on this hemisphere (see figure (2.3) ), and is given by :

$$q_1 = -k\frac{\partial T}{\partial r} = \rho c_p \kappa \frac{1}{r^2}\,g, \tag{2.39}$$

where k is the thermal conductivity and $c_p$ is the specific heat capacity of the material.

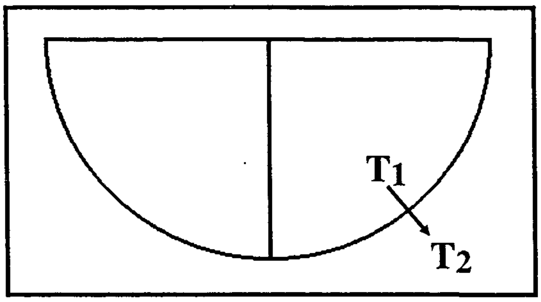

**Figure 2.3** - Conduction of heat through a hemisphere

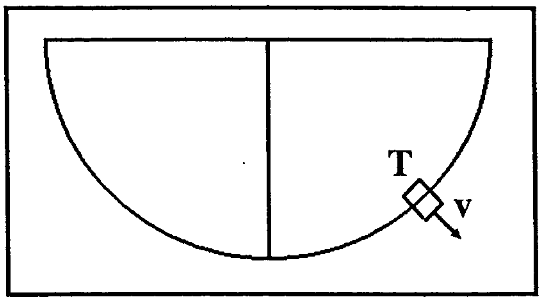

**Figure 2.2** - Convection of heat through a hemisphere

The heat convected depends on the temperature and the mass of fluid passing through the hemisphere (see figure 2.2) :

$$q_2 = T c_p \rho \, v_r = \frac{1}{r} g \, c_p \rho \left(-\frac{\nu}{r} f'\right) = - c_p \rho \nu \frac{1}{r^2} g f'. \qquad (2.40)$$

The total heat flux is then obtained by integrating the sum of $q_1$ and $q_2$ over a full $2\pi$ revolution in $\varphi$, and over $\mu$ from 0 to 1, giving

$$Q = \int_0^{2\pi} \int_0^{1} \left( \frac{- c_p \rho \nu}{r^2} g f' + \rho c_p \frac{\kappa}{r^2} g \right) r^2 d\varphi \, d\mu$$

$$= 2\pi \rho c_p \int_0^1 g(\kappa - \nu f') \, d\mu. \qquad (2.41)$$

## 2.3.1 Method of solution

To solve the problem, equations (2.37), (2.27) and (2.41) are written as first order differential equations, which are solved subject to boundary conditions (2.35) and (2.38) using a NAG routine (DO2BBF). This routine uses a Runge-Kutta-Merson method to integrate a system of first order ODE's over a prescribed range subject to given initial conditions. The necessary value for $f'(0)$ is obtained by initially guessing a value , which is then altered if the value for Q obtained on solving the equations is not within 0.1% of $6J_0$. This correction procedure required no special algorithm, since the value for Q behaved monotonically with $f'(0)$ for most of the range of values of $J_0$ and $\frac{\partial\gamma}{\partial T}$.

## 2.4 Results and discussion

In all the results presented here values for $\nu$, $\kappa$, $\rho$ and $c_p$ which are appropriate for liquid steel are prescribed:

$\rho$ $= 7000 \text{ kg m}^{-3}$
$\nu$ $= 6.4 * 10^{-7} \text{ m}^2\text{s}^{-1}$
$\kappa$ $= 1.0 * 10^{-5} \text{ WmK}^{-1}\text{s}^{-1}$
$c_p$ $= 600 \text{ J kg}^{-1}\text{K}^{-1}$

### 2.4.1 Case 1 : Positive surface tension gradient

The highest temperatures in the liquid will occur at the origin, and hence equation (2.8) shows that when $\frac{\partial\gamma}{\partial T}$ is positive the surface tension force is directed towards the origin. The electromagnetic forces also act to force the fluid inwards along the top surface, and down the axis. Hence it would be expected that for a particular current value, as the surface tension force increases the velocity of the fluid increases, but the qualitative nature of the flow remains basically unchanged. This is indeed the case. For all values of positive $\frac{\partial\gamma}{\partial T}$ the fluid describes a single loop, inwards along the top surface and down the axis $\mu=1$ ($\theta=0$). Considering the definition of $f(\mu)$ in terms of $u(\mu)$ (equation (2.36) above), it is obvious that the radial velocity component, which is proportional to $f'$, will become infinite down the axis $\mu = 1$ if $u(1)$ becomes zero. This was the problem Sozou encountered in his work [ 97 ]. The addition of the surface tension force does not eliminate this problem, and in the case of positive $\frac{\partial\gamma}{\partial T}$ the increase in velocity causes this breakdown to occur at lower current values.

Figure 2.4 displays, for a particular value of $\frac{\partial\gamma}{\partial T} = +8*10^{-6} \text{ Nm}^{-1}\text{K}^{-1}$, the value of three quantities: $f'(0) = r\, v_r/\nu$ indicating the velocity on the top surface, $f'(1)$ indicating the

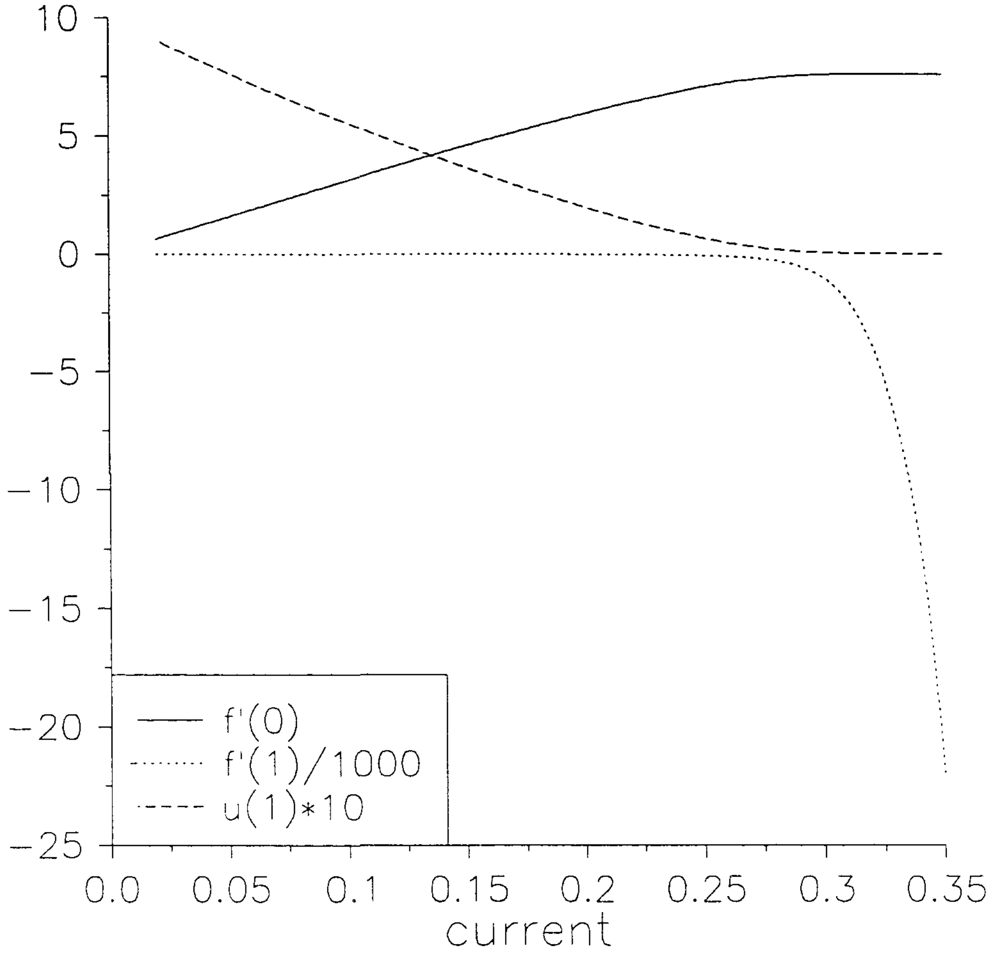

**Figure 2.4** - values of particular quantities for $\frac{\partial\gamma}{\partial T}=+8*10^{-6}\mathrm{Nm}^{-1}\mathrm{K}^{-1}$

velocity down the axis, and the value of u(1), for increasing values of applied current. This figure shows the rapid increase in fluid velocity down the axis as u(1) approaches zero.

Figures 2.5 to 2.8 display streamlines and isotherms for four values of the applied current (with $\frac{\partial\gamma}{\partial T}$ fixed at $+8*10^{-6}\,\mathrm{Nm}^{-1}\mathrm{K}^{-1}$).The numbers on the figures indicate values of $\Psi/\nu L$ and TL, where L is some length and the displayed axes are L long.

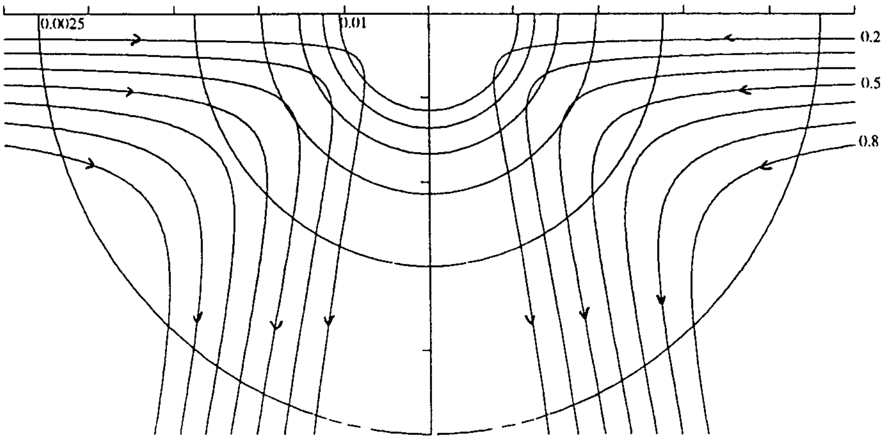

**Figure 2.5** - streamlines and isotherms for $J_0$=0.1A and $\frac{\partial \gamma}{\partial T} = +8*10^{-6}\mathrm{Nm}^{-1}\mathrm{K}^{-1}$

Figure 2.5 is a plot at 0.1 A and clearly shows the single loop structure with a nearly spherical temperature distribution.

Figure 2.6 is a plot at 0.2 A and it can be seen that the streamlines down the axis are coming closer together, indicating an increasing downward velocity parallel to the axis. The isotherms also display a slight elongation down the axis, indicating that the warmer fluid, heated at the origin, is being forced down the axis, as convection starts to dominate over conduction as the method of heat propagation.

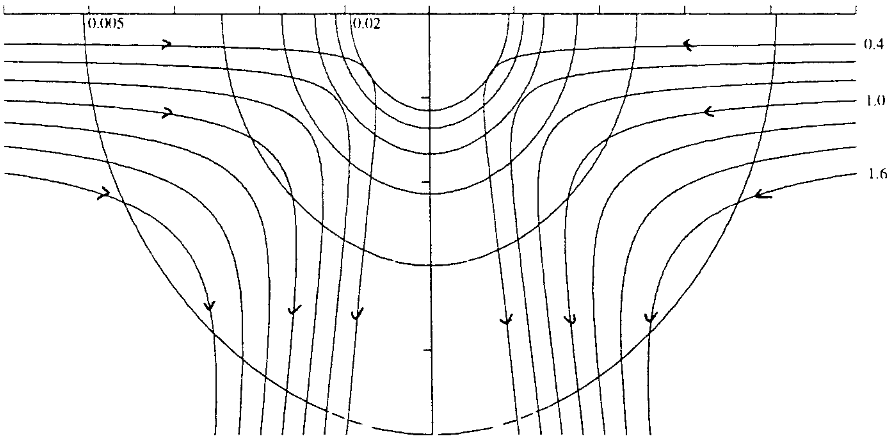

**Figure 2.6** - streamlines and isotherms for $J_0$=0.2A and $\frac{\partial \gamma}{\partial T} = +8*10^{-6}\mathrm{Nm}^{-1}\mathrm{K}^{-1}$

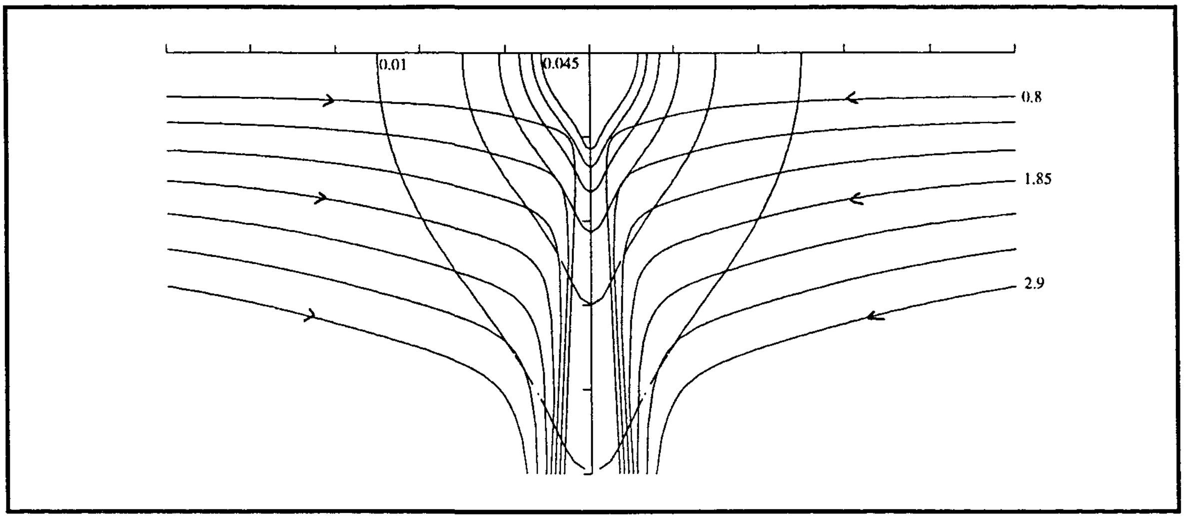

**Figure 2.7** - streamlines and isotherms for $J_0$=0.3A and $\frac{\partial \gamma}{\partial T}=+8*10^{-6}Nm^{-1}K^{-1}$

Figure 2.7 is a plot at 0.3 A, which is at the beginning of the region of rapid increase in radial velocity. The formation of a jet like structure down the axis can be seen, with the isotherms now being far from spherical.

Figure 2.8 is a plot at 0.34 A, a value just short of the point where breakdown occurs. A narrow high velocity jet down the axis can be clearly seen, with the isotherms being greatly elongated down the axis.

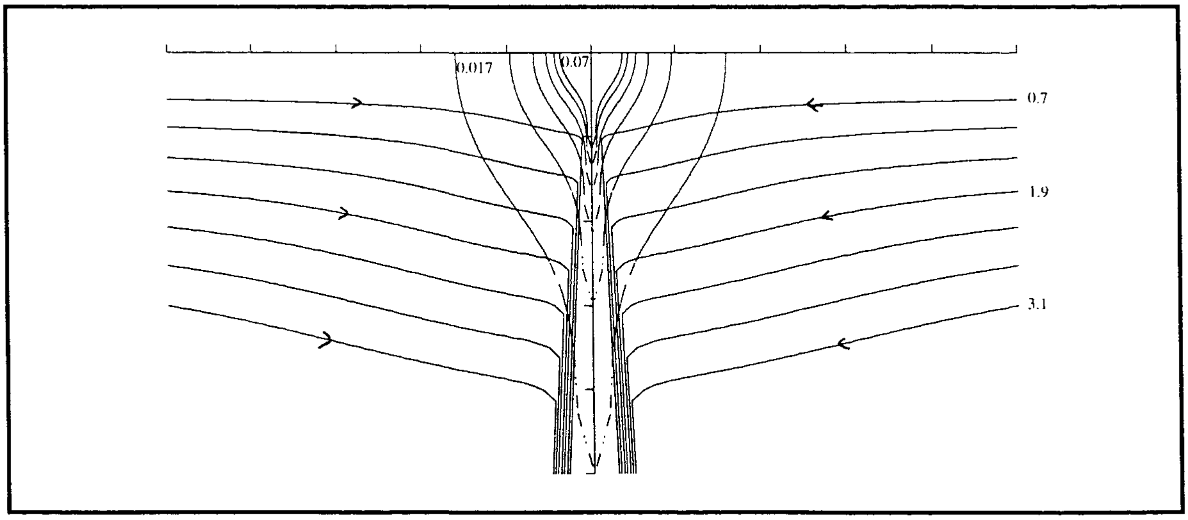

**Figure 2.8** - streamlines and isotherms for $J_0$=0.34A and $\frac{\partial \gamma}{\partial T}=+8*10^{-6}Nm^{-1}K^{-1}$

The evolution of the flow and isotherm patterns presented in figures 2.5 to 2.8 is typical of that occurring for all positive values of $\frac{\partial \gamma}{\partial T}$, although the particular current values at which the changes occur vary considerably depending on the value of $\frac{\partial \gamma}{\partial T}$ chosen, with the current values decreasing as $\frac{\partial \gamma}{\partial T}$ increases.

Very close to the current value at which breakdown occurs it is difficult to obtain solutions due to the high velocity gradients present near the axis. Using a quadratic extrapolation it is possible to determine a good approximation to the point where u(1) goes through zero, and hence f′(1) goes infinite. Figure 2.9 displays these values as a graph of breakdown current vs. $\log_{10} \frac{\partial \gamma}{\partial T}$. This shows very clearly the great influence the surface tension forces can have on the flow, since when $\frac{\partial \gamma}{\partial T}$ is about $10^{-4}\mathrm{Nm}^{-1}\mathrm{K}^{-1}$ the breakdown current is approximately 2 orders of magnitude less than when $\frac{\partial \gamma}{\partial T}$ is about $10^{-7}\mathrm{Nm}^{-1}\mathrm{K}^{-1}$. It should be noted that the breakdown current for $\frac{\partial \gamma}{\partial T} = 10^{-4}\mathrm{Nm}^{-1}\mathrm{K}^{-1}$ is almost zero.

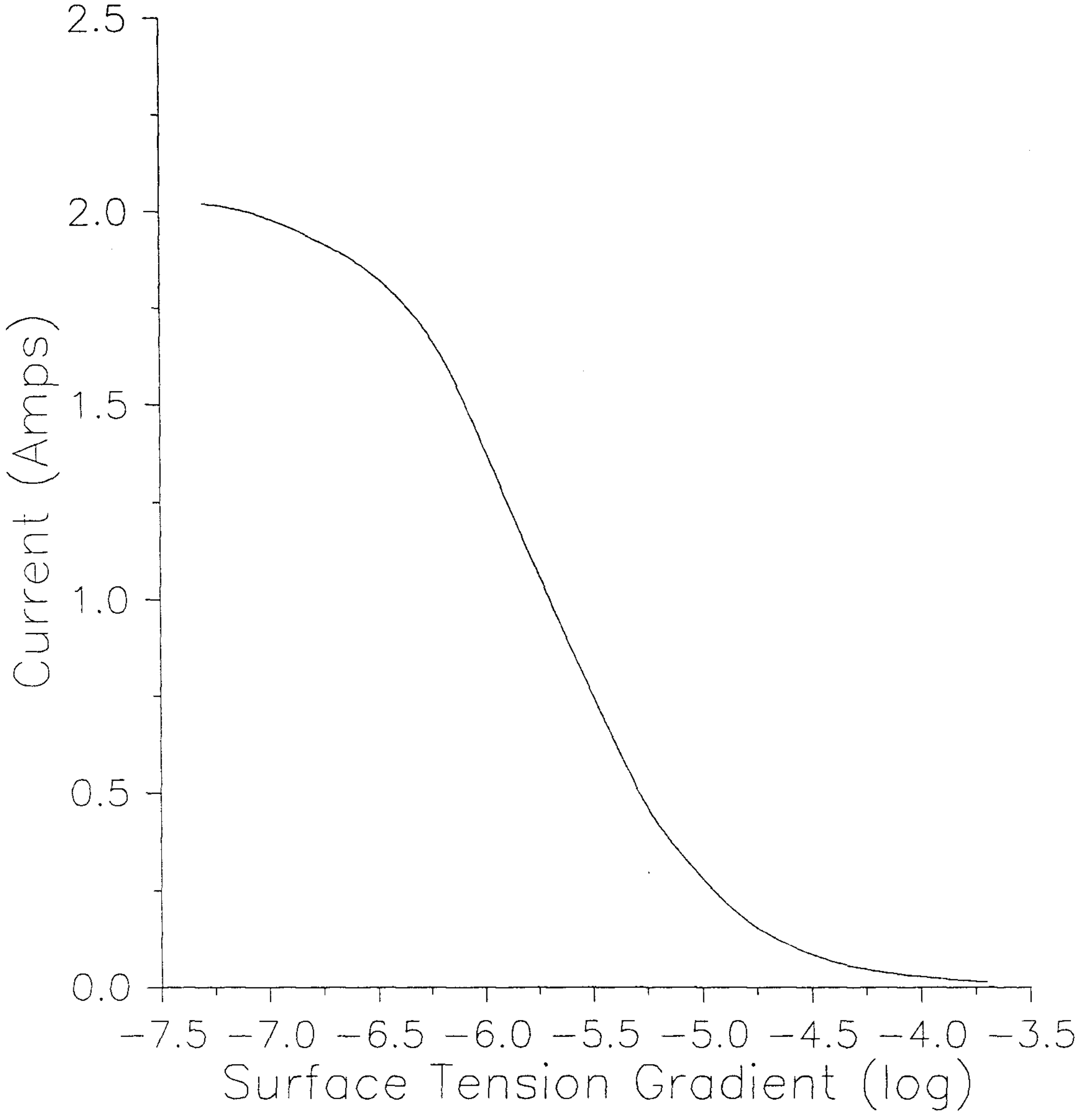

**Figure 2.9** - Breakdown current for positive $\frac{\partial\gamma}{\partial T}$

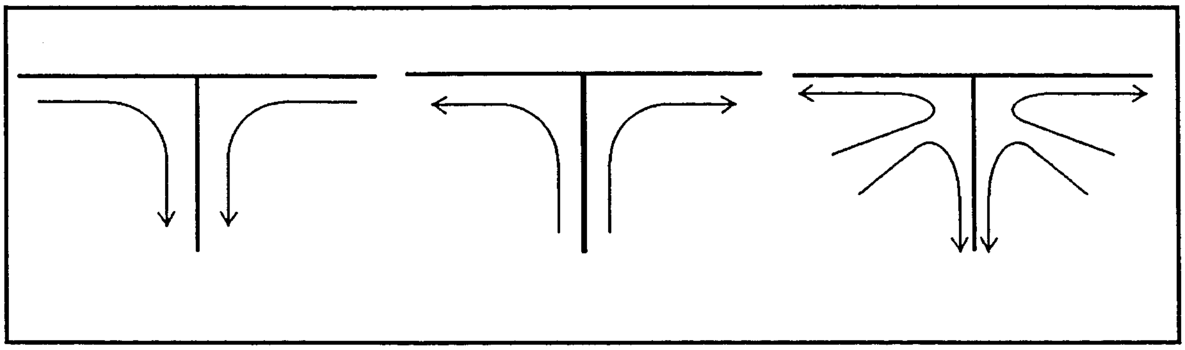

**Figure 2.10** - Possible flow structures for negative $\frac{\partial\gamma}{\partial T}$

## 2.4.2 Case 2 : negative surface tension gradient

The temperature gradients in the liquid will remain as before, with the temperature decreasing outwards from the origin. A negative surface tension gradient therefore causes the surface tension forces to be directed outwards along the top surface, opposing the electromagnetic forces. Intuitively it can be seen that there are three possible qualitative structures for the fluid flow in this case. If the electromagnetic forces dominate, the flow will have a single loop, with the fluid moving in along the top surface and down the axis. If the surface tension forces dominate, then the flow will again be a single loop, but this time up the axis and out along the top surface. If neither force dominates then there will be a flow with two loops, fluid flowing out along the top surface and down the axis, but inward at some intermediate value of $\mu$ (see figure 2.10). These expectations are confirmed by the detailed results presented below.

Figure 2.11 displays the values of u(1), f′(0) and f′(1) for $\frac{\partial\gamma}{\partial T} = -5*10^{-7}\ \mathrm{Nm^{-1}K^{-1}}$. The points where f′(0) and f′(1) cross the axis indicate the current values where the direction of flow along the top surface, or down the axis, reverses, ie. where the qualitative character of the flow changes between the cases mentioned above.

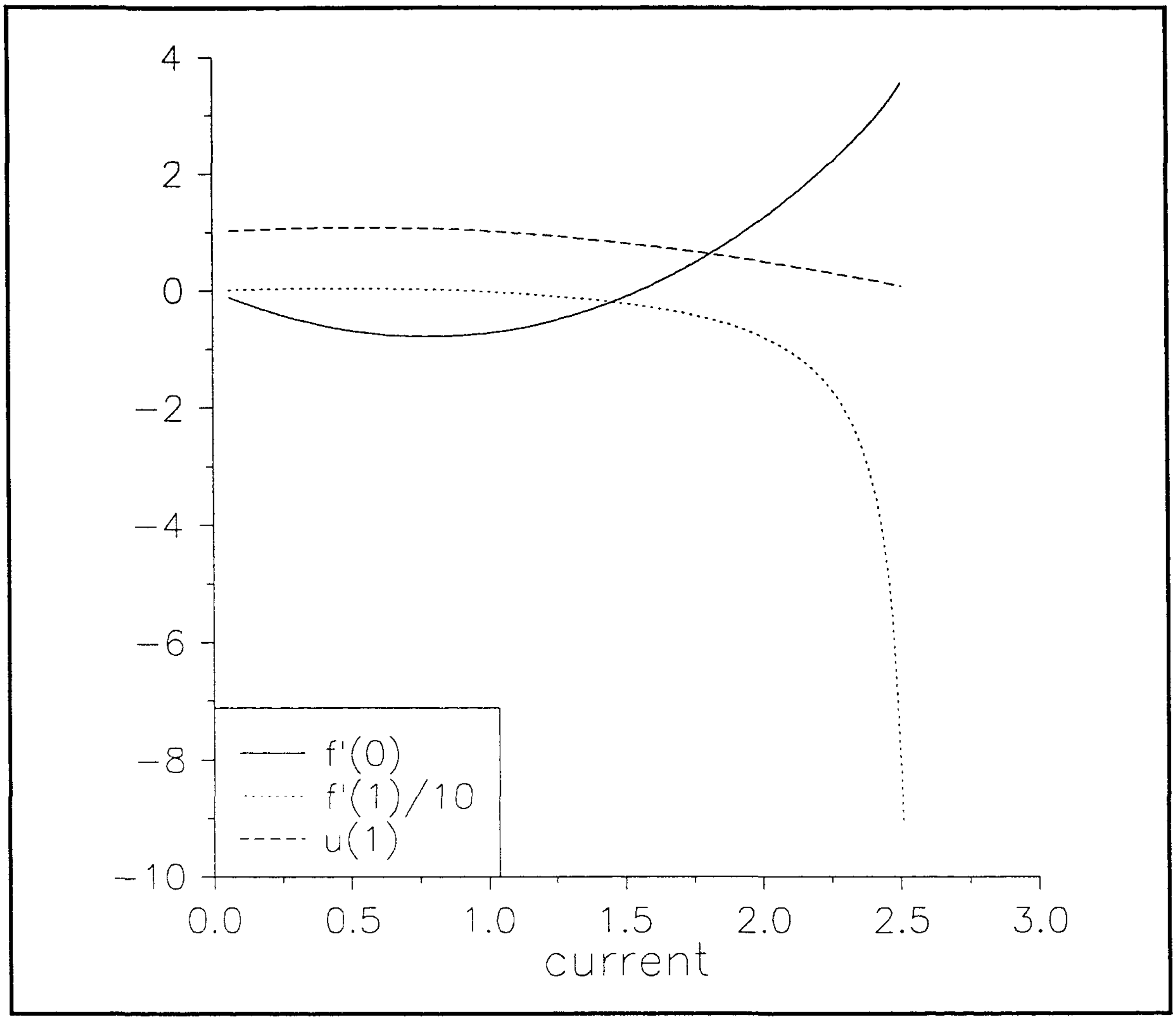

**Figure 2.11** - values of particular quantities for $\frac{\partial\gamma}{\partial T}$=-5*10$^{-7}$Nm$^{-1}$K$^{-1}$

Figure 2.12 is a plot of streamlines and isotherms for the case $\frac{\partial\gamma}{\partial T}$ = -5*10$^{-7}$ Nm$^{-1}$K$^{-1}$, at a current of 0.5 A. This shows a purely outward flow on the top surface, and a single loop structure. The surface tension forces dominate the electromagnetic forces, with the fluid moving outward on the surface considerably faster than in the rest of the fluid. The velocities are not fast enough, however, to cause significant convection of heat, and hence the isotherms are nearly spherical.

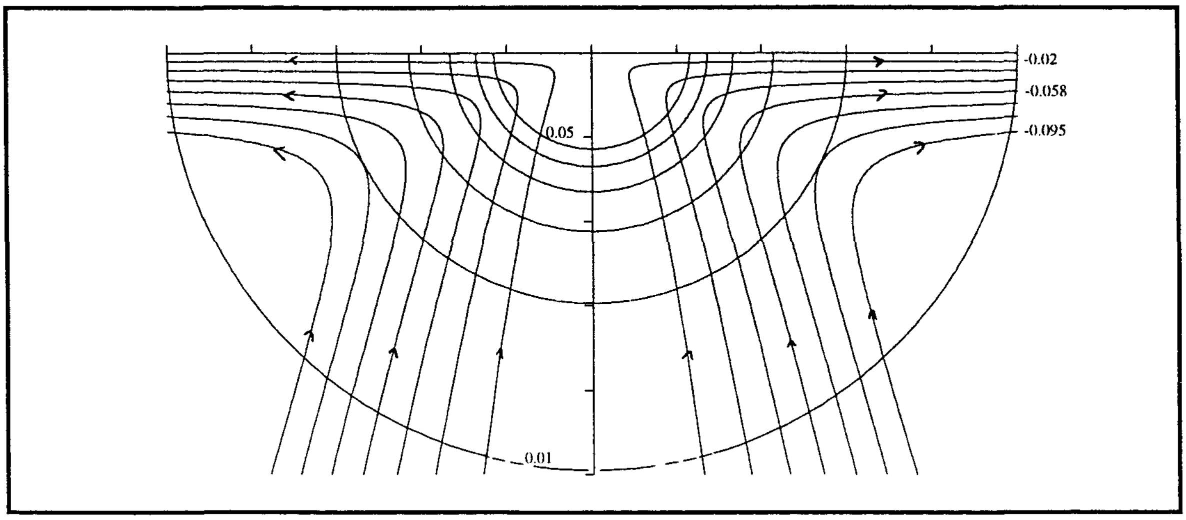

**Figure 2.12** - streamlines and isotherms for $J_0$=0.5A and $\frac{\partial\gamma}{\partial T}=-5*10^{-7}\mathrm{Nm^{-1}K^{-1}}$

Figure 2.13 shows the flow at 1.0 A, which is shortly after the value of f′(1) has passed through zero. Looking at this graph it can be seen that there is a relatively strong outward flow along the top surface. Also there is a region near the axis $\mu=1$, where the electromagnetic forces now dominate, and a second slower, counter rotating loop is produced. The isotherms, being nearly spherical, show that the velocities are not sufficiently large for convection to be important.

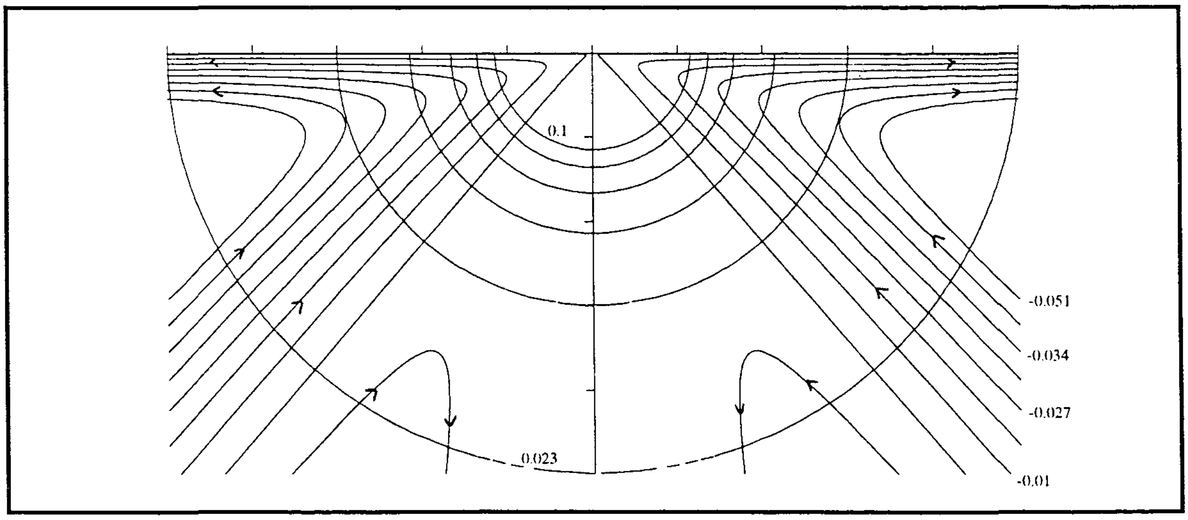

**Figure 2.13** - streamlines and isotherms for $J_0$=1.0A and $\frac{\partial\gamma}{\partial T}=-5*10^{-7}\mathrm{Nm^{-1}K^{-1}}$

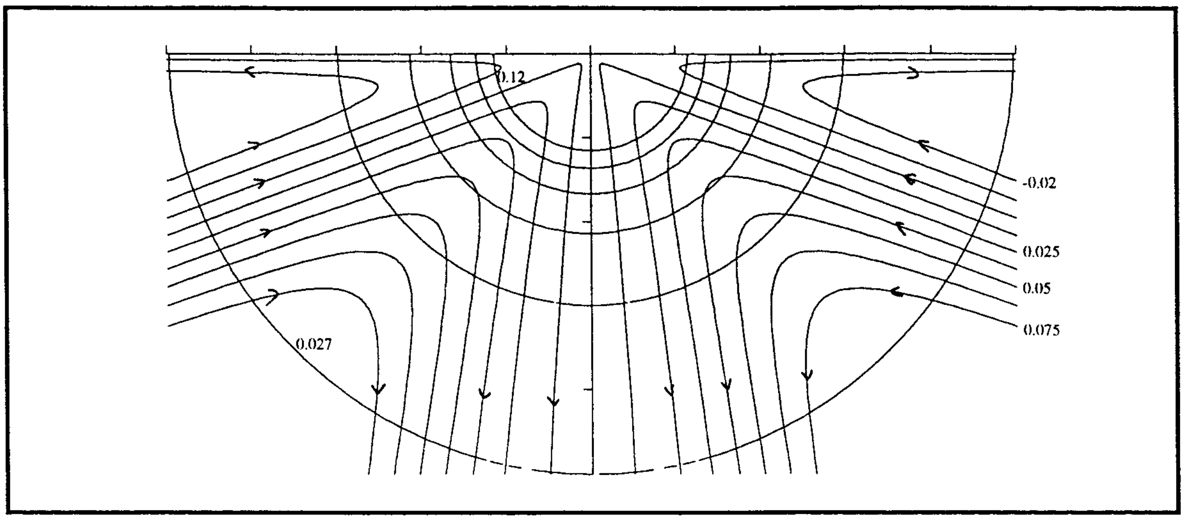

**Figure 2.14** - streamlines and isotherms for $J_0$=1.2A and $\frac{\partial\gamma}{\partial T}$=-5*$10^{-7}$Nm$^{-1}$K$^{-1}$

Figure 2.14 displays the flow patterns at 1.2 A. This shows the way that the boundary line between the portion of the flow which is dominated by the electromagnetic forces and that dominated by the surface tension forces is sweeping upwards towards the top surface, with the electromagnetic forces now dominating over most of the region.

Figure 2.15 shows the flow pattern at the current value, 1.5 A, where the electromagnetic forces dominate everywhere over the entire region, and the flow is in a single loop.

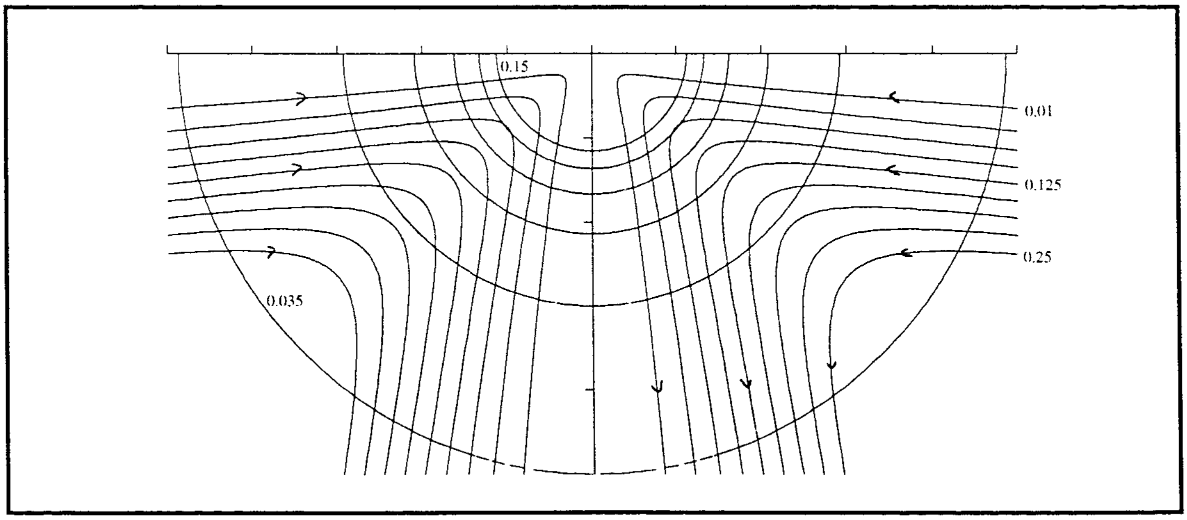

**Figure 2.15** - streamlines and isotherms for $J_0$=1.5A and $\frac{\partial\gamma}{\partial T}$=-5*$10^{-7}$Nm$^{-1}$K$^{-1}$

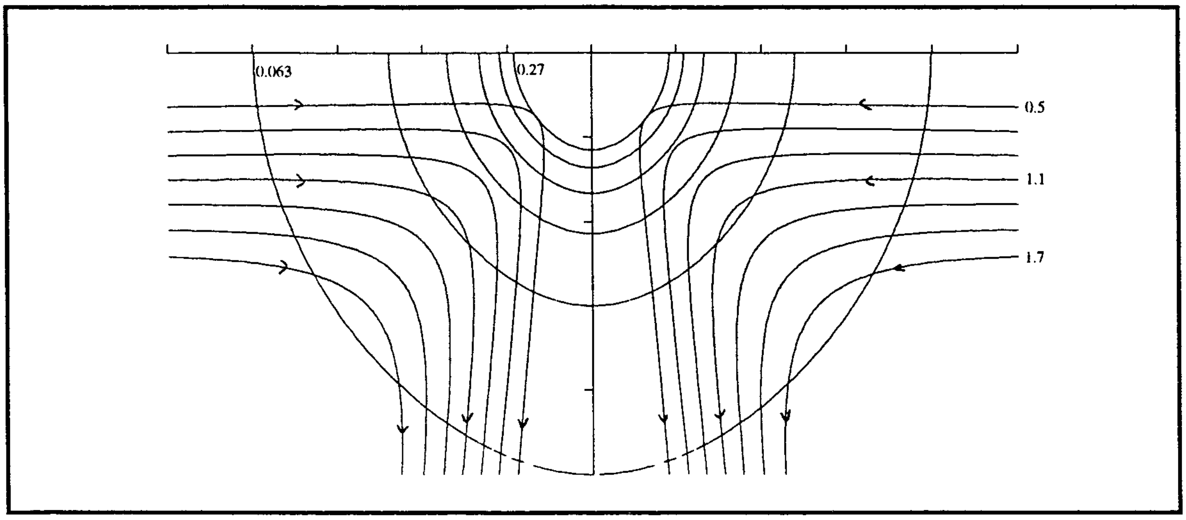

**Figure 2.16** - streamlines and isotherms for $J_0$=2.4A and $\frac{\partial\gamma}{\partial T}$=-5*$10^{-7}$Nm$^{-1}$K$^{-1}$

Figures 2.16 and 2.17 show the streamlines and isotherms at 2.4 A and 2.5 A respectively. Comparing these plots with figures 2.6 and 2.7 it can be seen that a similar jet like structure is being created. Also the velocities are now large enough that convection is important in determining the heat flow, and the isotherms are elongated down the axis.

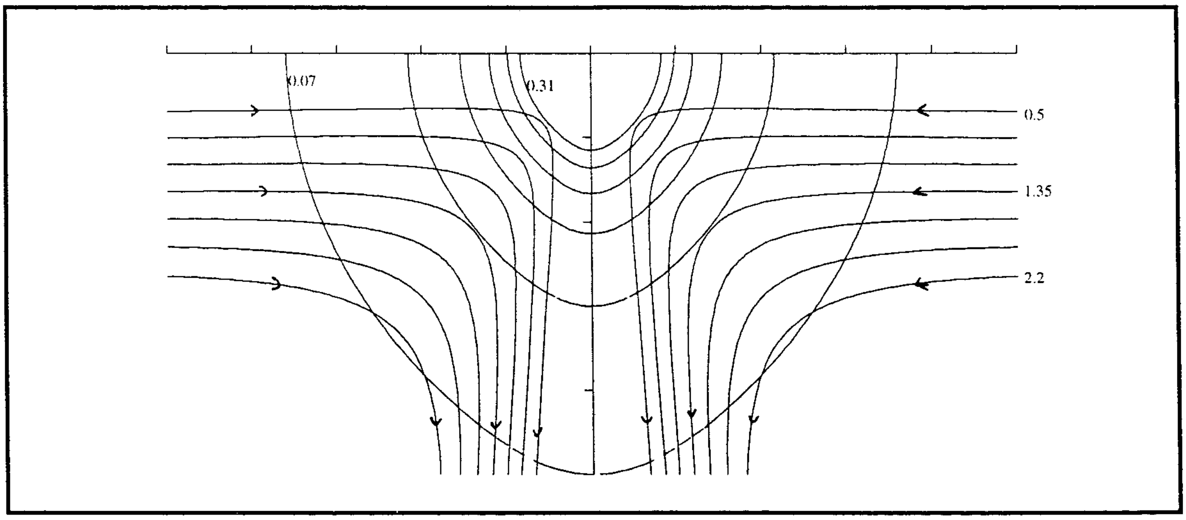

**Figure 2.17** - streamlines and isotherms for $J_0$=2.5A and $\frac{\partial\gamma}{\partial T}$=-5*$10^{-7}$Nm$^{-1}$K$^{-1}$

From figure 2.11 it is clear that the value of u(1) is tending towards zero, and hence the flow will reach the point of breakdown, with infinite velocity down the axis, for values of the applied current only slightly larger than 2.5A.

The above results are for a fairly small value of $\frac{\partial \gamma}{\partial T}$, $-5*10^{-7}$ $\mathrm{Nm^{-1}K^{-1}}$. For larger values of $\frac{\partial \gamma}{\partial T}$ it is not always possible to realise the three possible flow types before the point of breakdown is reached. For instance, consider the case for $\frac{\partial \gamma}{\partial T} = -2*10^{-6}$ $\mathrm{Nm^{-1}K^{-1}}$. Figure 2.18 displays the values of u(1), f′(0) and f′(1). From this figure it can be seen that u(1) will reach the axis before f′(0) becomes positive, which means that the velocity

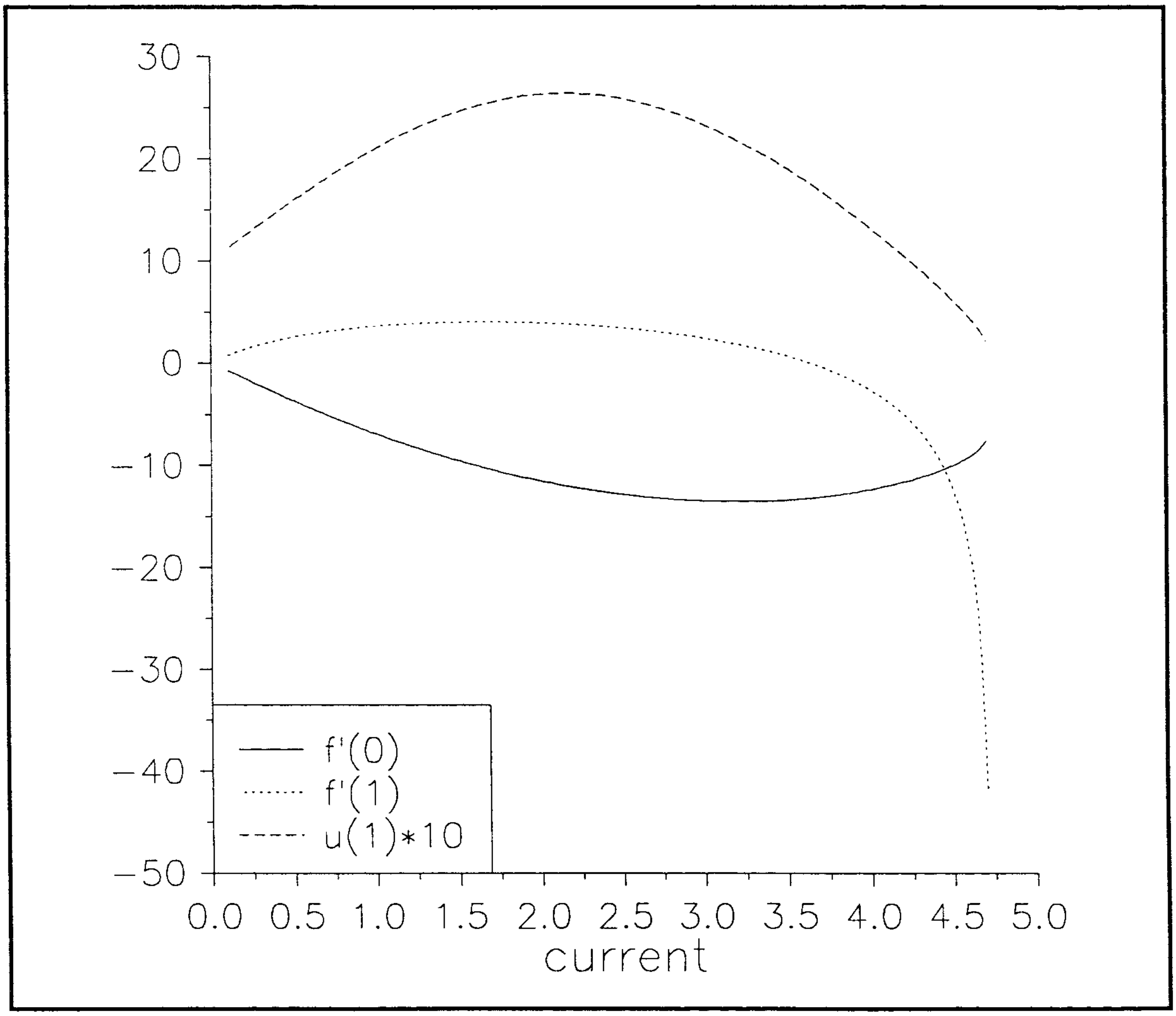

**Figure 2.18** - values of particular quantities for $\frac{\partial \gamma}{\partial T}$ $=-2*10^{-6}\mathrm{Nm^{-1}K^{-1}}$

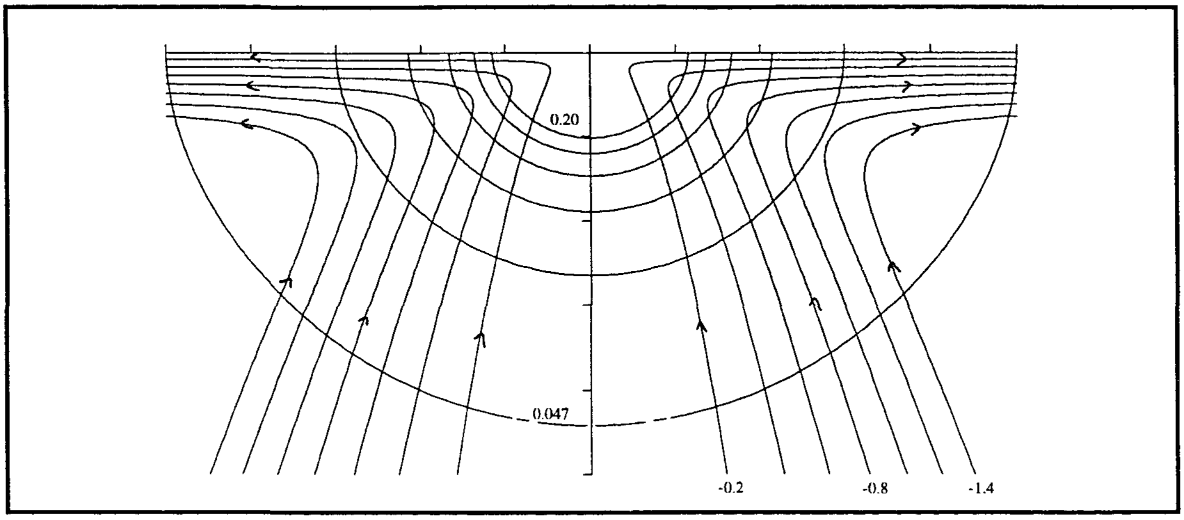

**Figure 2.19** - streamlines and isotherms for $J_0$=2.0A and $\frac{\partial\gamma}{\partial T}$=$-2*10^{-6}$Nm$^{-1}$K$^{-1}$

down the axis will become infinite while the surface tension still dominates at the top of the region, and the fluid flows outwards along the top surface. These cases are illustrated in figures 2.19 to 2.21 and discussed below.

Figure 2.19 shows the streamlines and isotherms at 2.0 A, where the flow has a single loop, and moves outward on the top surface. This figure has a similar appearance to figure 2.12.

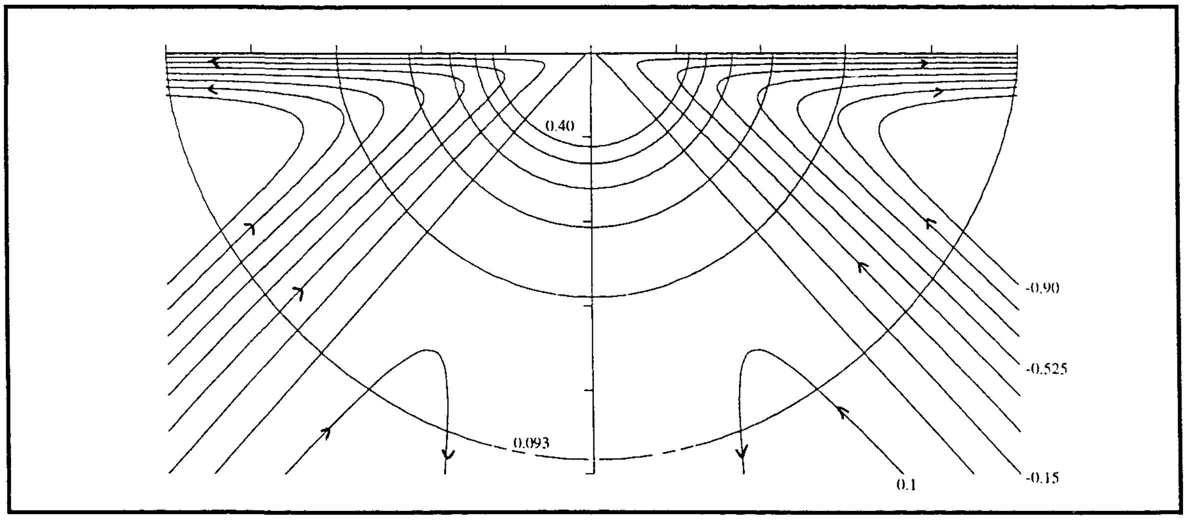

**Figure 2.20** - streamlines and isotherms for $J_0$=4.0A and $\frac{\partial\gamma}{\partial T}$=$-2*10^{-6}$Nm$^{-1}$K$^{-1}$

Figure 2.20 depicts the flow at 4.0 A, where the electromagnetic forces are starting to dominate the flow, with a downward flow near the axis, but a strong outward flow remains along the top surface. The appearance of this flow is similar to that in figure 2.13.

Figure 2.21 shows the case just short of breakdown, at 4.65 A. Comparing this with figure 2.14 it can be seen that, although the two flow loops are approximately the same size, the flow down the axis in figure 2.21 is much stronger and the development of a jet structure is clearly visible. Also, the isotherms are no longer completely spherically, but are stretched down the axis due to the greater importance of convection.

The evolution of flow patterns for $\frac{\partial \gamma}{\partial T} = -2*10^{-6}\,Nm^{-1}K^{-1}$ is typical of that for 'large' values of $\frac{\partial \gamma}{\partial T}$, with the flow being surface tension dominated at low currents. As the current is increased, the electromagnetic forces dominate in a region near the axis, but before they can dominate everywhere, the velocity down the axis become infinite and breakdown occurs. Figure 2.22 shows the flow patterns attainable for various negative values of $\frac{\partial \gamma}{\partial T}$, at different current values. The lines on the graph separate three regions of flow.

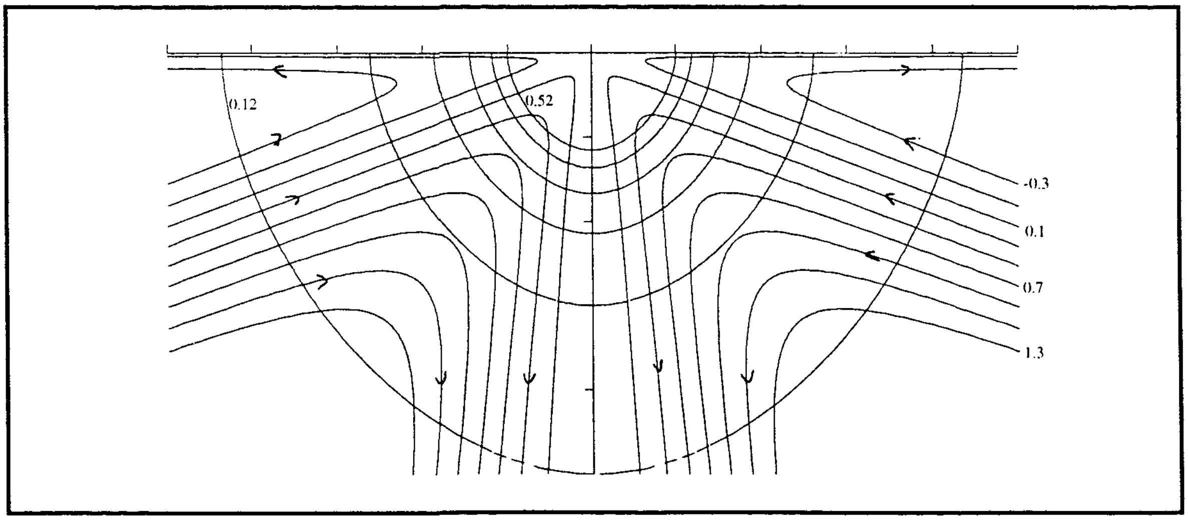

**Figure 2.21** - streamlines and isotherms for $J_0$=4.65A and $\frac{\partial \gamma}{\partial T}=-2*10^{-6}Nm^{-1}K^{-1}$

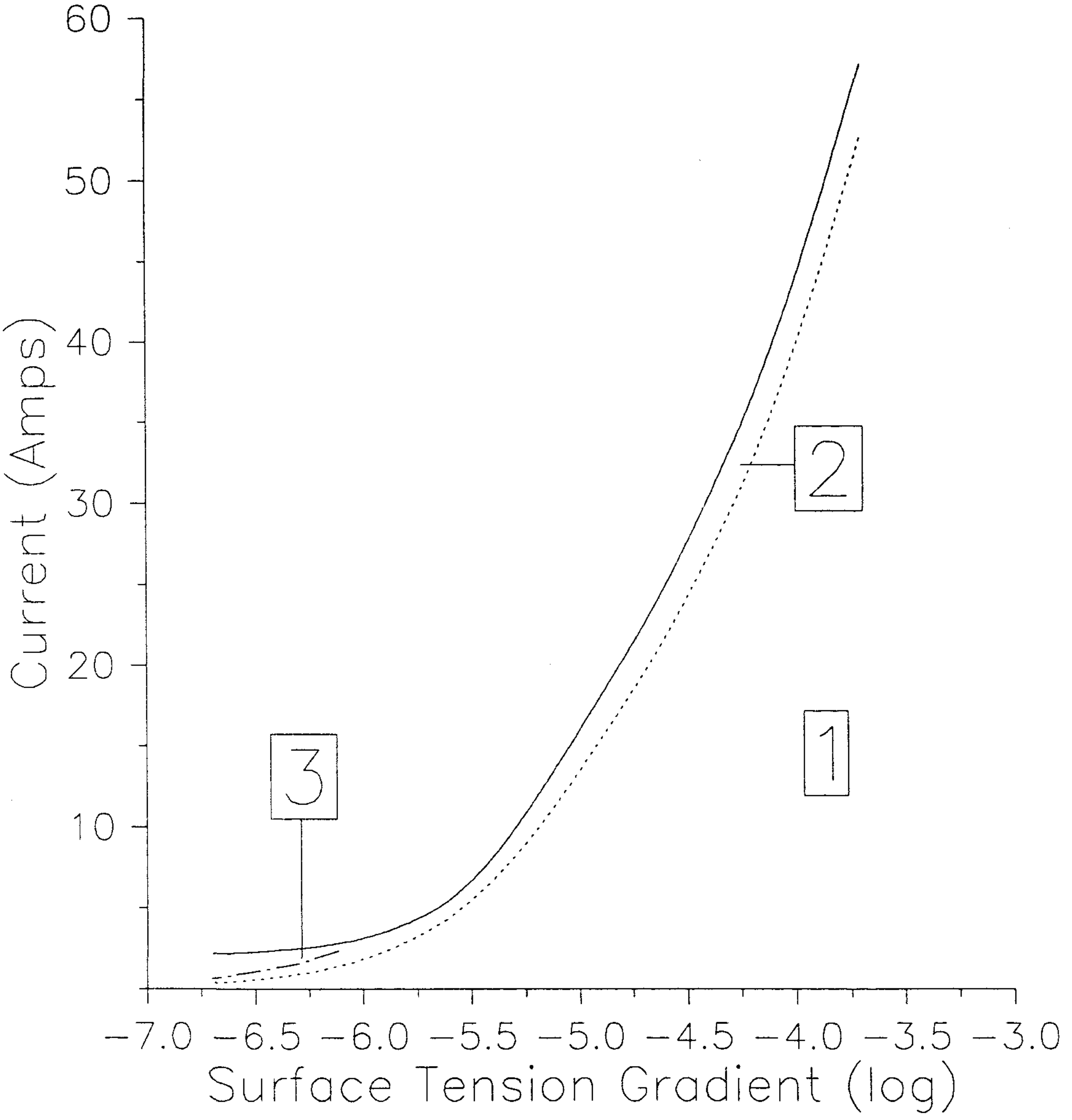

**Figure 2.22** - Breakdown current for negative $\frac{\partial\gamma}{\partial T}$

Region 1 is the surface tension dominated single loop flow, with the fluid flowing up the axis and outwards along the top surface

Region 2 is where neither force dominates and a two loop flow exists, outward along the top surface, down the axis and inwards at some value of $\mu$ between 0 and 1.

Region 3 is the single loop flow dominated by electromagnetic forces, with the fluid flowing inwards along the top surface and then down the axis.

The solid line depicts the current value at which, for a given $\frac{\partial \gamma}{\partial T}$, the velocity down the axis becomes infinite, and the similarity solution ceases to exist.

Figure 2.22 also shows that a large negative value for $\frac{\partial \gamma}{\partial T}$ causes a large increase in the value of the current at which breakdown occurs. It is possible, in these situations, to obtain a similarity solution for the flow for realistic current values. In practice, values for $\frac{\partial \gamma}{\partial T}$ of magnitude $10^{-4}$ and larger are possible for real materials, and so the existence of the similarity solution at high currents is important.

It should also be noted from figure 2.22 that in the limit as $\frac{\partial \gamma}{\partial T}$ tends to zero the breakdown current tends to a value slightly below 2.1A. From figure 2.9 it can be seen that this is consistent with the case when $\frac{\partial \gamma}{\partial T}$ is tending to zero from above. These limiting values are lower than the breakdown current obtained by Sozou [ 97 ] in his original model. The breakdown current obtained in that case was about 3.7A. However, Sozou assumed that the top surface was a plane wall, and hence that the velocity on the top surface would be zero. This would obviously slow down the fluid flow, and hence delay flow breakdown. Not surprisingly, therefore, a higher breakdown current occurs in his work than for this model with a free surface.

# Chapter 3: Azimuthal Flow

## 3.1: Introduction

Heiple and Roper [ 42 ] have shown experimentally that an azimuthal rotation is possible in a weld pool, and Bojarevics and Shcherbinin [ 10 ] demonstrated that a hemispherical bowl of mercury undergoing inward flow can start rotating if the applied current is sufficiently large, above about 15A in their case. Woods and Milner [ 113 ] also considered a hemispherical bowl of mercury and showed that altering the orientation of the lead drawing the current from the bowl could create a rotating flow.

Bojarevics and Shcherbinin suggested that the rotation could be due to a non-zero azimuthal component in the electromagnetic force, caused by a non-zero meridional component in the magnetic field. The latter might be caused in practice by the return current path not being perfectly symmetric, or just by the Earth's magnetic field. In [ 10 ] they added a meridional component of magnetic field to the model adopted by Sozou [ 97 ], a component that was considerably smaller than the self induced magnetic field. The pair of ODE's obtained was then solved using the semi-analytical Galerkin (spectral) method [ 76 ]. They showed that on approaching the parameter value $K=K_c$, at which flow breakdown would occur for the Sozou problem, the fluid starts to rotate considerably faster. In addition the fluid velocity down the axis of symmetry reaches a maximum at $K=K_c$ and then decreases as K increases further. The solutions of Bojarevics and Shcherbinin also showed that when $K>K_c$, the azimuthal velocity does not tend to zero if the azimuthal force is gradually reduced to zero.

In this chapter the approach of Bojarevics and Shcherbinin is applied to the model in Chapter 2.

## 3.2: The Model

The physical model is unchanged from that of Chapter 2, except that the magnetic field is now of the form $\mathbf{B} = \mathbf{B}_s + \mathbf{B}_0$, where $\mathbf{B}_s$ is the self-induced magnetic field given earlier,

$$\boldsymbol{B}_s = \frac{J_0\mu_0(1-\mu)}{2\pi r(1-\mu^2)^{1/2}}\hat{\varphi}, \tag{3.1}$$

and $\mathbf{B}_0$ is the new applied magnetic field.

Ampere's law states

$$\nabla\times\boldsymbol{B} = \mu_0\boldsymbol{J}.$$

It is convenient to chose a form for $\mathbf{B}_0$ such that $\nabla\times\boldsymbol{B}_0$ is zero, since this leaves the form for $\mathbf{J}$ unchanged and means that a similarity solution similar to that of Chapter 2 might still be possible. The quantity $\mathbf{B}_0$ must also satisfy Maxwell's equation $\nabla.\boldsymbol{B}_0 = 0$. One such form for $\mathbf{B}_0$ is

$$\boldsymbol{B}_0 = \frac{\varepsilon\mu_0 J_0}{2\pi r}\left( C\,, \frac{C\mu+D}{(1-\mu^2)^{1/2}}\,, 0 \right) \tag{3.2}$$

where C, D and $\varepsilon$ are constants. The parameter $\varepsilon$ is a small number, which gives the relative sizes of the self-induced and external magnetic fields. The values for C and D were chosen to be -1 and 1 to remove the singularity at $\mu=1$, which leads to a parabolic field in the meridional plane and a form for $\mathbf{B}_0$ which is very similar to $\mathbf{B}_s$.

As in Chapter 2, the governing equations are given by:

the curl of the Navier-Stokes equation

$$-\nabla\times(\mathbf{v}\times(\nabla\times\mathbf{v})) = -\nu\nabla\times(\nabla\times(\nabla\times\mathbf{v})) + \frac{1}{\rho}\nabla\times(\mathbf{J}\times\mathbf{B}); \tag{3.3}$$

incompressible fluid

$$\nabla.\mathbf{v} \equiv 0; \tag{3.4}$$

heat transfer equation

$$\mathbf{v}\,.\nabla T = \kappa\nabla^2 T. \tag{3.5}$$

Since $\mathbf{B}_0$ is independent of $\phi$, it is reasonable to assume that the solution to equations (3.3), (3.4), and (3.5) will also be independent of $\phi$. The velocity (2.17) now has an additional azimuthal component, and is expressed

$$\mathbf{v} = \left( \frac{-\nu f'(\mu)}{r}, \frac{-\nu f(\mu)}{r(1-\mu^2)^{1/2}}, \mathrm{v}_\varphi(r,\mu) \right). \tag{3.6}$$

Since $\mathrm{v}_\phi$ is independent of $\phi$, the continuity equation (3.4) is identically satisfied by (3.6). A similarity solution can again be found with $\mathrm{v}_\phi$ of the form

$$\mathrm{v}_\varphi = \frac{\nu}{r} \frac{l(\mu)}{(1-\mu^2)^{1/2}}, \tag{3.7}$$

where $l(\mu)$ is a new function.

The temperature T is left unchanged from (2.24) as

$$T = \frac{1}{r} g(\mu).$$

Since T is independent of $\phi$, equation (3.5) for the temperature is obviously unchanged from (2.27) by the addition of the azimuthal velocity component, and remains

$$g' = \frac{\nu f g}{\kappa(1-\mu^2)}. \tag{3.8}$$

However, the introduction of the azimuthal velocity component and the applied magnetic field $\mathbf{B}_0$ changes the equation for the fluid flow. So consider again the Navier-Stokes equation (3.3).

Firstly look at the inertial term in (3.3). Recalling that the model is axially symmetric, and hence all $\varphi$-derivatives are identically zero, and that $\mathbf{v}$ is given by (3.6), it follows that

$$\nabla \times \mathbf{v} = -\hat{\boldsymbol{r}} \frac{\nu l'}{r^2} - \hat{\Phi} \frac{(1-\mu^2)^{1/2} \nu f''}{r^2}, \tag{3.9}$$

$$\mathbf{v} \times (\nabla \times \mathbf{v})) = \hat{\boldsymbol{r}} \frac{\nu^2 f f'}{r^3} - \hat{\theta} \frac{\nu^2}{r^3} \left[ (1-\mu^2)^{1/2} f' f'' + \frac{l l'}{(1-\mu^2)^{1/2}} \right] - \hat{\Phi} \frac{\nu^2 f l'}{r^3 (1-\mu^2)^{1/2}},$$

$$\begin{aligned} \nabla \times (\mathbf{v} \times (\nabla \times \mathbf{v})) = {} & \hat{\boldsymbol{r}} \frac{\nu^2}{r^4} (f' l' + f l'') - \hat{\theta} \frac{2\nu^2 f l'}{r^4 (1-\mu^2)^{1/2}} \\ & + \hat{\Phi} \frac{\nu^2}{r^4} \left\{ \frac{2 l l'}{(1-\mu^2)^{1/2}} + 3(1-\mu^2)^{1/2} f' f'' + (1-\mu^2)^{1/2} f f''' \right\}. \end{aligned} \tag{3.10}$$

Now considering the viscous term the following are obtained,

$$\nabla\times(\nabla\times \mathbf{v}) = \hat{\boldsymbol{r}}\,\frac{\nu}{r^3}[(1-\mu^2)f''' - 2\mu f''] - \hat{\theta}\,\frac{\nu}{r^3}(1-\mu^2)^{1/2}f'' - \hat{\Phi}\,\frac{\nu}{r^3}(1-\mu^2)^{1/2}l'',$$

$$\nabla\times(\nabla\times(\nabla\times \mathbf{v})) = \hat{\boldsymbol{r}}\,\frac{\nu}{r^4}[(1-\mu^2)l''' - 2\mu l''] - \hat{\theta}\,\frac{2\nu(1-\mu^2)^{1/2}l''}{r^4}$$
$$+\hat{\Phi}\,\frac{\nu}{r^4}\Big[-4\mu(1-\mu^2)^{1/2}f''' + (1-\mu^2)^{3/2}f''''\Big]. \qquad (3.11)$$

Finally from (3.1), (3.2) and (2.9) it can be shown that the electromagnetic term is

$$\boldsymbol{J}\times\boldsymbol{B} = -\,\hat{\theta}\,\frac{J_0^2\mu_0(1-\mu)}{4\pi^2r^3(1-\mu^2)^{1/2}} + \hat{\Phi}\,\frac{J_0^2\mu_0\,\varepsilon(1-\mu)}{4\pi^2r^3(1-\mu^2)^{1/2}},$$

and hence its curl is

$$\nabla\times(\boldsymbol{J}\times\boldsymbol{B}) = \hat{\boldsymbol{r}}\,\frac{J_0^2\mu_0\,\varepsilon}{4\pi^2r^4} + \hat{\theta}\,\frac{J_0^2\mu_0\,\varepsilon}{2\pi^2r^4}\,\frac{(1-\mu)}{(1-\mu^2)^{1/2}} + \hat{\Phi}\,\frac{J_0^2\mu_0}{2\pi^2r^4}\,\frac{(1-\mu)}{(1-\mu^2)^{1/2}}. \qquad (3.12)$$

Using the results obtained above ( (3.10), (3.11) and (3.12) ), the three components of equation (3.3) can be written as

$$\hat{\boldsymbol{r}}:\ \frac{\nu^2}{r^4}(f'l' + fl'') - \frac{\nu^2}{r^4}[(1-\mu^2)l''' - 2\mu l''] + \frac{J_0^2\mu_0\,\varepsilon}{4\pi^2\rho r^4} = 0, \qquad (3.13)$$

$$\hat{\theta}:\ -\frac{2\nu^2 fl'}{r^4(1-\mu^2)^{1/2}} + \frac{2\nu^2(1-\mu^2)^{1/2}l''}{r^4} + \frac{J_0^2\mu_0\,\varepsilon}{2\pi^2\rho r^4}\,\frac{(1-\mu)}{(1-\mu^2)^{1/2}} = 0\,, \qquad (3.14)$$

$$\hat{\Phi}:\ \frac{\nu^2}{r^4}\left\{\frac{2ll'}{(1-\mu^2)^{1/2}} + 3(1-\mu^2)^{1/2}f'f'' + (1-\mu^2)^{1/2}ff'''\right\}$$
$$-\frac{\nu^2(1-\mu^2)^{1/2}}{r^4}\Big[-4\mu f''' + (1-\mu^2)f''''\Big] + \frac{J_0^2\mu_0}{2\pi^2\rho r^4}\,\frac{(1-\mu)}{(1-\mu^2)^{1/2}} = 0\,, \qquad (3.15)$$

On multiplying equation (3.13) by $\frac{r^4}{\nu^2}$, (3.14) by $\frac{r^4(1-\mu^2)^{1/2}}{2\nu^2}$ and (3.15) by $\frac{r^4(1-\mu^2)^{1/2}}{\nu^2}$, the equations simplify to

$$\hat{\boldsymbol{r}}:\ \frac{J_0^2\mu_0\,\varepsilon}{4\pi^2\rho\nu^2} - \Big[-2\mu l'' + (1-\mu^2)l'''\Big] + (f\,l'' + f'l') = 0, \qquad (3.16)$$

$$\hat{\theta}:\ \frac{J_0^2\mu_0\,\varepsilon}{4\pi^2\rho\nu^2}(1-\mu) + (1-\mu^2)l'' - f\,l' = 0\,, \qquad (3.17)$$

$$\hat{\Phi}: \; \frac{J_0^2\mu_0}{2\pi^2\rho\nu^2}(1-\mu) - \left[-4\mu(1-\mu^2)f''' + (1-\mu^2)^2 f''''\right]$$

$$+ \left[2l\,l' + (1-\mu^2)(ff''' + 3f'f'')\right] = 0. \qquad (3.18)$$

It is possible to integrate equation (3.18) once with respect to μ to give

$$-\frac{J_0^2\mu_0}{4\pi^2\rho\nu^2}(1-\mu)^2 - (1-\mu^2)^2 f''' + \frac{1}{2}(1-\mu^2)\left(f^2\right)'' + \mu\left(f^2\right)' - f^2 + l^2 = 0, \qquad (3.19)$$

with the constant of integration being zero after the use of boundary conditions (3.21) and (3.25) below.

It can be easily seen that equation (3.16) is just the μ-derivative of the equation (3.17), hence only two equations need to be solved, (3.17) and (3.19). These two equations are similar to those obtained by Bojarevics and Shcherbinin [ 10 ]. However, since they scaled their variables equivalent to f(μ) and l(μ) with $J_0(\mu_0/\rho)^{1/2}$, the constants in their equations were different.

Equations (3.17) and (3.19) are solved subject to the same boundary conditions for f(μ) and g(μ) as stated in Chapter 2. For convenience, these conditions are listed again below.

The top surface remaining flat requires application of

$$v_\theta(0) = 0 \;\Rightarrow\; f(0) = 0. \qquad (3.20)$$

For no fluid to cross the axis of symmetry it is necessary that

$$v_\theta(1) = 0 \;\Rightarrow\; f(1) = 0. \qquad (3.21)$$

Zero heat flux across the top surface leads to

$$\frac{\partial T}{\partial \theta} = 0 \;\Rightarrow\; g'(0) = 0. \qquad (3.22)$$

Balance of radial stress on the top surface yields

$$-\rho\nu^2 f''(0) = \frac{\partial \gamma}{\partial T}\, g(0). \qquad (3.23)$$

For a physically realistic solution it is necessary that the total heat flux is related to the total current input by

$$Q = 2\pi\rho c_p \int_0^1 g(\kappa - \nu f')\, d\mu = 6J_0. \tag{3.24}$$

Additional boundary conditions are required for $l(\mu)$ and these are obtained from the following requirements.

In order that the azimuthal fluid velocity is finite along the axis $\mu=1$ it follows, using (3.7), that

$$l(1) = 0. \tag{3.25}$$

There is also zero applied stress in the azimuthal direction on the top surface, that is

$$\sigma_{\varphi\theta} = 0 \text{ on } \mu = 0. \tag{3.26}$$

Since $v_\phi$ is independent of $\phi$, the general expression for $\sigma_{\phi\theta}$ becomes

$$\sigma_{\varphi\theta} = \rho\nu\left(\frac{-(1-\mu^2)^{1/2}}{r}\frac{\partial v_\varphi}{\partial\mu} - \frac{v_\varphi \mu}{r(1-\mu^2)^{1/2}}\right),$$

and on using (3.7) it can be written

$$\sigma_{\varphi\theta} = -\frac{\rho\nu^2}{r^2}\left(\frac{2l\mu}{(1-\mu^2)} + l'\right).$$

Application of condition (3.26) then yields

$$l'(0) = 0. \tag{3.27}$$

### 3.2.1: Method of solution

The system to be solved consists of equations (3.8), (3.17) and (3.19), subject to the boundary conditions (3.20), (3.21), (3.22), (3.23), (3.24), (3.25) and (3.27). To obtain the solution equations (3.5), (3.17) and (3.19) are written as a series of first order differential equations, these are then solved by the NAG routine D02HBF. This routine solves a series of first-order ordinary differential equations, using initial value techniques incorporating guesses for any unknown initial values (l(0), f′(0) and g(0) for our system.) These guesses are then corrected using Newton iteration to obtain a solution where conditions (3.24), (3.21) and (3.25) also hold to some required accuracy. In this work a tolerance of $10^{-5}$ was used. This routine was used instead of the Galerkin method used by Bojarevics and Shcherbinin [ 10 ], as the coupled boundary condition (3.23) would be problematical to apply using this method.

# 3.3: Results and discussion

When $\varepsilon<<1$ the electromagnetic force in the azimuthal direction is very small and would be expected to produce only a very small azimuthal velocity. This is indeed the case when the current is below the breakdown current for a particular value of $\frac{\partial\gamma}{\partial T}$. In fact the poloidal flow is very close to the solution obtained from the model in Chapter 2. Figures 3.1 and 3.2 show the streamlines $\frac{\psi}{\nu L}$, where L is a length and the displayed axes are L long, the scaled isotherms LT, and the scaled azimuthal velocity $\frac{\mathrm{L}v_{\varphi}}{\nu}$ at a distance L from the origin for parameter values of J=1.5A and $\frac{\partial\gamma}{\partial T}=-10^{-7}\mathrm{Nm}^{-1}\mathrm{K}^{-1}$, both with $\varepsilon=0.001$ and $\varepsilon=0$ (cases with and without an azimuthal force). The streamlines produced are virtually indistinguishable by eye, which is not surprising in view of the size of the azimuthal velocity.

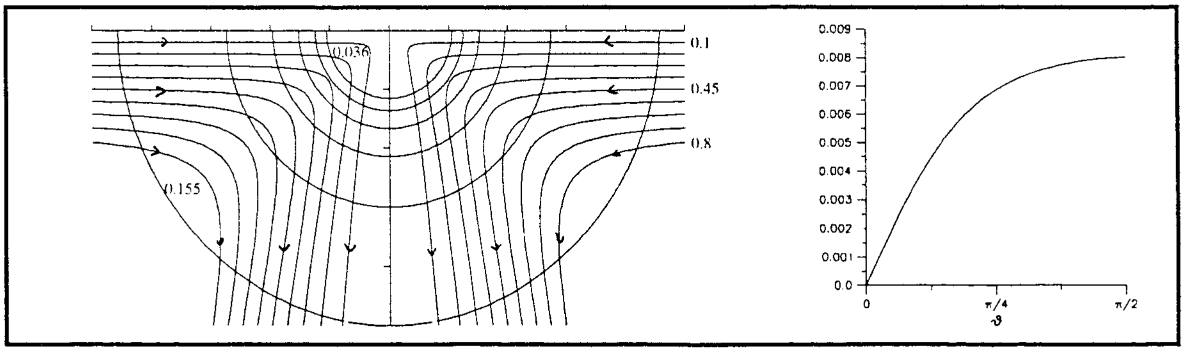

**Figure 3.1** - streamlines, isotherms and azimuthal velocity for J=1.5, $\frac{\partial\gamma}{\partial T}=-10^{-7}$, $\varepsilon=0.001$

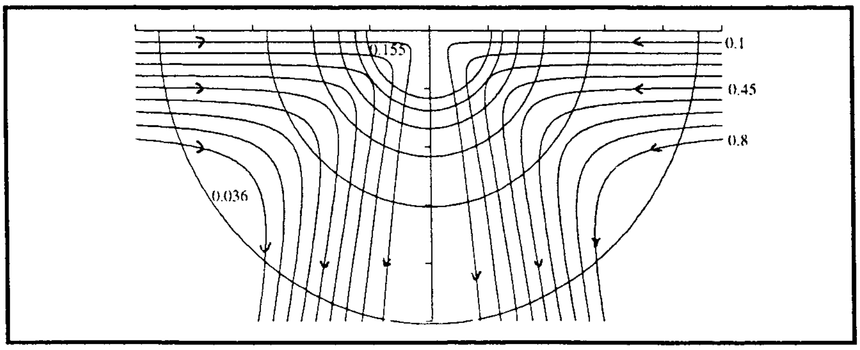

**Figure 3.2** - streamlines and isotherms for J=1.5, $\frac{\partial\gamma}{\partial T}=-10^{-7}$, $\varepsilon=0$

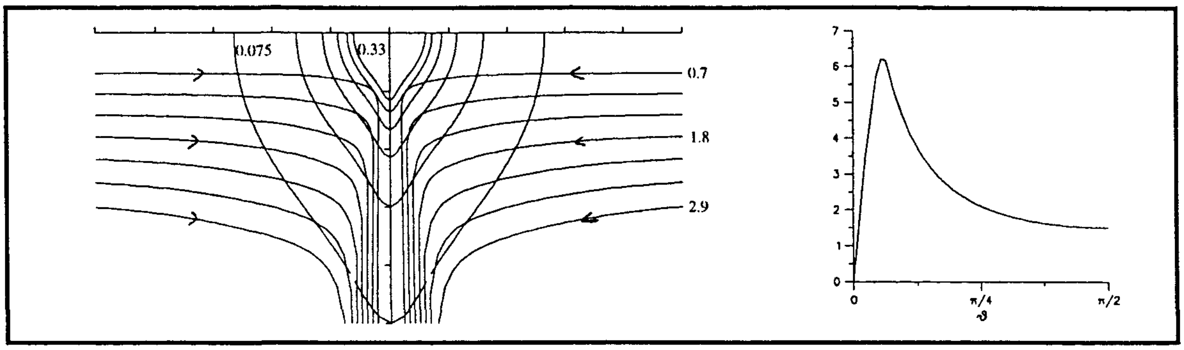

**Figure 3.3** - streamlines, isotherms and azimuthal velocity for J=2.2, $\frac{\partial\gamma}{\partial T}$=-$10^{-7}$, $\varepsilon$=0.001

As the current approaches the breakdown value and the radial velocity down the axis begins to grow rapidly, the azimuthal velocity also starts to increase to much larger values. The centrifugal force produced as a result of the rotation slows down the poloidal flow enough that although the velocity down the axis increases sharply, it does not become infinite. In fact it reaches a maximum at a value for the applied current slightly larger than the corresponding breakdown current for $\varepsilon$=0 and decreases from then on.

Figure 3.3 shows the streamlines and isotherms for $\frac{\partial\gamma}{\partial T}$=-$10^{-7}$Nm$^{-1}$K$^{-1}$, $\varepsilon$=0.001 and J=2.2A, approximately the breakdown current for this value of $\frac{\partial\gamma}{\partial T}$. From this figure a strong jet-like structure down the axis can be clearly seen, with the isotherms being elongated down the axis $\mu$=1. The azimuthal velocity has now grown to be of significant size everywhere, slowing the fluid down and preventing flow breakdown. On increasing the current to J=5A the strong jet has disappeared and the isotherms are not stretched down the axis to quite the same extent (figure 3.4).

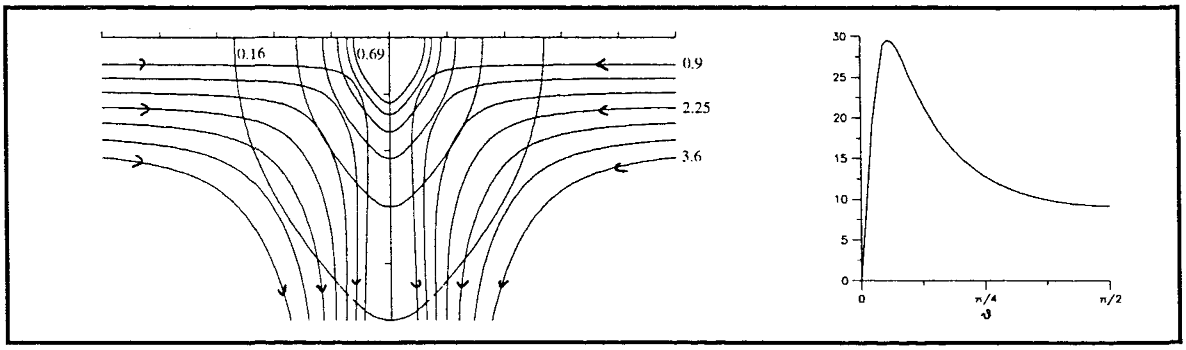

**Figure 3.4** - streamlines, isotherms and azimuthal velocity for J=5.0, $\frac{\partial\gamma}{\partial T}$=-$10^{-7}$, $\varepsilon$=0.001

Figure 3.5 shows the variation with current of l(0), f′(0) and f′(1) when $\frac{\partial\gamma}{\partial T}$=-10$^{-7}$Nm$^{-1}$K$^{-1}$ and ε=0.001. These three quantities are proportional to the azimuthal velocity on the top surface, the radial velocity on the top surface and the radial velocity down the axis of symmetry respectively. From the diagram the overall behaviour of the flow can be clearly seen, with the azimuthal velocity being very close to zero until the applied current is above 2A, and then increasing rapidly with the appearance of a perturbed pitchfork bifurcation. This appears different to the results presented by Bojarevics and Shcherbinin [ 10 ] who had their version of l(0) having a maximum then decreasing, due to the rescaling of the variables they had used. It is also clearly visible on figure 3.5 that the growth in azimuthal velocity slows down the poloidal flow, with the fluid velocity down the axis reaching a peak and the radial velocity on the top surface having a sharp drop in its rate of increase, when the azimuthal velocity grows to a significant size. Halving the size of ε to 0.0005 produces a similar diagram, figure 3.6, the only significant difference being that the maximum value for |f′(1)| has doubled.

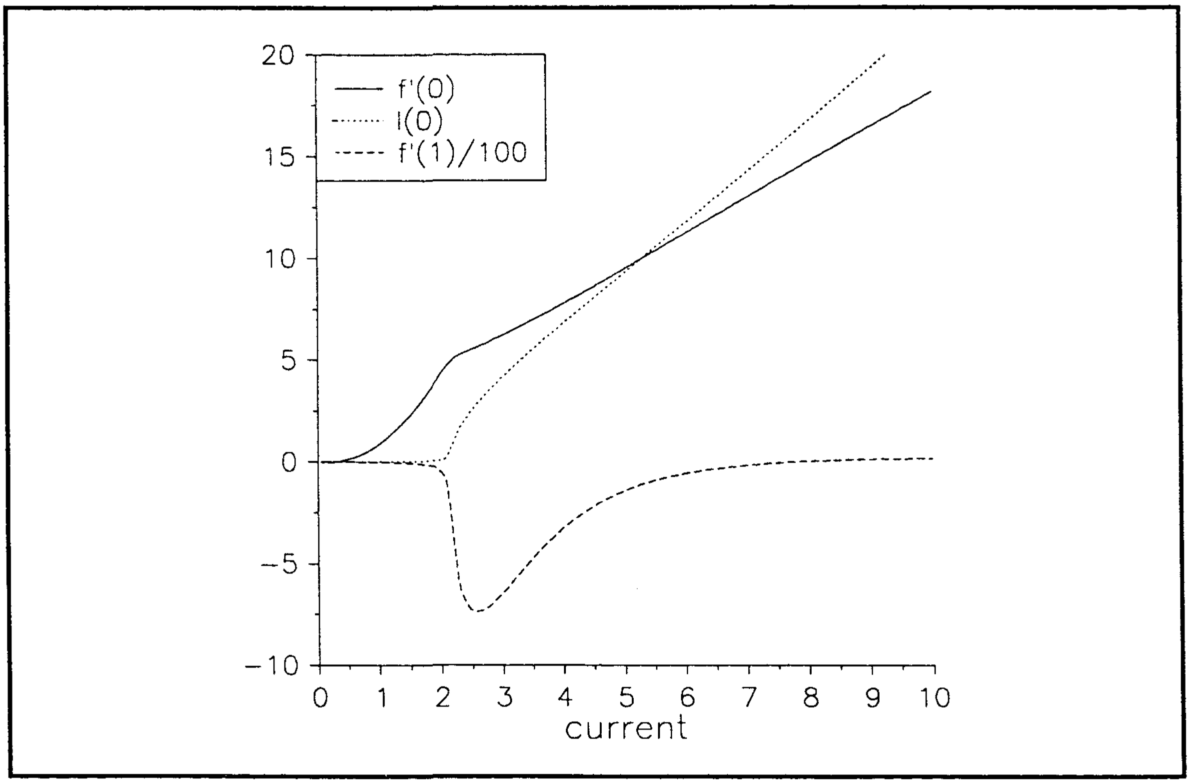

**Figure 3.5** - the variation with current of l(0), f′(0) and f′(1) when $\frac{\partial\gamma}{\partial T}$=-10$^{-7}$ and ε=0.001

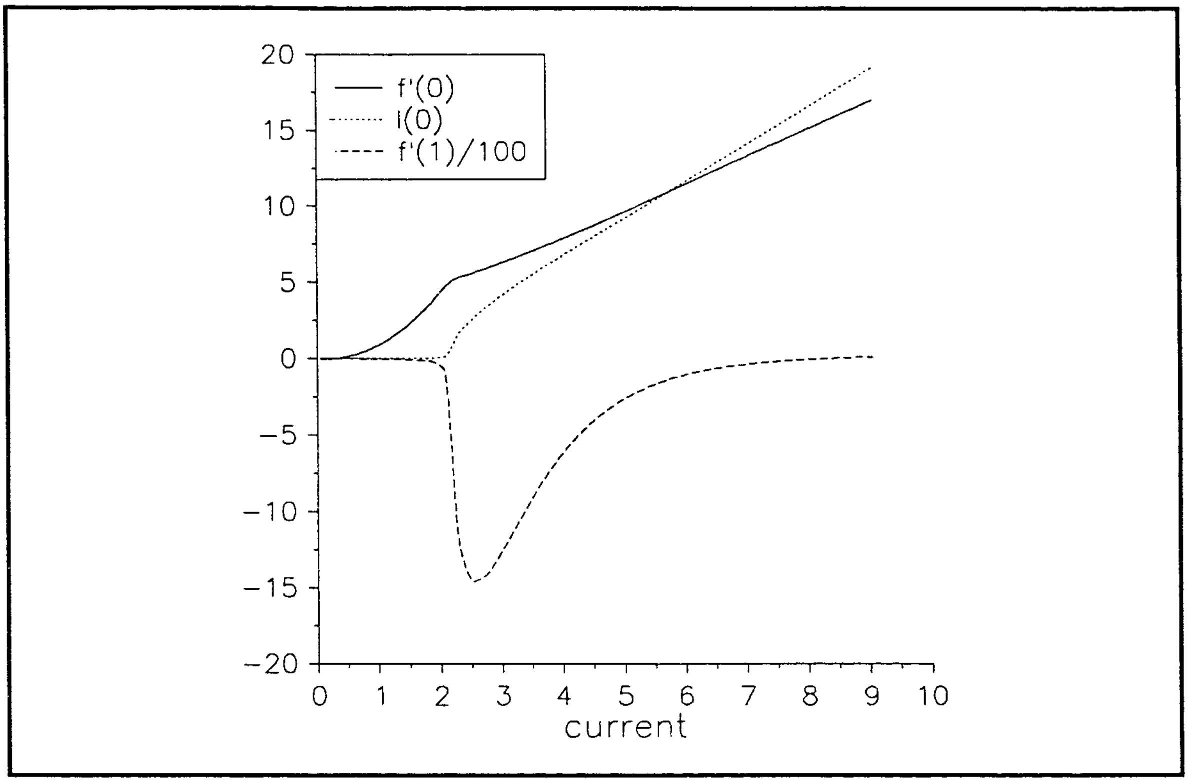

**Figure 3.6** - the variation with current of l(0), f′(0) and f′(1) when $\frac{\partial\gamma}{\partial T}=-10^{-7}$ and $\varepsilon=0.0005$

Looking in more detail at the effect of changing the size of ε, figures 3.7 and 3.8 show the variation with ε of some variables, at a fixed $\frac{\partial\gamma}{\partial T}=-10^{-7}\mathrm{Nm}^{-1}\mathrm{K}^{-1}$. Figure 3.7 shows the values of l(0) at 1A, considerably below the breakdown current, and 5A, considerably above. At 1A the azimuthal velocity tends to zero as ε, and hence the azimuthal force, tends to zero. However, at 5A the azimuthal velocity does not tend to zero, with l(0) tending to approximately 9.5. Figure 3.8 shows the values of both 1/max(|f′(1)|) and 1/f′(1) for $J_0$=5A. These tend to zero as ε approaches zero, indicating that the fluid velocity down the axis will still become infinite even if the azimuthal velocity is non-zero.

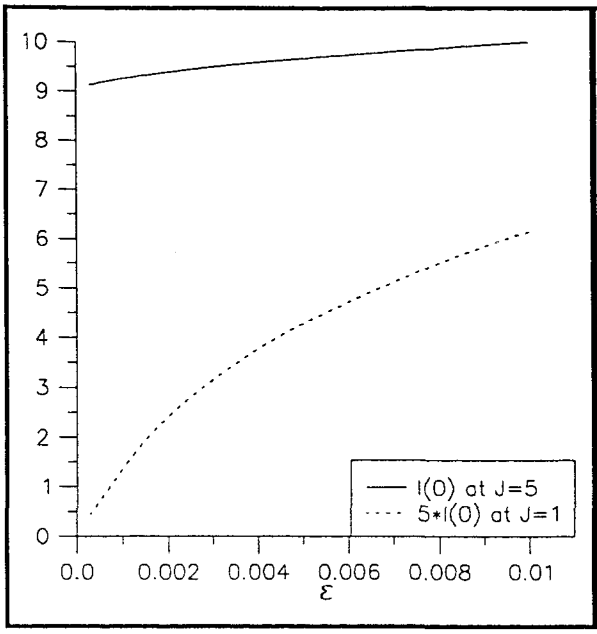

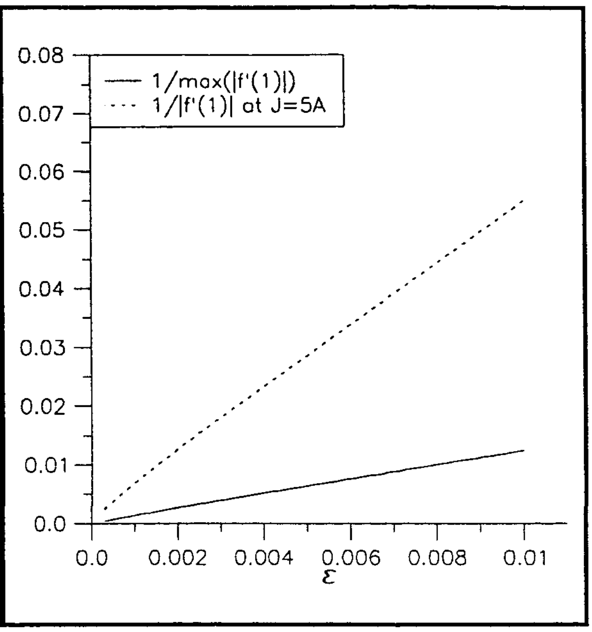

**Figure 3.7** - showing the effect of the size of ε on l(0) for $\frac{\partial\gamma}{\partial T}$=-$10^{-7}$

**Figure 3.8** - showing the effect of the size of ε on f′(1) for $\frac{\partial\gamma}{\partial T}$=-$10^{-7}$

Figure 3.9 shows the effect of increasing the strength of the surface tension force, with $\frac{\partial\gamma}{\partial T}$=-$10^{-6}$Nm$^{-1}$K$^{-1}$ and with ε=0.001. From this diagram it can be seen that the curves for f′(1) and l(0) are qualitatively the same as for the case $\frac{\partial\gamma}{\partial T}$=-$10^{-7}$Nm$^{-1}$K$^{-1}$, but with the current value at which the rapid increase occurs now being at the higher value of about 3.2A. The quantity f′(0) behaves differently, due to the larger surface tension force, with the fluid in this case flowing outwards along the top surface at low currents. However, as l(0) increases to values above unity, f′(0) shows a sharp decreases in its rate of increase, the same behaviour as with the smaller value of $\left|\frac{\partial\gamma}{\partial T}\right|$.

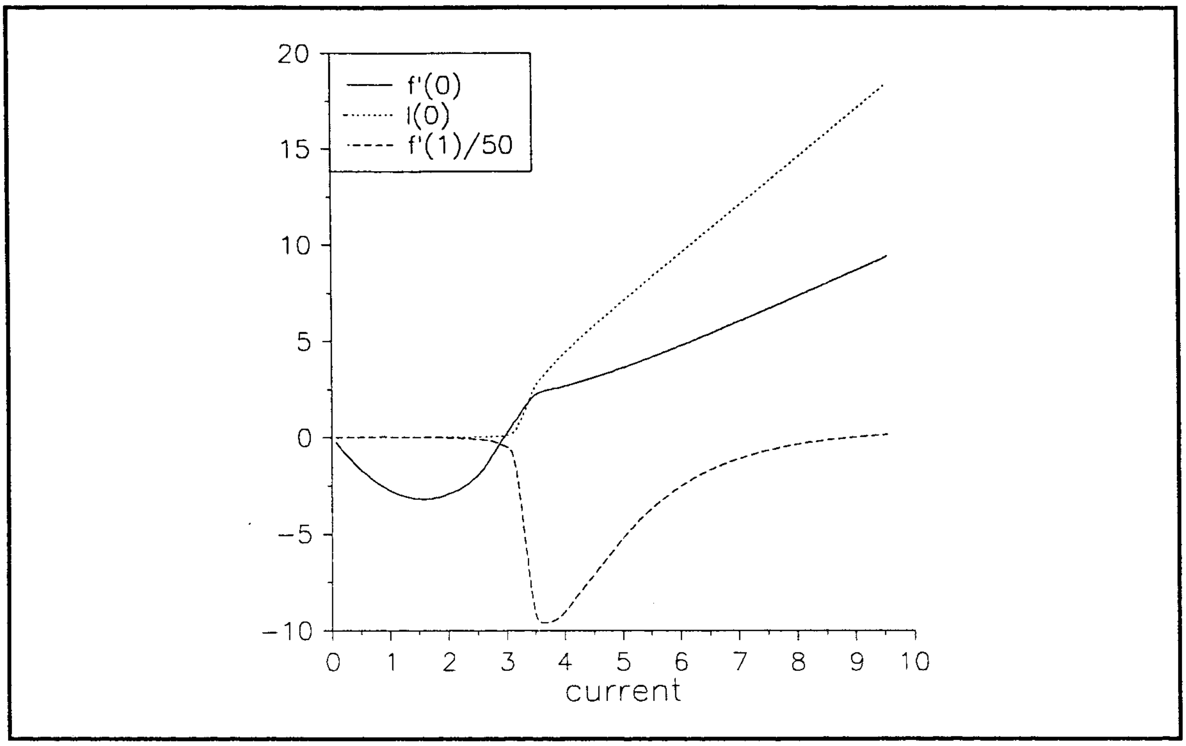

**Figure 3.9** - the variation with current of l(0), f′(0) and f′(1) when $\frac{\partial \gamma}{\partial T}$=-10$^{-6}$ and ε=0.001

Similar results are also obtained for positive values of $\frac{\partial \gamma}{\partial T}$. Figure 3.10 shows the values of l(0), f′(0) and f′(1) for $\frac{\partial \gamma}{\partial T}$=10$^{-7}$Nm$^{-1}$K$^{-1}$ and ε=0.001. Figures 3.11 and 3.12 show the variation with ε of some variables, for $\frac{\partial \gamma}{\partial T}$=10$^{-7}$Nm$^{-1}$K$^{-1}$: l(0) at 1A and 5A; and 1/max(|f′(1)|) and 1/f′(1) for $J_0$=5A.

No solutions above the breakdown current for values of $\left|\frac{\partial \gamma}{\partial T}\right|$ greater than 2*10$^{-6}$Nm$^{-1}$K$^{-1}$ were obtained, since the numerical routine failed to converge.

Figures 3.13 and 3.14 show some flow variables for positive and negative values of $\frac{\partial \gamma}{\partial T}$ respectively. These variables are:

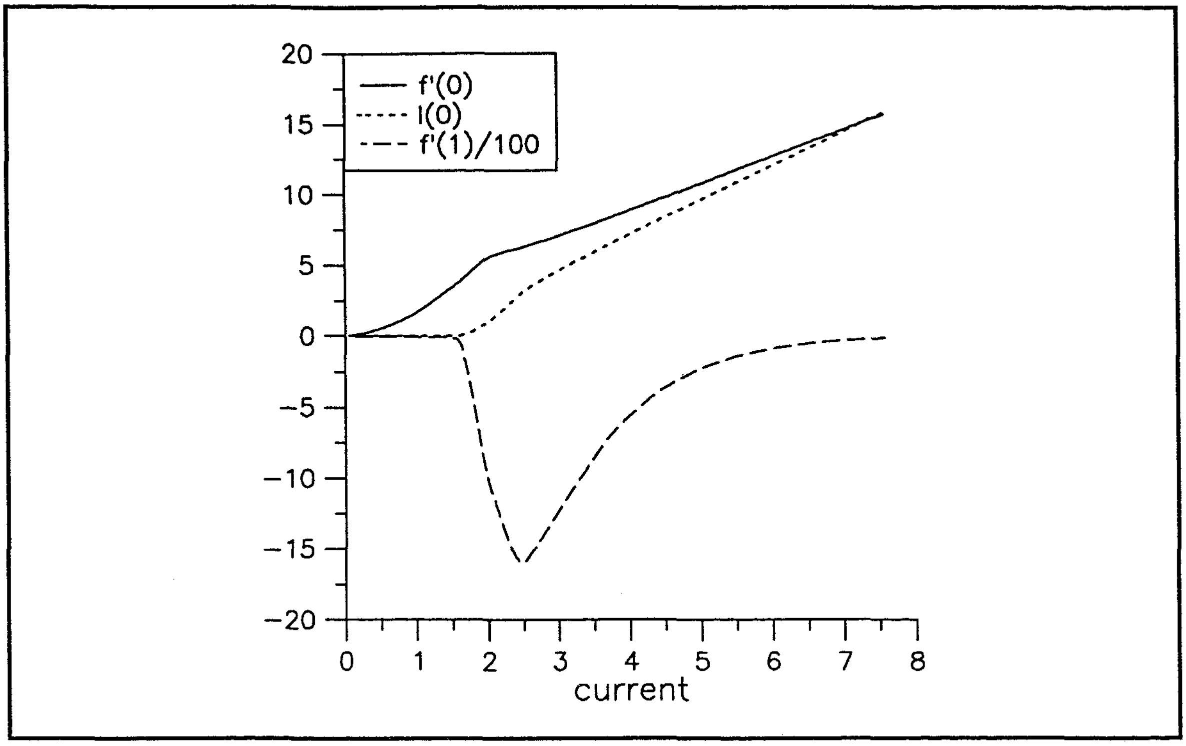

**Figure 3.10** - the variation with current of l(0), f′(0) and f′(1) when $\frac{\partial\gamma}{\partial T}=10^{-7}$ and ε=0.001

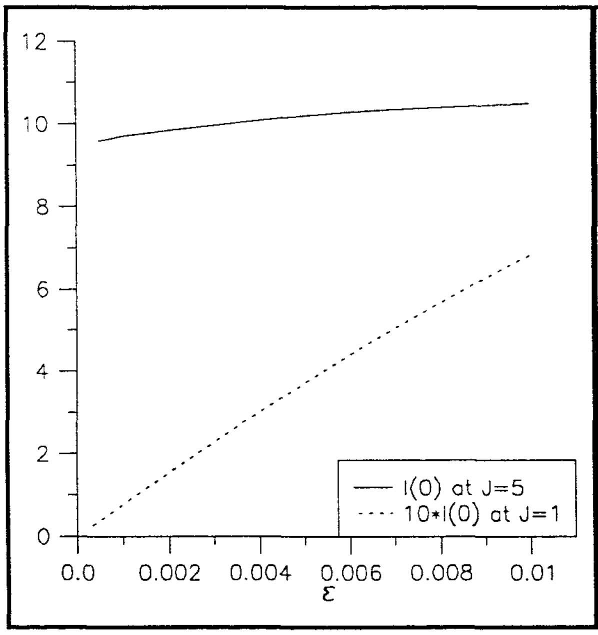

**Figure 3.11** - showing the effect of the size of ε on l(0) for $\frac{\partial\gamma}{\partial T}=10^{-7}$

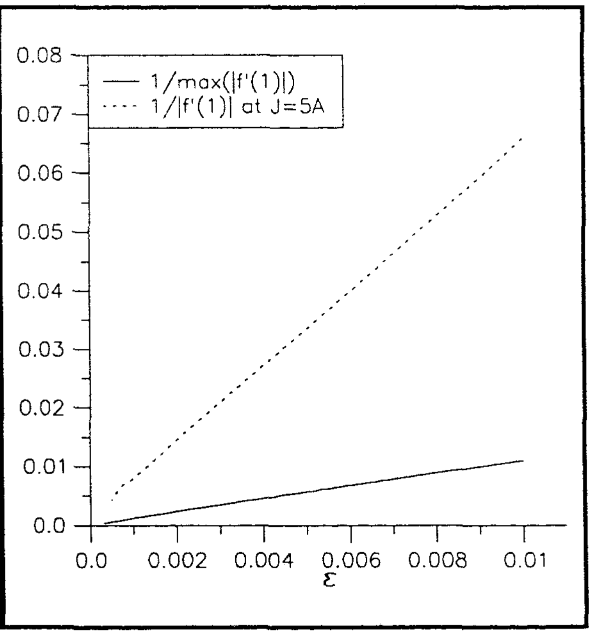

**Figure 3.12** - showing the effect of the size of ε on f′(1) for $\frac{\partial\gamma}{\partial T}=10^{-7}$

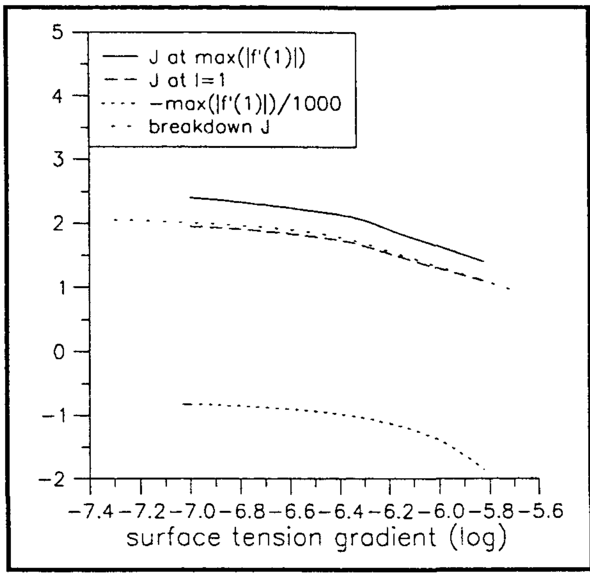

**Figure 3.13** - showing the effect of the size of ε on l(0) for $\frac{\partial\gamma}{\partial T}=+10^{-7}$

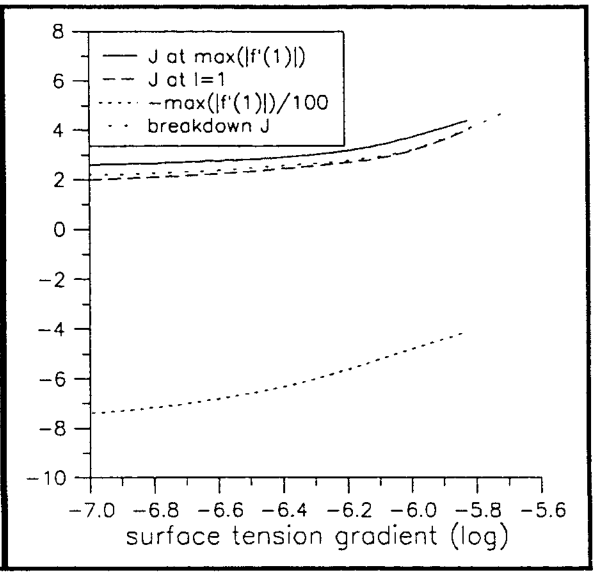

**Figure 3.14** - showing the effect of the size of ε on l(0) for $\frac{\partial\gamma}{\partial T}=-10^{-7}$

max(|f′(1)|), indicating the maximum velocity down the axis for a given $\frac{\partial\gamma}{\partial T}$;

the current value at which this occurs;

the current value when l(0)=1, when the weld pool undergoes its rapid increase in azimuthal velocity;

the breakdown current for the equivalent solution with no azimuthal force, from Chapter 2.

From these diagrams it can be seen that the maximum axial velocity does not tend to infinity as $\left|\frac{\partial\gamma}{\partial T}\right|$ increases, which would seem to indicate that the problems with obtaining solutions is numerical. It should also be noted that the value of the applied current at which the maximum axial velocity occurs and that at which l(0) goes through 1 come closer together as $\left|\frac{\partial\gamma}{\partial T}\right|$ increases, indicating a more rapid growth in l. More importantly it can be seen that the current value at which l(0)=1, while below the breakdown current for $\left|\frac{\partial\gamma}{\partial T}\right|=10^{-7}Nm^{-1}K^{-1}$, approaches it more closely as $\left|\frac{\partial\gamma}{\partial T}\right|$ is increased. Hence it can be concluded that as $\left|\frac{\partial\gamma}{\partial T}\right|$ increases the fluid does not start to spin until values of the current are much closer to the breakdown current. To prevent flow breakdown the azimuthal velocity then undergoes a more rapid increase. It is not clear at present whether the inability to obtain solutions at high currents for large $\left|\frac{\partial\gamma}{\partial T}\right|$ is due to the azimuthal velocity not increasing sufficiently rapidly to prevent the axial velocity from becoming infinite, or is a result of the numerical method being unable to work because of the presence of large gradients.

# Chapter 4: Solution in a Hemisphere

## 4.1 Introduction

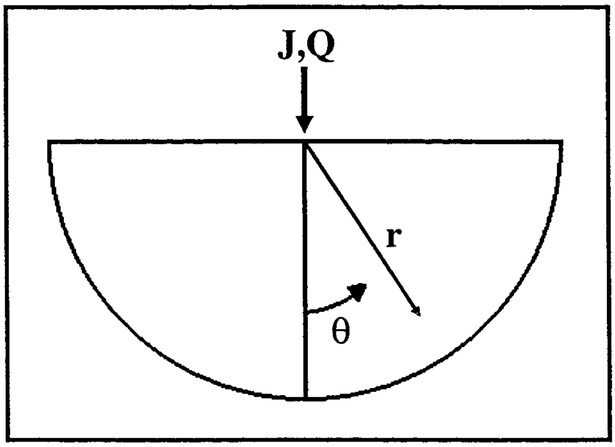

**Figure 4.1:**The geometry for the model

An obvious and major omission in the models presented in the previous chapters is the fact that a real weld pool is finite in size. In an attempt to rectify this omission, in this chapter a model is presented in which the weld pool is approximated by a hemispherical bowl. In practice the position of the outer surface of a weld pool is determined by the isotherm at the melting temperature, but the investigation of the flow in a hemispherical bowl should give a reasonable indication of the qualitative nature of the flow in the real weld pool.

On changing to a finite hemispherical geometry the previous similarity solutions no longer exist. The stream function and the temperature are now given by unknown functions of r and θ, which means that instead of solving a series of coupled ODE's it is now necessary to solve a series of coupled PDE's. This obviously requires a different method of solution.

Since it is not possible to use a similarity solution in this model it seems appropriate to include also the previously omitted buoyancy forces. The Boussinesq approximation is introduced: the change in density due to temperature is ignored in all terms apart from the buoyancy. Although the changes produced by the addition of bouyancy to the model are in most cases relatively small (<10% change) [ 58 ], it can in some cases cause a major change in the qualitative structure of the flow and so the term is included in the model for greater realism.

In this chapter, because of the geometry of the weld pool, an axisymmetric solution is assumed, without any form of azimuthal rotation, but this postulate is relaxed in the stability analysis discussed in the next chapter.

The governing equations will be solved numerically using finite differences. Second derivatives are approximated using central differences, with first derivatives being approximated by the method introduced by Leonard [ 59 ], which provides more accurate results than the methods traditionally used. The resulting set of finite difference equations are then solved using Successive Under Relaxation (SUR).

## 4.2 Deriving the equations

Recalling the original vector equations (2.3) and (2.4), the fluid flow is governed by the following equations

$$-\nabla\times(\mathbf{v}\times(\nabla\times\mathbf{v})) = -\nu\nabla\times(\nabla\times(\nabla\times\mathbf{v})) + \frac{1}{\rho}\nabla\times(\boldsymbol{J}\times\boldsymbol{B}) + \frac{1}{\rho}\nabla\times\boldsymbol{F_B}, \qquad (4.1)$$

$$\nabla.\mathbf{v} \equiv 0. \qquad (4.2)$$

The additional term on the far right of equation (4.1) is the term describing the buoyancy force in the liquid.

The temperature distribution is described by the following equation:

$$\mathbf{v}.\nabla T = \kappa\nabla^2 T. \qquad (4.3)$$

The flow is subject to the same boundary conditions on the axis and top surface as for the initial problem, that is conditions (2.5), (2.7) and (2.8), with additional ones for the outer hemisphere ( conditions (4.15) and (4.23) ), and the origin ((4.17) and (4.24) ).

The symmetry of the problem suggests that, as in Chapter 2, **v** is axisymmetric with no azimuthal component, and hence a stream function $\psi$ can be introduced, such that

$$\mathbf{v} = -\left(\frac{1}{r^2}\frac{\partial\psi}{\partial\mu}, \frac{1}{r(1-\mu^2)^{1/2}}\frac{\partial\psi}{\partial r}, 0\right) \qquad (4.4)$$

The continuity equation (4.2) is therefore satisfied identically. The stream function $\psi$ now depends on r and $\theta$, and is written as $\psi = \nu r g(\lambda,\mu)$, where $\mu$=cos $\theta$, $\lambda$=r/a and a is the radius of the hemisphere. Substituting this form for $\psi$ into equation (4.4) gives

$$\mathbf{v} = -\frac{\nu}{r}\left(g_\mu, \frac{g+\lambda g_\lambda}{(1-\mu^2)^{1/2}}, 0\right). \qquad (4.5)$$

T is now also dependent on r and $\theta$, and is written in the form

$$T = \frac{T_m\, a}{r}\, t(\mu,\lambda), \qquad (4.6)$$

where $T_m$ is the melting temperature, with t($\mu$,$\lambda$) being non-dimensional.

Following Sozou and Pickering [ 103 ] a new variable $f(\mu,\lambda)$ is defined by

$$f = g_{\mu\mu} + \frac{(2\lambda g_\lambda + \lambda^2 g_{\lambda\lambda})}{1-\mu^2} = (\nabla\times \mathbf{v})_\Phi \frac{(-r^2)}{\nu(1-\mu^2)^{1/2}} . \tag{4.7}$$

It should be noted that in contrast to the previous chapters that the funtion g describes the stream function not the temperature and f describes the vorticity and not the stream function.Taking note of equations (4.5), (4.6) and (4.7) consider each term of equation (4.1):

$$\mathbf{v}\times(\nabla\times\mathbf{v}) = \hat{\mathbf{r}}\left(\frac{(-\nu)(g+\lambda g_\lambda)}{r\,(1-\mu^2)^{1/2}}\,\frac{(-f\,\nu)(1-\mu^2)^{1/2}}{r^2}\right)$$
$$-\,\hat{\theta}\left(\frac{-\nu g_\mu}{r}\,\frac{(-f\,\nu)(1-\mu^2)^{1/2}}{r^2}\right),$$

$$\nabla\times(\mathbf{v}\times(\nabla\times\mathbf{v})) = -\frac{1}{r}\,\hat{\Phi}\left(\frac{\partial}{\partial r}\left[\frac{(-\nu)(g+\lambda g_\lambda)}{r\,(1-\mu^2)^{1/2}}\,\frac{(-f\,\nu)(1-\mu^2)^{1/2}}{r^2}\,r\right]\right.$$
$$\left. -\,(1-\mu^2)^{1/2}\frac{\partial}{\partial\mu}\left[\frac{(-\nu g_\mu)}{r}\,\frac{(-f\,\nu)(1-\mu^2)^{1/2}}{r^2}\right]\right)$$
$$= \hat{\Phi}\,\frac{\nu^2(1-\mu^2)^{1/2}}{r^4}\left[\lambda\left(f_\mu g_\lambda - f_\lambda g_\mu\right) + 3fg_\mu + gf_\mu\right], \tag{4.8}$$

$$\nabla\times(\nabla\times\mathbf{v}) = \hat{\mathbf{r}}\,\frac{1}{r}\left[\frac{\partial}{\partial\mu}\left(\frac{(1-\mu^2)^{1/2}\,(-f\nu)(1-\mu^2)^{1/2}}{r^2}\right)\right] - \hat{\theta}\left[\frac{1}{r}\frac{\partial}{\partial r}\left(\frac{r\,(-f\,\nu)(1-\mu^2)^{1/2})}{r^2}\right)\right],$$

$$\nu\nabla\times(\nabla\times(\nabla\times\mathbf{v})) = \hat{\Phi}\,\frac{\nu}{r}\left[\frac{\partial}{\partial r}\left(\frac{\nu(1-\mu^2)^{1/2}}{r^2}\,(rf_r - f)\ r\right) + (1-\mu^2)^{1/2}\frac{\partial}{\partial\mu}\left(\frac{\nu}{r^3}\left(f_\mu(1-\mu^2) - 2\mu f\right)\right)\right]$$
$$= \hat{\Phi}\,\frac{\nu^2(1-\mu^2)^{1/2}}{r^4}\left(\lambda^2 f_{\lambda\lambda} - 2\lambda f_\lambda + (1-\mu^2)f_{\mu\mu} - 4\mu f_\mu\right), \tag{4.9}$$

$\nabla\times(\boldsymbol{J}\times\boldsymbol{B})$ is unchanged from that given in Chapter 2 as (2.11).

The buoyancy force, $\mathbf{F_B}$, can be written as

$$\boldsymbol{F_B} = -\,(\rho-\rho_m)g_e\,\mathbf{e_z}$$
$$= (\rho-\rho_m)g_e\,(\hat{\mathbf{r}}\cos\theta - \hat{\theta}\sin\theta)\ , \tag{4.10}$$

where $\rho_m$ is the density of steel at its melting temperature, $g_e$ is the acceleration due to gravity and $\mathbf{e_z}$ is a unit vector pointing in the direction of gravity. The change in density is approximated by

$$\rho - \rho_m \approx -\rho\beta(T-T_m) = -\rho\beta\left(\frac{T_m\,at}{r} - T_m\right), \tag{4.11}$$

where $\beta$ is the coefficient of expansion of the liquid metal.

From (4.10) and (4.11) it can easily be shown that

$$\frac{1}{\rho}\nabla\times F_B = -\hat{\Phi}\,\frac{g_e\,\beta T_m\,(1-\mu^2)^{1/2}a}{r^2}(-\lambda t_\lambda + t + \mu t_\mu)\;. \tag{4.12}$$

From equations (4.8), (4.9), (4.12) and (2.11), it follows that the vector equation (4.1) is reduced to a single scalar equation. On multiplying the latter by $\frac{r^4}{\nu^2(1-\mu^2)^{1/2}}$ and defining new parameters $\chi$, the Rayleigh number, and $K$ by

$$\chi = \frac{g_e\,\beta T_m\,a^3}{\nu^2}$$

and

$$K = \frac{J_0\mu_0}{\pi^2\nu^2\rho}$$

equation (4.1) can now be written

$$(1-\mu^2)f_{\mu\mu} - 4\mu f_\mu + \lambda^2 f_{\lambda\lambda} - 2\lambda f_\lambda - \frac{K}{1+\mu} + \chi\lambda^2(-\lambda t_\lambda + t + \mu t_\mu)$$
$$= 3fg_\mu + gf_\mu + \lambda(f_\mu g_\lambda - f_\lambda g_\mu)\;. \tag{4.13}$$

Equation (4.13) is identical to the one derived by Sozou and Pickering in [ 103 ] apart from the term multiplied by $\chi$, which is due to the buoyancy force.

Looking at (4.5), the boundary conditions for the flow become the following :

v finite on $\mu=1$

$$g(1,\lambda)=0\,,\; g_\lambda(1,\lambda)=0\,, \tag{4.14}$$

$\mathbf{v}=0$ on $\lambda=1$

$$g(\mu,1)=0\,,\ g_\lambda(\mu,1)=0\,, \tag{4.15}$$

$\mathbf{v}$ tangential to the top surface

$$g(0,\lambda)=0\,,\ g_\lambda(0,\lambda)=0\,, \tag{4.16}$$

the flow tends to the similarity solution at the origin

$$g(\mu,0)=g_0(\mu)\,,\ f(\mu,0)=g_0''(\mu)\,, \tag{4.17}$$

where $g_0(\mu)$ is the solution obtained in Chapter 2, and the prime denotes differentiation with respect to $\mu$.

It was shown in Chapter 2 that considering the balance of the surface stresses on the free surface of the weld pool ($\mu=0$) leads to the following relationship

$$\sigma_{r\theta}=\frac{\partial\gamma}{\partial r}=\frac{\partial\gamma}{\partial T}\frac{\partial T}{\partial r}\,,$$

which becomes

$$\rho\nu\left(\frac{1}{r}\frac{\partial v_r}{\partial\theta}-\frac{v_\theta}{r}+\frac{\partial v_\theta}{\partial r}\right)=\frac{\partial\gamma}{\partial T}\frac{\partial T}{\partial r}\,. \tag{4.18}$$

Using equation (4.5) and the boundary conditions (4.16) the condition (4.18) becomes

$$\frac{\rho\nu^2}{r^2}\left(g_{\mu\mu}+\lambda^2 g_{\lambda\lambda}\right)=\frac{1}{r^2}\frac{\partial\gamma}{\partial T}(\lambda t_\lambda-t)T_m a\,.$$

Recalling equation (4.7), the above expression can be rewritten

$$\rho\nu^2 f(\,0,\lambda)=\frac{\partial\gamma}{\partial T}T_m\,a\left[\lambda t_\lambda(0,\lambda)-t\,(\,0,\lambda)\right]. \tag{4.19}$$

Returning to the temperature equation, with the aid of expressions (4.5) and (4.6) equation (4.3) becomes

$$-\frac{\nu}{r}\left(g_\mu\,,\frac{(g+\lambda g_\lambda)}{(1-\mu^2)^{1/2}}\,,0\right)\cdot\left(\frac{-t}{r^2}+\frac{1}{ar}t_\lambda\,,-\frac{(1-\mu^2)^{1/2}}{r^2}t_\mu\,,0\right)$$
$$=\kappa\left[\frac{2}{r^3}t-\frac{1}{ar^2}t_\lambda-\frac{1}{ar^2}t_\lambda+\frac{1}{a^2r}t_{\lambda\lambda}+\frac{2}{r}\left(\frac{-1}{r^2}t+\frac{1}{ar}t_\lambda\right)-\frac{\mu}{r^3}t_\mu+\frac{1}{r^2}\left(-\frac{\mu}{r}t_\mu+\frac{(1-\mu^2)}{r}t_{\mu\mu}\right)\right],$$

which, after multiplying through by $r^3$, simplifies to

$$-\nu\left(\lambda t_\lambda - t\right)g_\mu + \nu\left(g + \lambda g_\lambda\right)t_\mu = \kappa\left(\lambda^2 t_{\lambda\lambda} - 2\mu t_\mu + (1-\mu^2)t_{\mu\mu}\right). \qquad (4.20)$$

The boundary conditions for the temperature equation are as follows:

$$\frac{\partial T}{\partial \theta} = 0 \quad \text{on } \theta = \frac{\pi}{2}, \qquad \text{no heat flux across the top surface,} \qquad (4.21)$$

$$\frac{\partial T}{\partial \theta} = 0 \quad \text{on } \theta = 0, \qquad \text{no heat flux across the axis due to symmetry,} \qquad (4.22)$$

$T = T_m$, at the melting temperature on the surface of the hemisphere, (4.23)

T is equal to the corresponding similarity solution at the origin. (4.24)

## 4.3 Change to $(\eta,\lambda)$ co-ordinates

It is easily seen that equations (4.13) and (4.20) are not purely elliptical in the region of interest, since they both become parabolic on the axis $\mu=1$. Sozou and Pickering [ 103 ] encountered a similar difficulty, and showed that the change of equation type on this boundary could be removed by introducing a change of variable from $\mu$ to $\eta$, where $\eta$ is defined by

$$\eta = (1-\mu)^{1/2}. \tag{4.25}$$

A similar change of variable is used here, with the corresponding dependent variables being expressed by:

$$\begin{aligned} f(\mu,\lambda) &= F(\eta,\lambda), \\ g(\mu,\lambda) &= G(\eta,\lambda), \\ t(\mu,\lambda) &= T(\eta,\lambda). \end{aligned} \tag{4.26}$$

With the change in variable (4.25) and the variation in notation (4.26), equations (4.13), (4.7), (4.20) become

$$\begin{aligned} &(2-\eta^2)F_{\eta\eta} + \left(2\lambda G_\lambda + 2G + 6 - 7\eta^2\right)\frac{F_\eta}{\eta} + 4\lambda^2 F_{\lambda\lambda} - 2\lambda\left(\frac{G_\eta}{\eta} + 4\right)F_\lambda + 6\frac{G_\eta}{\eta}F \\ &\qquad - \frac{4K}{2-\eta^2} + \chi\lambda^2\left[-\lambda T_\lambda + T - \frac{(1-\eta^2)T_\eta}{2\eta}\right] = 0\,, \end{aligned} \tag{4.27}$$

$$-F - \frac{G_\eta}{4\eta^3} + \frac{G_{\eta\eta}}{4\eta^2} + \frac{(2\lambda G_\lambda + \lambda^2 G_{\lambda\lambda})}{(2-\eta^2)\eta^2} = 0, \tag{4.28}$$

$$\begin{aligned} &-\frac{1}{2\eta}G_\eta\left(\lambda T_\lambda - T\right) + \frac{1}{2\eta}T_\eta\left(G + \lambda G_\lambda\right) \\ &\qquad + \frac{\kappa}{\nu}\left[\lambda^2 T_{\lambda\lambda} + (2-3\eta^2)\frac{T_\eta}{4\eta} + \frac{(2-\eta^2)}{4}T_{\eta\eta}\right] = 0, \end{aligned} \tag{4.29}$$

respectively.

The changes in variable imply

$$\frac{\partial T}{\partial \theta} = -\sin\theta\frac{\partial T}{\partial \mu} = \frac{\sin\theta}{2\eta}\frac{\partial T}{\partial \eta} = \frac{\sin\theta}{2(1-\cos\theta)^{1/2}}\frac{\partial T}{\partial \eta}\,,$$

but

$$\frac{\sin\theta}{2(1-\cos\theta)^{1/2}} = \frac{(1-\cos^2\theta)^{1/2}}{2(1-\cos\theta)^{1/2}} = \frac{(1+\cos\theta)^{1/2}}{2} = \frac{\cos\theta/2}{2^{1/2}} ,$$

and hence the boundary conditions (4.21) and (4.22) are equivalent to

$$\left(\frac{\partial T}{\partial \eta}\right)_{\eta=1} = 0, \tag{4.30}$$

$$\left(\frac{\partial T}{\partial \eta}\right)_{\eta=0} = 0. \tag{4.31}$$

The final set of boundary conditions to be used are, therefore,

$$G(0,\lambda) = 0, \qquad \mathbf{v} \text{ finite on axis,} \tag{4.32}$$

$$G(\eta,1) = 0, \qquad \mathbf{v} \text{ zero on } \lambda = 1, \tag{4.33}$$

$$G(1,\lambda) = 0, \qquad \mathbf{v} \text{ tangential on top surface,} \tag{4.34}$$

$$G(\eta,0) = g_0(\mu), \qquad \text{limit as } \lambda \to 0, \tag{4.35}$$

$$F(1,\lambda) = \frac{T_m\, a}{\rho \nu^2}\frac{\partial \gamma}{\partial T}\,[\lambda T_\lambda(1,\lambda) - T(1,\lambda)], \qquad \text{stress on the top surface,} \tag{4.36}$$

$$F(\eta,0) = g_0''(\mu), \qquad \text{limit as } \lambda \to 0, \tag{4.37}$$

$$F_\eta(0,\lambda) = 0, \quad \text{keep derivatives finite on the axis,} \tag{4.38}$$

$$F(\eta,1) = \frac{g_{\lambda\lambda}}{1-\mu^2} = \frac{G_{\lambda\lambda}}{\eta^2(2-\eta^2)}, \qquad \text{(4.28) evaluated on } \lambda = 1, \tag{4.39}$$

$$F(0,1) = \frac{1}{4}\, G_{\eta\eta\lambda\lambda}\, , \qquad \text{(4.28) evaluated on } \lambda = 1,\ \eta = 0, \tag{4.40}$$

$$T_\eta(0,\lambda) = 0, \qquad \text{no heat flux across top surface,} \tag{4.41}$$

$$T_\eta(1,\lambda) = 0, \qquad \text{no heat flux across axis,} \tag{4.42}$$

$$T(\eta,1) = T_m, \qquad \text{temperature at melting temperature on hemisphere,} \tag{4.43}$$

$$T(\eta,0) = t_0(\mu), \qquad \text{limit as } \lambda \to 0. \tag{4.44}$$

## 4.4 Converting to finite differences

Traditional methods of writing first order advective derivatives in finite difference form can lead to problems when fluid velocities are not small. Results obtained can look rather diffuse when using one-sided differences, or may not converge when using central differences[ 59 ]. The numerical method used here is to write the first derivatives as finite differences using the Quadratic Upstream Interpolation (QUI) method introduced by Leonard [ 59 ], due to its greater accuracy and stability compared to the more traditional methods. The QUI method is explained in greater detail on the next three pages.

### 4.4.1 Quadratic Upstream Interpolation (QUI)

Traditionally first derivatives are approximated using either central differences, or one-sided first order differences. Leonard [ 59 ] showed that both of these methods have problems when the convection term is important. The reasons for these problems are discussed below, and the justification of the accuracy of the QUI scheme is presented. Attention is confined to a one dimensional system, for simplicity, because converting the QUI method to two dimensions is trivial to undertake but makes the notation more complicated.

Consider the model convective-diffusion equation

$$\frac{\partial P}{\partial t} = -\mathrm{u}\frac{\partial P}{\partial x} + \nu\frac{\partial^2 P}{\partial x^2} + S\,, \tag{4.45}$$

where P is some variable quantity, t denotes time, x is a spatial coordinate, u is the fluid velocity and $\nu$ is the diffusion coefficient. In this equation the first term on the right-hand side represents the convection of P with the fluid, the second represents the diffusion of P through the fluid and S represents any other terms not explicitly specified.

Standard first order, one-sided differences for the first derivative of the variable P with respect to x, at a point $x_i$, are

$$\left(\frac{\partial P}{\partial x}\right)_i \approx \frac{P_i - P_{i-1}}{\Delta x},$$

and

$$\left(\frac{\partial P}{\partial x}\right)_i \approx \frac{P_{i+1} - P_i}{\Delta x}.$$

Expanding P in a Taylor series about the point $x_i$ gives

$$P_{i+1} = P_i + \Delta x\left(\frac{\partial P}{\partial x}\right)_i + \frac{(\Delta x)^2}{2}\left(\frac{\partial^2 P}{\partial x^2}\right)_i + \frac{(\Delta x)^3}{6}\left(\frac{\partial^3 P}{\partial x^3}\right)_i + O\left((\Delta x)^4\right), \tag{4.46}$$

and

$$P_{i-1} = P_i - \Delta x\left(\frac{\partial P}{\partial x}\right)_i + \frac{(\Delta x)^2}{2}\left(\frac{\partial^2 P}{\partial x^2}\right)_i - \frac{(\Delta x)^3}{6}\left(\frac{\partial^3 P}{\partial x^3}\right)_i + O\left((\Delta x)^4\right). \tag{4.47}$$

Hence the convection term in (4.45) can be written, using one-sided differences, as

$$-\mathrm{u}\left[\frac{P_i - P_{i-1}}{\Delta x}\right] = -\mathrm{u}\left[\left(\frac{\partial P}{\partial x}\right)_i - \frac{\Delta x}{2}\left(\frac{\partial^2 P}{\partial x^2}\right)_i + O\left((\Delta x)^2\right)\right], \tag{4.48}$$

or

$$-\mathrm{u}\left[\frac{P_{i+1} - P_i}{\Delta x}\right] = -\mathrm{u}\left[\left(\frac{\partial P}{\partial x}\right)_i + \frac{\Delta x}{2}\left(\frac{\partial^2 P}{\partial x^2}\right)_i + O\left((\Delta x)^2\right)\right]. \tag{4.49}$$

Looking at the leading order discretisation terms in (4.48) and (4.49), and comparing with equation (4.45), it is seen that they are equivalent to a physical diffusion term with an effective diffusion coefficient of $\pm\frac{\mathrm{u}\Delta x}{2}$ respectively. So, if (4.48) is chosen when $u>0$, and (4.49) when $u<0$, the discretisation error terms interfere with, and may completely swamp, the diffusion terms present in the system, when u is large.

In Leonard's QUI method the term $-u\frac{\partial P}{\partial x}$ is replaced by one of the following difference expressions:

when $u>0$

$$-\mathrm{u}\left[\frac{P_{i+1}-P_{i-1}}{2\Delta x} - \frac{(P_{i+1} - 3P_i + 3P_{i-1} - P_{i-2})}{6\Delta x}\right]$$
$$= -\mathrm{u}\left[\frac{(2P_{i+1} + 3P_i - 6P_{i-1} + P_{i-2})}{6\Delta x}\right], \tag{4.50}$$

when u<0

$$-\mathrm{u}\left[\frac{P_{i+1}-P_{i-1}}{2\Delta x}-\frac{(P_{i+2}-3P_{i+1}+3P_i-P_{i-1})}{6\Delta x}\right]$$
$$=-\mathrm{u}\left[\frac{(-P_{i+2}+6P_{i+1}-3P_i-2P_{i-1})}{6\Delta x}\right]. \qquad (4.51)$$

With the aid of the Taylor series (4.46) and (4.47), and the corresponding ones for $P_{i+2}$ and $P_{i-2}$ which can be written

$$P_{i+2}=P_i+2\Delta x\left(\frac{\partial P}{\partial x}\right)_i+2(\Delta x)^2\left(\frac{\partial^2 P}{\partial x^2}\right)_i+\frac{4(\Delta x)^3}{3}\left(\frac{\partial^3 P}{\partial x^3}\right)_i+O\left((\Delta x)^4\right), \qquad (4.52)$$

and

$$P_{i-2}=P_i-2\Delta x\left(\frac{\partial P}{\partial x}\right)_i+2(\Delta x)^2\left(\frac{\partial^2 P}{\partial x^2}\right)_i-\frac{4(\Delta x)^3}{3}\left(\frac{\partial^3 P}{\partial x^3}\right)_i+O\left((\Delta x)^4\right), \qquad (4.53)$$

we see expression (4.50) is equivalent to

$$=-\mathrm{u}\left[\left(\frac{\partial P}{\partial x}\right)_i+\frac{(\Delta x)^3}{12}\left(\frac{\partial^4 P}{\partial x^4}\right)_i+O\left((\Delta x)^4\right)\right], \qquad (4.54)$$

and expression (4.51) is equivalent to

$$=-\mathrm{u}\left[\left(\frac{\partial P}{\partial x}\right)_i-\frac{(\Delta x)^3}{12}\left(\frac{\partial^4 P}{\partial x^4}\right)_i+O\left((\Delta x)^4\right)\right]. \qquad (4.55)$$

It is obvious, therefore, that the QUI form for the finite difference representations of the convection term do not have the same problem as that obtained with the one-sided differences.

Central differences can also be used for first derivatives. The basic expression has the form

$$\left(\frac{\partial P}{\partial x}\right)_i=\frac{P_{i+1}-P_{i-1}}{2\Delta x}.$$

Considering the Taylor series (4.46) and (4.47), it can be shown that expressing the convection term using central differences leads to

$$-\mathrm{u}\left[\frac{P_{i+1}-P_{i-1}}{2\Delta x}\right]=-\mathrm{u}\left[\left(\frac{\partial P}{\partial x}\right)_i+\frac{(\Delta x)^2}{6}\left(\frac{\partial^3 P}{\partial x^3}\right)_i+O\left((\Delta x)^3\right)\right].$$

It is obvious that the central difference representation of the convection term, like the QUI method, does not produce the additional diffusion term. However it does have a different disadvantage. Its use when convection is strong can result in the numerical method being divergent.

On writing a numerical scheme in matrix form $\Phi^{n+1} = A\ \Phi^{n}$, where $\Phi^{\mathrm{n}}$ is a vector of the discretised unknown variable at iteration n, stability of the scheme requires the amplification matrix $A$ to have a spectral radius less than one (i.e. all the eigenvalues of $A$ must have absolute value less than unity). It is not always easy to show whether this is satisfied for particular numerical schemes. It is well known that the use of central difference representation for first derivatives can lead to instability. The work of Leonard and others suggests that a more stable method for creating a finite difference approximation to the governing equations is to use standard central differences for the second derivatives, but to use the third order QUI method for the first derivatives, and it is this approach that has been used in the following sections to solve the differential equations.

## 4.4.2 Writing the governing equations in finite difference form.

Equations (4.27) and (4.29) both include products of first derivatives; one term in each product is the derivative of the variable for which the equation is being solved, whereas the other is a derivative of one of the other dependent variables. Originally an attempt was made to use the QUI scheme for both derivatives but, even after a considerable amount of work, no convergent algorithm was produced. The approach adopted in this section is to approximate the first derivatives of a variable using the QUI method in the equation which is being used to update its value, but by central differences in the other equations.

The mesh points used are equally spaced, and the same number of points are used in both coordinate directions. The points are labelled for $\lambda$=0 to 1 as i=0 to N, and for $\eta$=0 to 1 as j=0 to N. The value of $\lambda$ at a particular grid point i is given by $\lambda_i = i\Delta\lambda$, and similarly $\eta_j = j\Delta\eta$. In the finite difference equations, an omitted suffix has the value i or j as appropriate.

Let us return to equation (4.27),

$$(2-\eta^2)F_{\eta\eta} + \left(2\lambda G_\lambda + 2G + 6 - 7\eta^2\right)\frac{F_\eta}{\eta} + 4\lambda^2 F_{\lambda\lambda} - 2\lambda\left(\frac{G_\eta}{\eta} + 4\right)F_\lambda + 6\frac{G_\eta}{\eta}F$$
$$-\frac{4K}{2-\eta^2} + \chi\lambda^2\left[-\lambda T_\lambda + T - \frac{(1-\eta^2)T_\eta}{2\eta}\right] = 0\,,$$

which is used to update the variable F.

Firstly, looking at the terms which will have only one form for the finite difference representation, and writing down only the subscript that changes in each case we obtain

$$(2-\eta^2)F_{\eta\eta}: \quad (2-\eta_j^2)\frac{(F_{j+1} - 2F_j + F_{j-1})}{(\Delta\eta)^2}, \tag{4.56}$$

$$4\lambda^2 F_{\lambda\lambda}: \quad 4i^2(F_{i+1} - 2F_i + F_{i-1})\,, \tag{4.57}$$

$$6\frac{G_\eta}{\eta}F: \quad \frac{3}{\eta_j\Delta\eta}(G_{j+1} - G_{j-1})\,F_{i,j}\,, \tag{4.58}$$

$$\chi\lambda^2(-\lambda T_\lambda + T - \frac{(1-\eta^2)T_\eta}{2\eta}):$$

$$\chi\lambda_i^2\left[\frac{-i}{2}(T_{i+1} - T_{i-1}) + T_i - (1-\eta_j^2)\frac{1}{4\eta_j\Delta\eta}(T_{j+1} - T_{j-1})\right]. \qquad (4.59)$$

Next consider the terms containing the first derivatives in F. In each case the first derivative in G is expanded using central differences.

$$-2\lambda\left(\frac{G_\eta}{\eta} + 4\right)F_\lambda:$$

when $\left[\frac{1}{2\Delta\eta\eta_i}(G_{j+1} - G_{j-1}) + 4\right] > 0$ use

$$\frac{-i}{3}\left[\frac{1}{2\Delta\eta\eta_i}(G_{j+1} - G_{j-1}) + 4\right](2F_{i+1} + 3F_i - 6F_{i-1} + F_{i-2}), \qquad (4.60)$$

and when $\left[\frac{1}{2\Delta\eta\eta_i}(G_{j+1} - G_{j-1}) + 4\right] < 0$ use

$$-\frac{i}{3}\left[\frac{1}{2\Delta\eta\eta_i}(G_{j+1} - G_{j-1}) + 4\right](-F_{i+2} + 6F_{i+1} - 3F_i - 2F_{i-1}), \qquad (4.61)$$

$$(2\lambda G_\lambda + 2G + 6 - 7\eta^2)\frac{F_\eta}{\eta}:$$

when $[i\,(G_{i+1} - G_{i-1}) + 2G_i + 6 - 7\eta_j^2] > 0$ use

$$[i\,(G_{i+1} - G_{i-1}) + 2G_i + 6 - 7\eta_j^2]\frac{1}{\eta_j 6\Delta\eta}(-F_{j+2} + 6F_{j+1} - 3F_j - 2F_{j-1}), \qquad (4.62)$$

and when $[i\,(G_{i+1} - G_{i-1}) + 2G_i + 6 - 7\eta_j^2] < 0$ use

$$[i\,(G_{i+1} - G_{i-1}) + 2G_i + 6 - 7\eta_j^2]\frac{1}{\eta_j 6\Delta\eta}(2F_{j+1} + 3F_j - 6F_{j-1} + F_{j-2}). \qquad (4.63)$$

Next consider the equation solved for the temperature, T, equation (4.29):

$$-\frac{1}{2\eta}G_\eta(\lambda T_\lambda - T) + \frac{1}{2\eta}T_\eta(G + \lambda G_\lambda) + \frac{\kappa}{\nu}\left[\lambda^2 T_{\lambda\lambda} + (2 - 3\eta^2)\frac{T_\eta}{4\eta} + \frac{(2-\eta^2)}{4}T_{\eta\eta}\right] = 0.$$

Converting this equation to finite differences term by term yields

$$-\frac{1}{2\eta}G_\eta(\lambda T_\lambda - T) \ :$$

when $\frac{1}{2\eta_j\Delta\eta}(G_{j+1} - G_{j-1}) > 0$ use

$$-\frac{1}{4\eta_j\Delta\eta}(G_{j+1} - G_{j-1})\left[\frac{i}{6}(2T_{i+1} + 3T_i - 6T_{i-1} + T_{i-2}) - T_i\right], \tag{4.64}$$

and when $\frac{1}{2\eta_j\Delta\eta}(G_{j+1} - G_{j-1}) < 0$ use

$$-\frac{1}{4\eta_j\Delta\eta}(G_{j+1} - G_{j-1})\left[\frac{i}{6}(-T_{i+2} + 6T_{i+1} - 3T_i - 2T_{i-1}) - T_i\right], \tag{4.65}$$

$$\frac{1}{2}(G + \lambda G_\lambda)T_\eta \ :$$

when $\left[G_i + \frac{i}{2}(G_{i+1} - G_{i-1})\right] > 0$ use

$$\frac{1}{12\eta_j\Delta\eta}(-T_{j+2} + 6T_{j+1} - 3T_j - 2T_{j-1})\left[G_i + \frac{i}{2}(G_{i+1} - G_{i-1})\right], \tag{4.66}$$

and when $\left[G_i + \frac{i}{2}(G_{i+1} - G_{i-1})\right] < 0$ use

$$\frac{1}{12\eta_j\Delta\eta}(2T_{j+1} + 3T_j - 6T_{j-1} + T_{j-2})\left[G_i + \frac{i}{2}(G_{i+1} - G_{i-1})\right], \tag{4.67}$$

$$\frac{\kappa}{\nu}\left[\lambda^2 T_{\lambda\lambda} + (2 - 3\eta^2)\frac{T_\eta}{4\eta} + \frac{(2-\eta^2)}{4}T_{\eta\eta}\right] :$$

when $\eta > (2/3)^{1/2}$ use

$$\frac{\kappa}{\nu}\left[i^2(T_{i+1} - 2T_i + T_{i-1}) + \frac{(2-\eta_j^2)}{4(\Delta\eta)^2}(T_{j+1} - 2T_j + T_{j-1}) + \frac{(2-3\eta_j^2)}{24\eta_j\Delta\eta}(2T_{j+1} + 3T_j - 6T_{j-1} + T_{j-2})\right], \tag{4.68}$$

and when $\eta < (2/3)^{1/2}$ use

$$\frac{\kappa}{\nu}\left[ i^2\,(T_{i+1} - 2T_i + T_{i-1}) + \frac{(2-\eta_j^2)}{4(\Delta\eta)^2}\,(T_{j+1} - 2T_j + T_{j-1}) \right.$$
$$\left. + \frac{(2-3\eta_j^2)}{24\eta_j\Delta\eta}\,(-T_{j+2} + 6T_{j+1} - 3T_j - 2T_{j-1}) \right]. \tag{4.69}$$

Finally, consider equation (4.28) which is used to update the variable G. Applying our method to this equation produces only one form for the finite difference representation, which is:

$$-F_{i,j} - \frac{1}{24\eta_j^3\Delta\eta}\,(G_{j-2} - 6G_{j-1} + 3G_j + 2G_{j+1}) + \frac{1}{4\eta_j^2(\Delta\eta)^2}\,(G_{j+1} - 2G_j + G_{j-1}) \tag{4.70}$$
$$+ \frac{1}{(2-\eta_j^2)\eta_j^2}\left[\frac{i}{3}(-2G_{i-1} - 3G_i + 6G_{i+1} - G_{i+2}) + i^2\,(G_{i+1} - 2G_i + G_{i-1})\right] = 0.$$

## 4.4.3 Finite differences near the Boundaries

The finite difference schemes presented above need to be altered when we are within one grid point of the boundaries, since the QUI method uses points up to two away from the current point, and working adjacent to the boundary can therefore require points outside the boundary. To avoid this problem, when an equation is solved at a point where i = 1 or N-1, or j = 1or N-1 the finite difference equations are altered to use one-sided differences, instead of the QUI method, to approximate first derivatives. One-sided differences are used in preference to central differences, since the lesser accuracy is preferable to possible instability of the code. The central difference approximation of second derivatives can be left unchanged. Special attention is needed when it is necessary to solve for the value of a variable actually on one of the boundaries, and these situations will be looked at as required.

Since G is specified on all boundaries equation (4.28), which determines G, need only be solved at all interior points. Equation (4.70) is used for all points $2 \leq i \leq N-2$ and

$2 \leq j \leq N-2$. For points i=1 or N-1, or j=1 or N-1, the changes mentioned above are made and the finite difference equation used is

$$-F_{i,j} - \frac{1}{4\eta_j^3\Delta\eta}(G_j - G_{j-1}) + \frac{1}{4\eta_j^2(\Delta\eta)^2}(G_{j+1} - 2G_j + G_{j-1})$$
$$+ \frac{1}{(2-\eta_j^2)\eta_j^2}[2\, i(G_{i+1} - G_i) + i^2\,(G_{i+1} - 2G_i + G_{i-1})] = 0\,. \tag{4.71}$$

Turning to the temperature, boundary conditions (4.23), (4.24), (4.31) and (4.30) state that T is specified for i=0 and N and $T_\eta$ is specified for j=0 and N. This means that a solution for T needs to be found for all values of $\eta$, ie. j=0,...N, and for i = 1,...N-1.

First consider the cases i=1, i=N-1, j=1, or j=N-1 ie. all points which are one in from the boundary. In this case the finite difference approximations for the second derivatives are left unchanged, and first derivatives are approximated by first order one-sided differences,

$-\frac{G_\eta}{2\eta}(\lambda T_\lambda - T)$ :

when $\frac{(G_{j+1} - G_{j-1})}{2\Delta\eta} > 0$ use

$$-\frac{(G_{j+1} - G_{j-1})}{4\eta_j\Delta\eta}\left(i\,(T_i - T_{i-1}) - T_i\right), \tag{4.72}$$

and when $\frac{(G_{j+1} - G_{j-1})}{2\Delta\eta} < 0$ use

$$-\frac{(G_{j+1} - G_{j-1})}{4\eta_j\Delta\eta}\left(i\,(T_{i+1} - T_i) - T_i\right) \tag{4.73}$$

$+ (G + \lambda G_\lambda)\frac{T_\eta}{2\eta}$ :

when $\left(G_i + \frac{i}{2}(G_{i+1} - G_{i-1})\right) > 0$ use

$$\left(G_i + \frac{i}{2}(G_{i+1} - G_{i-1})\right)\frac{(T_{j+1} - T_j)}{2\eta_j\Delta\eta}\,, \tag{4.74}$$

and when $\left(G_i + \frac{i}{2}(G_{i+1} - G_{i-1})\right) < 0$ use

$$\left(G_i + \frac{i}{2}(G_{i+1} - G_{i-1})\right)\frac{(T_j - T_{j-1})}{2\eta_j\Delta\eta} . \tag{4.75}$$

In the square-bracketed term in (4.29) the second derivatives are replaced with central differences as before, but the finite difference approximation for $\frac{\kappa}{\nu}(2 - 3\eta^2)\,\frac{T_\eta}{4\eta}$ is changed:

when $\eta < (2/3)^{1/2}$ use

$$\frac{\kappa}{\nu}(2 - 3\eta_j^2)\frac{(T_{j+1}-T_j)}{4\eta_j\Delta\eta} , \tag{4.76}$$

and when $\eta > (2/3)^{1/2}$ use

$$\frac{\kappa}{\nu}(2 - 3\eta_j^2)\frac{(T_j-T_{j-1})}{4\eta_j\Delta\eta} . \tag{4.77}$$

On the top surface $\eta=1$ (j = N), G=0 and $T_\eta=0$, hence the temperature equation (4.29) reduces to

$$\frac{\kappa}{\nu}\left(\lambda^2 T_{\lambda\lambda} + \frac{T_{\eta\eta}}{4}\right) - \frac{G_\eta}{2}(\lambda T_\lambda - T) = 0 . \tag{4.78}$$

Using central differences for the second derivative in $\eta$ would require the introduction of points above the surface. However $T_\eta = 0$ on the top surface, and central differencing of this condition implies that $T_{N+1} = T_{N-1}$. Hence, wherever $T_{N+1}$ is required in a finite difference approximation, $T_{N-1}$ can be substituted. First derivatives of G with respect to $\eta$ are approximated as one-sided differences using the point on the boundary and the one inside. Since T is specified on both j=0 and N the equation is not solved at the end points, and hence the first and second derivative with respect to $\lambda$ can still be approximated by one-sided differences and standard central differences, respectively.

With these assumptions the first term of equation (4.78) is represented in finite difference form by

$$\frac{\kappa}{\nu}\left(\lambda_i^2\,\frac{(T_{i+1}-2T_i+T_{i-1})}{(\Delta\lambda)^2}+\frac{(T_{N+1}-2T_N+T_{N-1})}{4(\Delta\eta)^2}\right),$$

which simplifies to

$$\frac{\kappa}{\nu}\left(i^2\,(T_{i+1}-2T_i+T_{i-1})+\frac{(T_{N-1}-T_N)}{2(\Delta\eta)^2}\right). \qquad (4.79)$$

On looking at the second term of (4.78), $G_\eta$ is approximated by a one-sided finite difference using only the point on the boundary and the one inside. However, G=0 on $\eta$=1, so the form for the finite difference approximation for $T_\lambda$ is determined by the sign of $G_{N-1}$ :

when $G_{N-1} < 0$ use

$$-\frac{(-G_{N-1})}{2\Delta\eta}\,(i\,(T_i-T_{i-1})-T_{i,j})\ , \qquad (4.80)$$

and when $G_{N-1} > 0$ use

$$-\frac{(-G_{N-1})}{2\Delta\eta}\,(i\,(T_{i+1}-T_i)-T_{i,j})\ . \qquad (4.81)$$

Finally for the temperature equation we must consider the case $\eta$=0, at which the relevant boundary conditions are $T_\eta$=0, G=0, $G_\eta$=0 and $G_\lambda$=0. Using these conditions and L'Hopital's rule, equation (4.29) reduces to

$$-\frac{1}{2}\,G_{\eta\eta}(\lambda T_\lambda - T\,)+\frac{\kappa}{\nu}\left[\lambda^2 T_{\lambda\lambda}+\frac{T_{\eta\eta}}{2}+\frac{T_{\eta\eta}}{2}\right]=0. \qquad (4.82)$$

Since the flow is assumed to be axisymmetric, the flow is identical on both sides of the axis $\eta = 0$. This implies that the points on one side have the same values as points on the other side, ie $G_{-1} = G_1$ and $T_{-1} = T_1$. Hence equation (4.82) can be written in finite difference form

when $(G_1 - G_0) > 0$ as

$$-\frac{(G_1-G_0)}{(\Delta\eta)^2}\,(i\,(T_i-T_{i-1})-T_i)+\frac{\kappa}{\nu}\left[i^2(T_{i+1}-2T_i+T_{i-1})+\frac{2(T_1-T_0)}{(\Delta\eta)^2}\right]=0, \quad (4.83)$$

and when $(G_1 - G_0) < 0$ as

$$-\frac{(G_1 - G_0)}{(\Delta\eta)^2}\,(i\,(T_{i+1} - T_i) - T_i) + \frac{\kappa}{\nu}\left[i^2(T_{i+1} - 2T_i + T_{i-1}) + \frac{2(T_1 - T_0)}{(\Delta\eta)^2}\right] = 0. \quad (4.84)$$

Finally consider equation (4.27), which is used to update F. The boundary conditions (4.36) to (4.39) specify F on all the boundaries except $\eta=0$. The finite difference equations (4.56) to (4.63) are solved in the interior of the region, i = 1,...N-1 and j = 1,...N-1. When i=1, i=N-1, j=1 or j=N-1 ie. one point in from the boundaries, again the method needs to be changed. As before the second derivatives are approximated by central differences, but the first derivatives are changed to one-sided differences. The terms that change are as follows

$(2\lambda G_\lambda + 2G + 6 - 7\eta^2)\dfrac{F_\eta}{\eta}$ :

when $(i\,(G_{i+1} - G_{i-1}) + 2G_i + 6 - 7\eta_j^2) > 0$ use

$$(i\,(G_{i+1} - G_{i-1}) + 2G_i + 6 - 7\eta_j^2)\frac{(F_{j+1} - F_j)}{\eta_j\Delta\eta}\,, \quad (4.85)$$

and when $(i\,(G_{i+1} - G_{i-1}) + 2G_i + 6 - 7\eta_j^2) < 0$ use

$$(i\,(G_{i+1} - G_{i-1}) + 2G_i + 6 - 7\eta_j^2)\frac{(F_j - F_{j-1})}{\eta_j\Delta\eta}\,. \quad (4.86)$$

$-2\lambda\left(\dfrac{G_\eta}{\eta} + 4\right)F_\lambda$:

when $\left(\dfrac{(G_{j+1} - G_{j-1})}{2\eta\Delta\eta} + 4\right) > 0$ use

$$-2i\left(\frac{(G_{j+1} - G_{j-1})}{2\eta_j\Delta\eta} + 4\right)(F_i - F_{i-1})\,, \quad (4.87)$$

and when $\left(\dfrac{(G_{j+1} - G_{j-1})}{2\eta_j\Delta\eta} + 4\right) < 0$ use

$$-2i\left(\frac{(G_{j+1} - G_{j-1})}{2\eta_j\Delta\eta} + 4\right)(F_{i+1} - F_i)\,. \quad (4.88)$$

The equation (4.27) must also be solved on $\eta=0$, where boundary conditions (4.32), (4.31), (4.38) and (4.14) state that $G=0$, $G_\eta=0$, $G_\lambda=0$, $T_\eta=0$ and $F_\eta=0$. Use is also made of L'Hopital's rule in evaluating terms of the form $\frac{G_\eta}{\eta}$.

With the above observations, on $\eta=0$ equation (4.27) simplifies to

$$\begin{aligned}&8F_{\eta\eta}+4\lambda^2F_{\lambda\lambda}-2\lambda(G_{\eta\eta}+4)F_\lambda+6G_{\eta\eta}F\\&+\chi\lambda^2(-\lambda T_\lambda+T-\tfrac{1}{2}T_{\eta\eta})-2K=0\,.\end{aligned}\tag{4.89}$$

Making use of axisymmetry, and the boundary conditions (4.38), (4.31) and (4.14), allows us to state that $G_{-1}=G_1$, $F_{-1}=F_1$ and $T_{-1}=T_1$. The finite difference form for each term of equation (4.89) can now be stated:

when $\left(\frac{(G_1-G_0)}{(\Delta\eta)^2}+2\right)>0$ use

$$\begin{aligned}&16\frac{(F_1-F_0)}{(\Delta\eta)^2}+4i^2\,(F_{i+1}-2F_i+F_{i-1})\\&-4i\left(\frac{(G_1-G_0)}{(\Delta\eta)^2}+2\right)(F_i-F_{i-1})+12\frac{(G_1-G_0)}{(\Delta\eta)^2}F_{i,j}\\&-2K+\chi\lambda_i^2\left(-i\,\frac{(T_{i+1}-T_{i-1})}{2}+T_{i,j}-\frac{(T_1-T_0)}{(\Delta\eta)^2}\right)=0\,,\end{aligned}\tag{4.90}$$

and when $\left(\frac{(G_1-G_0)}{(\Delta\eta)^2}+2\right)<0$ use

$$\begin{aligned}&16\frac{(F_1-F_0)}{(\Delta\eta)^2}+4i^2\,(F_{i+1}-2F_i+F_{i-1})\\&-4i\left(\frac{(G_1-G_0)}{(\Delta\eta)^2}+2\right)(F_{i+1}-F_i)+12\frac{(G_1-G_0)}{(\Delta\eta)^2}F_{i,j}\\&-2K+\chi\lambda_i^2\left(-i\,\frac{(T_{i+1}-T_{i-1})}{2}+T_{i,j}-\frac{(T_1-T_0)}{(\Delta\eta)^2}\right)=0\,.\end{aligned}\tag{4.91}$$

F is defined by derivative boundary conditions (4.36) and (4.39) on the boundaries of $\eta=1$ and $\lambda=1$. These are converted into finite differences as follows. On $\eta=1$ the boundary condition is

$$F(1,\lambda) = \frac{T_m\, a}{\rho v^2}\,\frac{\partial \gamma}{\partial T}\,[\lambda T_\lambda(1,\lambda) - T\,(1,\lambda)],$$

which can be represented in finite difference form as

$$F_{i,N} = \frac{T_m\, a}{\rho v^2}\,\frac{\partial \gamma}{\partial T}\left[\frac{i\,(T_{i+1} - T_{i-1})}{2} - T_{i,N}\right]. \tag{4.92}$$

This is used to solve for F along the boundary except at the end points. On $\lambda=0$ the condition $F(\eta,0) = g_0''$ is used. On $\lambda=1$ the first derivative of T is approximated by a one-sided difference so that a point outside the boundary is not needed, giving

$$F_{N,N} = \frac{T_m\, a}{\rho v^2}\,\frac{\partial \gamma}{\partial T}\left[N\,(T_N - T_{N-1}) - T_{N,N}\right]. \tag{4.93}$$

On the remainder of the boundary $\lambda=1$ the following condition holds:

$$F(\eta,1) = \frac{G_{\lambda\lambda}}{\eta^2(2-\eta^2)}. \tag{4.94}$$

There have been several different methods proposed to deal with this type of boundary condition, the one used here was introduced by Woods [ 112 ]:

$$F_N = \frac{3G_{N-1}}{(\Delta\lambda)^2\eta^2(2-\eta^2)} - \frac{F_{N-1}}{2} + O(\Delta\lambda^2) \tag{4.95}$$

Other researchers ([ 77 ], [ 108 ]) have found this to be an accurate method which does not produce as many problems with convergence as some more obvious approximations. On the axis $\eta=0$ the boundary condition for F is

$$F(0,1) = \frac{1}{4}\,G_{\eta\eta\lambda\lambda}. \tag{4.96}$$

From the Taylor series (4.47) and (4.53) it is possible to construct an approximation for the second derivative that does not require any points outside the weld pool:

$$\frac{\partial^2 G}{\partial \lambda^2} = \left(\frac{G_{i,N} - 2G_{i,N-1} + G_{i,N-2}}{(\Delta\lambda)^2}\right) + O(\Delta\lambda)\,. \tag{4.97}$$

Equation (4.96) is now converted to finite differences by applying (4.97) first for derivatives with respect to $\lambda$ and then for derivatives with respect to $\eta$. Since G is zero on the boundary, the boundary points in the expansion are eliminated leaving the following as the expression for $G_{\eta\eta\lambda\lambda}$

$$F_{N,0} = \frac{1}{4(\Delta\eta)^2(\Delta\lambda)^2}\left(4G_{N-1,N-1} - 2G_{N-2,N-1} - 2G_{N-1,N-2} + G_{N-2,N-2}\right) \qquad (4.98)$$

This approximation has low accuracy. However, it is used for only one corner point and hence should not significantly affect the accuracy of the final results.

# 4.5 Results and discussion

The finite difference equations obtained in the previous section ( (4.56)-(4.63), (4.64)-(4.69), (4.70), (4.71), (4.72)-(4.77), (4.85)-(4.88), (4.79)-(4.81), (4.83)-(4.84), (4.90), (4.91), (4.92) and (4.93) ), were solved using Successive Under Relaxation (SUR). An initial attempt was made to use the more sophisticated method of Stone's Strongly Implicit Procedure (SIP) using a NAG routine. However, the routine was divergent for all parameter values tried, and so the simpler method of SUR was used instead.

The method of solution is as follows:

1) The similarity solution of Chapter 2 is calculated, and used to set the values for F,G,T on $\lambda=0$.

2) F and G are set to zero everywhere else, and T to a linear profile from the origin to the outer hemisphere.

3) An SUR sweep is made to calculate new values for F,G and T in turn, and the maximum percentage change made at any grid point is recorded.

4) The SUR sweeps are repeated until the maximum percentage change in any of the variables is less than a specified tolerance. If convergence could not be obtained, the value of the relaxation parameter (origionally set to 0.7) is reduced and, as long as it is still above 0.1, this process is repeated from step 2.

## 4.5.1 Accuracy of the results

To check the accuracy of the results obtained using the computer program several numerical comparisons were made. Firstly, for several parameter values, solutions were computed using 21x21,41x41,61x61 and 81x81 grids. In each case the tolerance for convergence was set to be 0.1%. Figure 4.2 shows the maximum percentage change in $G(\lambda,\eta)$ from one grid size to the next defined by $\max_{(i,j)}\left(\frac{|\text{change in } G(i,j)|}{\max_{(i,j)}(|G(i,j)|)}\right)\times 100$ for three parameter values: set 1 is $\frac{\partial\gamma}{\partial T}$=8*$10^{-6}$Nm$^{-1}$K$^{-1}$ and J=0.2A; set 2 is $\frac{\partial\gamma}{\partial T}$=-5*$10^{-6}$Nm$^{-1}$K$^{-1}$ and J=5.0A; set 3 is $\frac{\partial\gamma}{\partial T}$=-$10^{-4}$Nm$^{-1}$K$^{-1}$ and J=1.0A. The changes in T(λ,η) were in all cases too small (<<0.1%) to affect any decision about the grid size needed. It can be seen that for most cases a 61x61 grid provides a reasonably accurate solution.

Solutions were also found for a 61x61 grid using a tolerance of 0.01%. The mean percentage change over the grid was less than 0.1% in all cases, and hence the tolerance was kept at 0.1%.

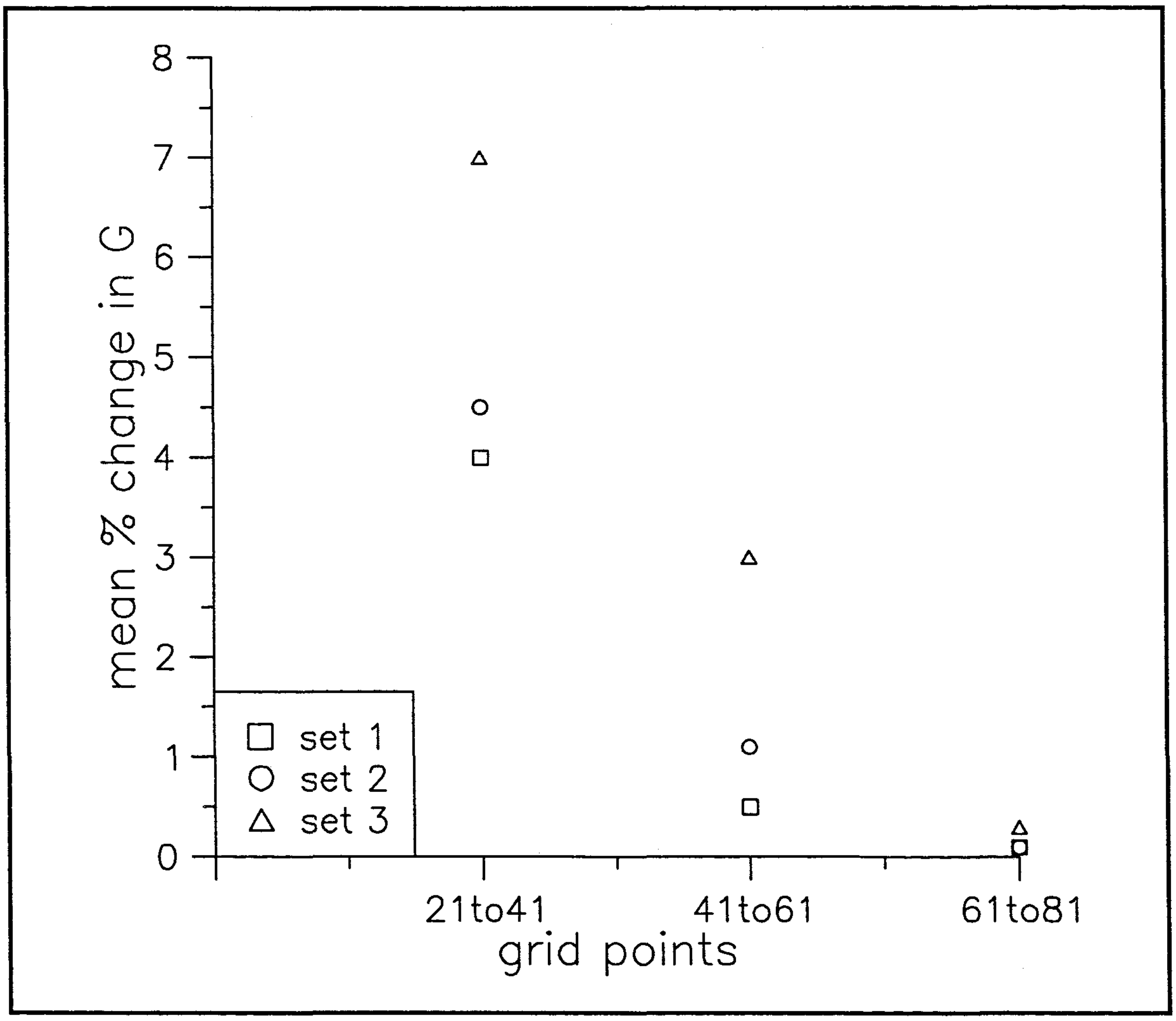

**Figure 4.2 -** percentage change in solutions from increasing the number of grid points

## 4.5.2 The effect of buoyancy

In contrast to the models in Chapters 2 and 3, the buoyancy force was included within this chapter. Under the influence of buoyancy the colder fluid at the outside of the hemisphere will sink and the warmer fluid near the centre will rise, trying to generate an upward and outward circulation in opposition to the inward flow generated by the Lorentz force. It has been estimated that the buoyancy force is only 5-10% of the size of the Lorentz or surface tension forces [ 7 ], but researchers have found significant differences in the flows resulting from their models on including it, especially at low currents [ 20 ], [ 55 ]. The following results illustrate the effect its addition has on solutions obtained with the current model.

The figures 4.3 to 4.6 display plots of the streamlines for the flow in the hemisphere at a fixed current of 1A and a positive $\frac{\partial\gamma}{\partial T}$ of $5*10^{-7}Nm^{-1}K^{-1}$, but with $\beta$, the coefficient of thermal expansion (4.11), varying from 0 to its physical value of $1.25*10^{-4}K^{-1}$. The numbers on the streamlines denote the appropriate values of $\psi/(\nu a)$, and those on the isotherms denote degrees Kelvin above the melting temperature $T_m$.

As would be expected, when there is no buoyancy force present the flow forms a single inward flowing loop, as both the Lorentz and Marangoni forces both push the fluid inwards along the top surface (figure 4.3).

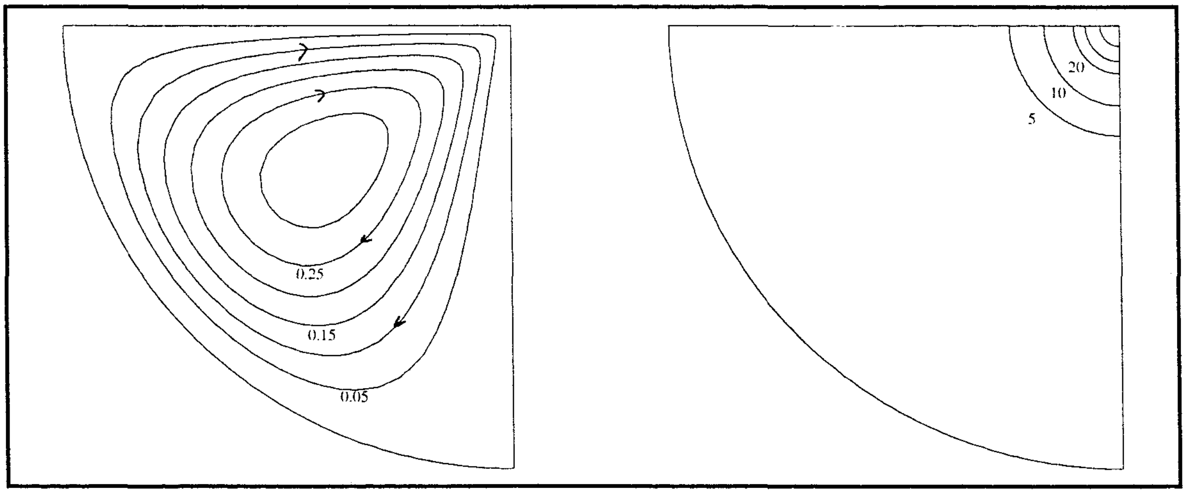

**Figure 4.3** - streamlines and isotherms for J=1A, $\beta=0\ K^{-1}$, $\frac{\partial\gamma}{\partial T}=5*10^{-7}Nm^{-1}K^{-1}$

Adding a buoyancy force with $\beta = 10^{-5}K^{-1}$, figure 4.4, produces a flow that is almost indistinguishable from that with no buoyancy force.

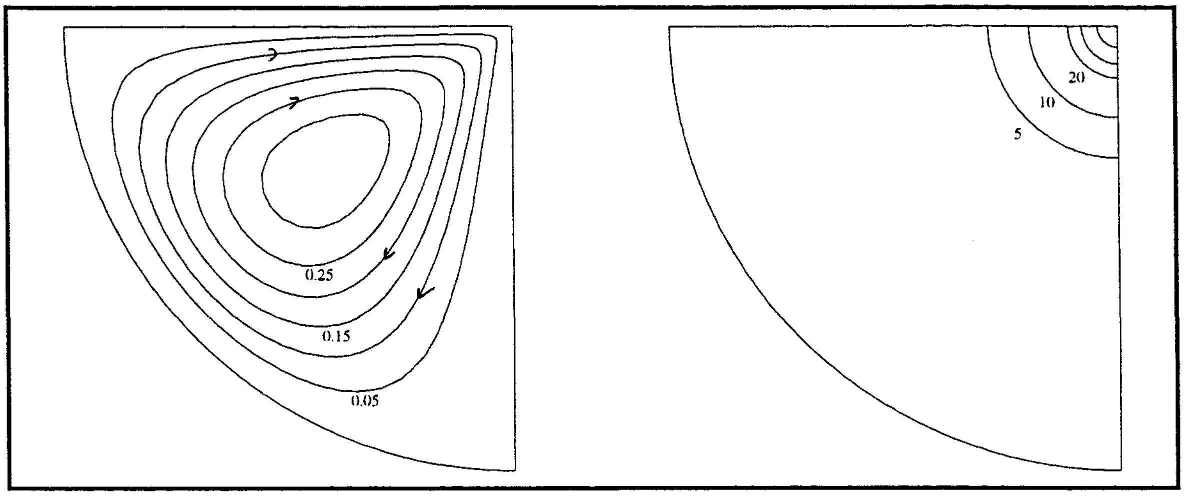

**Figure 4.4** - streamlines and isotherms for J=1A, $\beta=10^{-5}K^{-1}$, $\frac{\partial \gamma}{\partial T}=5*10^{-7}Nm^{-1}K^{-1}$

On increasing $\beta$ to $5*10^{-5}K^{-1}$ the effect of buoyancy can now be seen, with a slow, counter-rotating buoyancy driven loop appearing towards the edge of the hemisphere, figure 4.5.

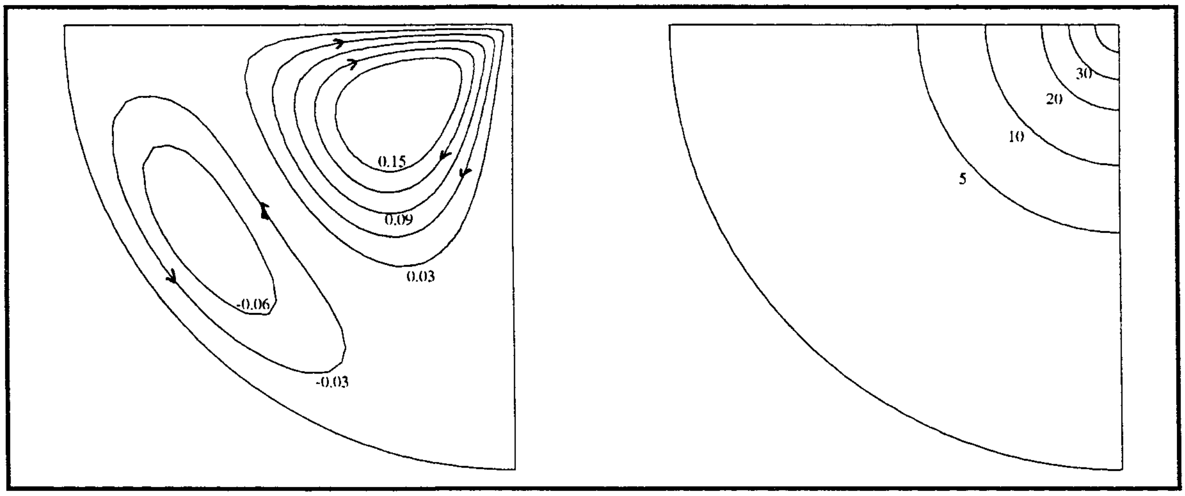

**Figure 4.5** - streamlines and isotherms for J=1A, $\beta=5*10^{-5}K^{-1}$, $\frac{\partial \gamma}{\partial T}=5*10^{-7}Nm^{-1}K^{-1}$

Using the full value for $\beta$ of $1.25*10^{-4}K^{-1}$ it can clearly be seen that the buoyancy force has completely changed the structure of the flow, with two counter-rotating loops being present, figure 4.6. The buoyancy force dominates over most of the hemisphere, with the Lorentz force dominating only near the origin.

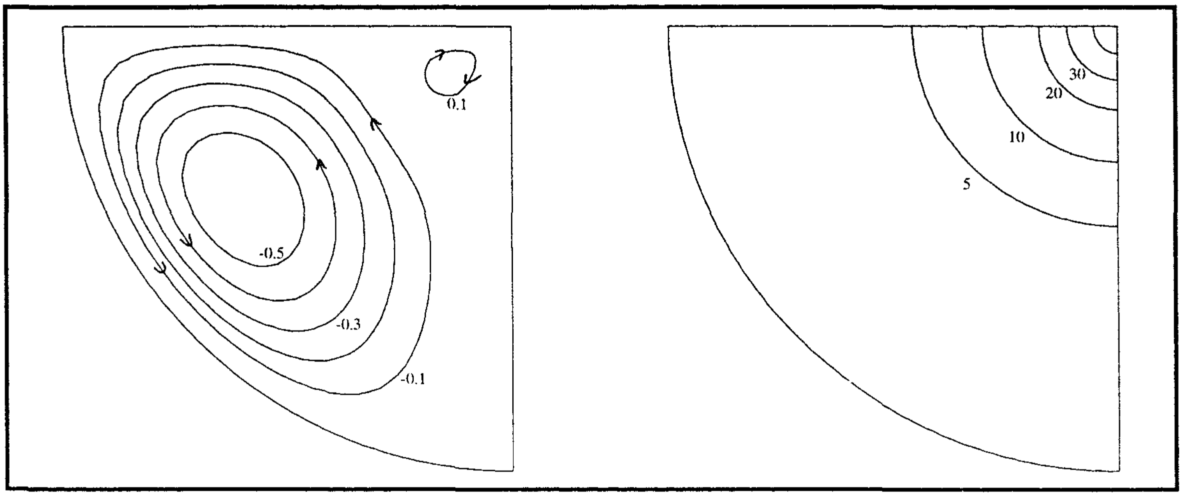

**Figure 4.6** - streamlines and isotherms for J=1A, $\beta=1.25*10^{-4}K^{-1}$, $\frac{\partial\gamma}{\partial T}=5*10^{-7}Nm^{-1}K^{-1}$

When added to a flow that is outward flowing on the top surface the buoyancy force makes a much smaller change. Figures 4.7 to 4.9 display streamlines for the flow at 1.5A with $\frac{\partial\gamma}{\partial T} = -3*10^{-6}Nm^{-1}K^{-1}$ and values for $\beta$ equal to 0, $5*10^{-5}$ and $1.25*10^{-4}K^{-1}$ respectively. For the first two cases the flows are virtually identical, whereas for the third the streamlines are not so closely packed near the top surface . This illustrates the fact that the buoyancy force is a body force, whereas the surface tension acts only on the surface of the fluid and causes the steep velocity profile there.

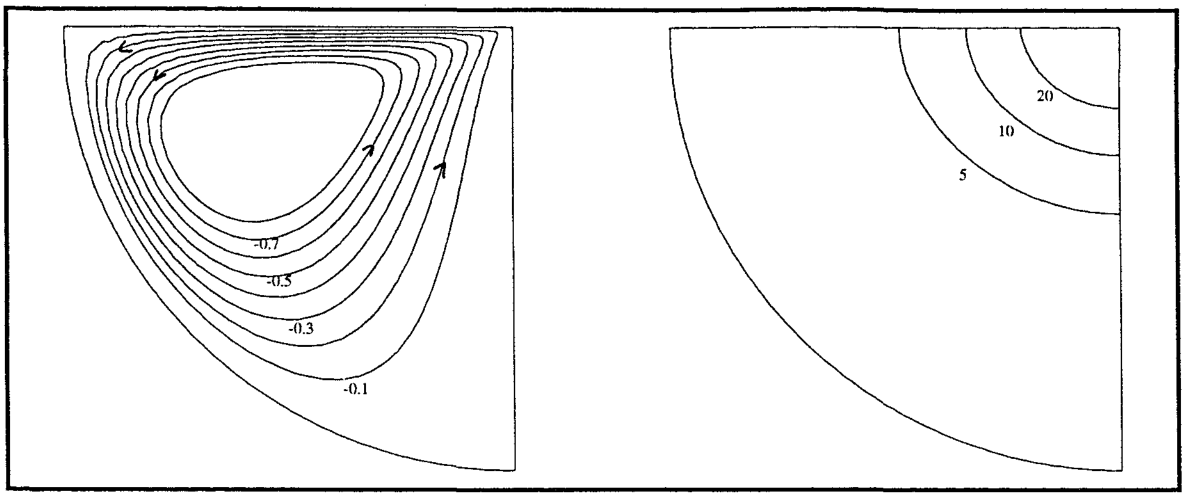

**Figure 4.7** - streamlines and isotherms for J=1.5A, $\beta$=0 $K^{-1}$, $\frac{\partial\gamma}{\partial T}$=-3*$10^{-6}Nm^{-1}K^{-1}$

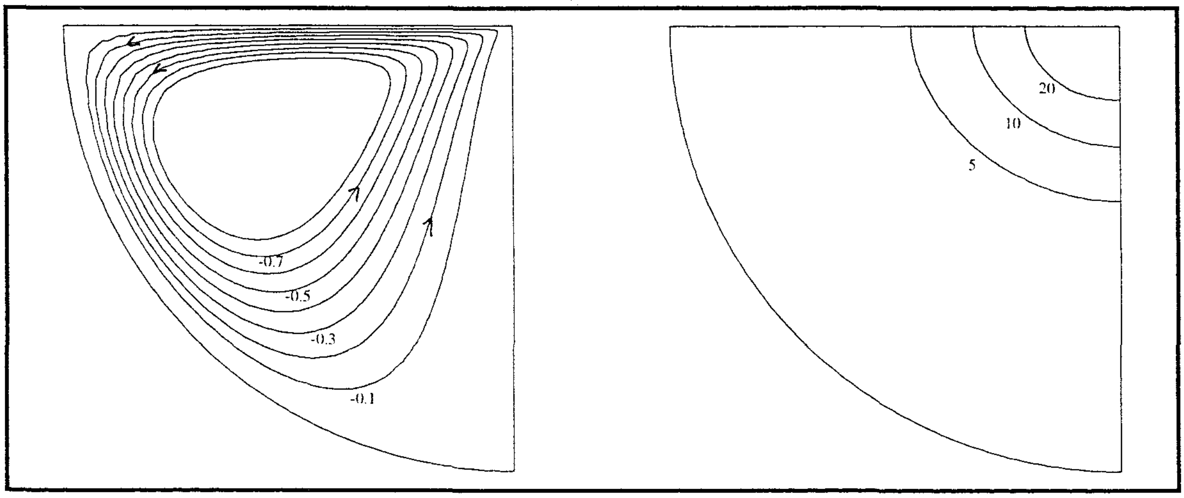

**Figure 4.8** - streamlines and isotherms for J=1.5A, $\beta$=5*$10^{-5}K^{-1}$, $\frac{\partial\gamma}{\partial T}$=-3*$10^{-6}Nm^{-1}K^{-1}$

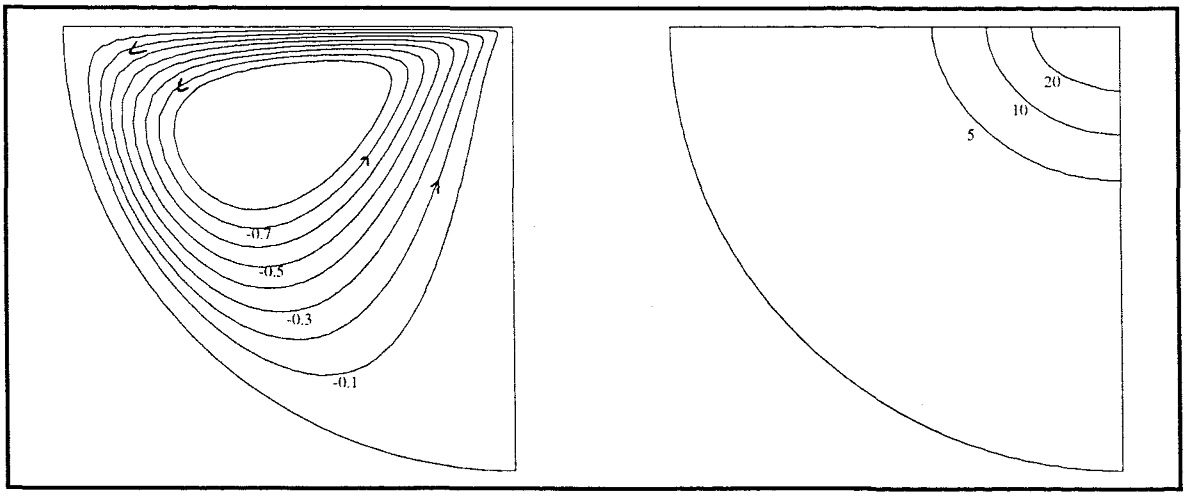

**Figure 4.9** - streamlines and isotherms for J=1.5A, $\beta$=1.25*$10^{-4}K^{-1}$, $\frac{\partial\gamma}{\partial T}$=-3*$10^{-6}Nm^{-1}K^{-1}$

The above results illustrate the effect the buoyancy force can have on the solutions for the flow field. The large qualitative differences present between figures 4.3 and 4.6 indicate that the inclusion of the buoyancy force in the model is essential to get a correct qualitative description of the flow for all parameter values. However, the size of the buoyancy force depends on the temperature difference across the weld pool and so will be roughly proportional to the heat input Q, which is proportional to the current. The Lorentz force, however, is proportional to the current squared, and hence the effect of buoyancy is expected to become less important as the current increases. Additionally, when $\frac{\partial\gamma}{\partial T}$ is large, the surface tension force dominates the flow at low currents and buoyancy has little effect on the flow patterns produced.

A more detailed discussion of the results obtained for the cases of positive and negative $\frac{\partial\gamma}{\partial T}$ is presented next.

### 4.5.3: Case 1 : positive $\frac{\partial\gamma}{\partial T}$

In this case the surface tension force is acting to reinforce the Lorentz force, but the buoyancy force opposes it. Despite its relatively small size compared to the other two forces, the buoyancy force, as has been shown above, can produce a reversal of the flow in a region of the weld pool, particularly when $\frac{\partial\gamma}{\partial T}$ is small and the current is low.

Figures 4.10 to 4.12 show the streamlines for the flow with a very small value for $\frac{\partial\gamma}{\partial T}$ of $10^{-7}Nm^{-1}K^{-1}$. Initially the flow is almost entirely driven by the buoyancy force, with just a small counter rotating loop near the origin, driven by the Lorentz and surface tension forces (figure 4.10). As the current is increased this loop grows, as the strength of the Lorentz force grows, expanding outwards from the origin (figure 4.11), until it dominates the entire flow (figure 4.12). As the value of $\frac{\partial\gamma}{\partial T}$ is increased the surface

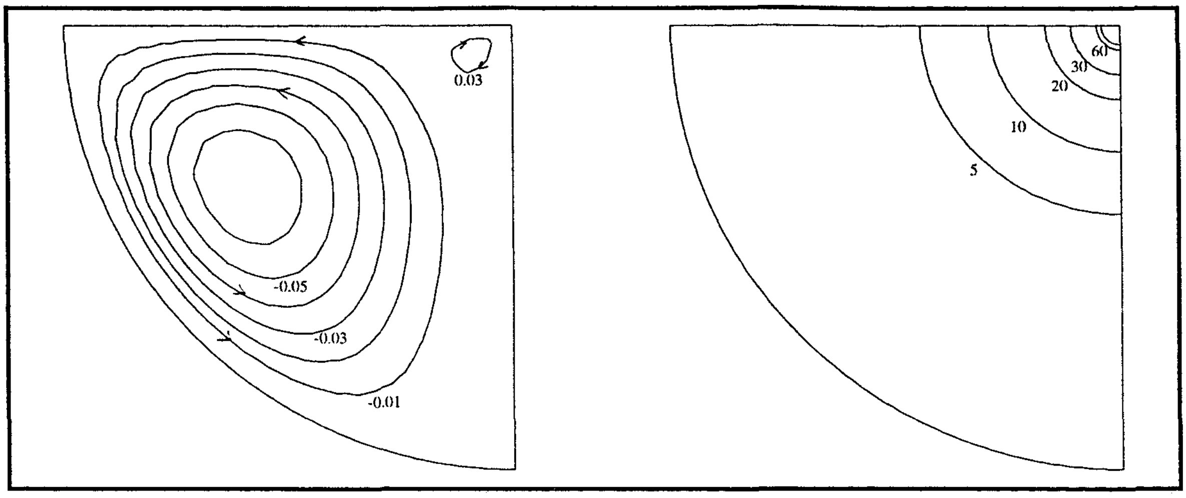

**Figure 4.10** - streamlines and isotherms for J=1.0A, $\beta=1.25*10^{-4}K^{-1}$, $\frac{\partial\gamma}{\partial T}=10^{-7}Nm^{-1}K^{-1}$

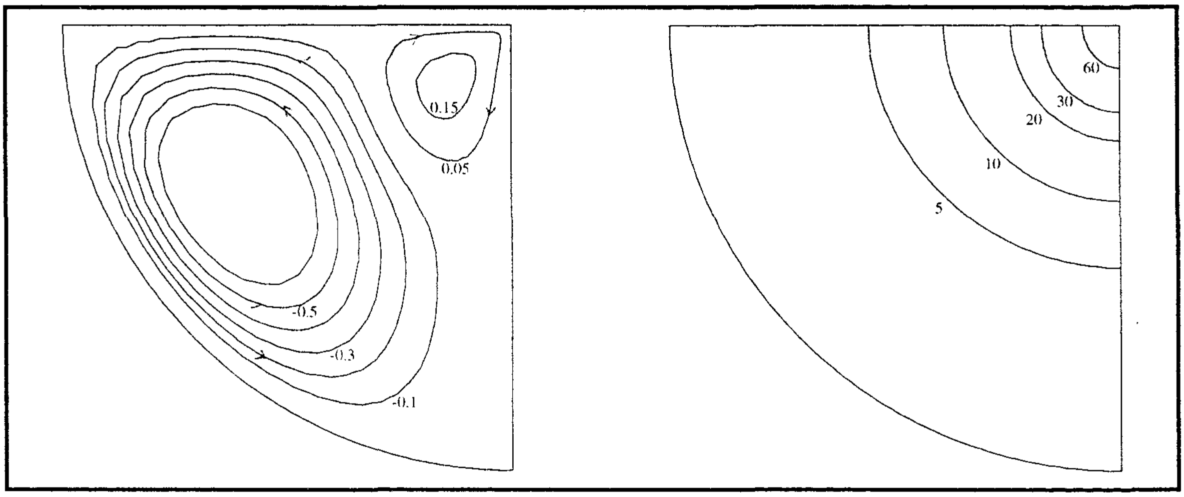

**Figure 4.11** - streamlines and isotherms for J=1.5A, $\beta=1.25*10^{-4}K^{-1}$, $\frac{\partial\gamma}{\partial T}=10^{-7}Nm^{-1}K^{-1}$

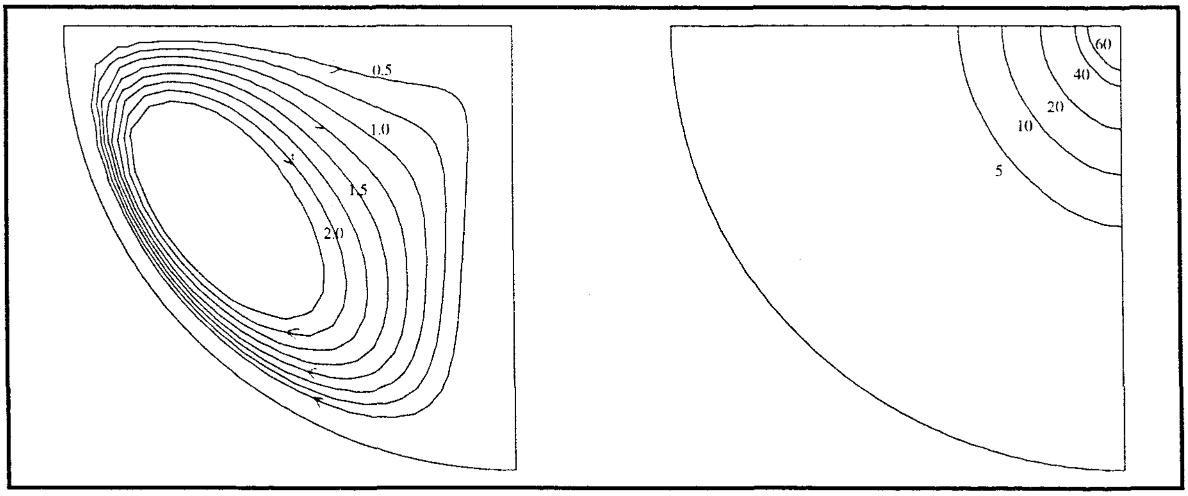

**Figure 4.12** - streamlines and isotherms for J=1.8A, $\beta=1.25*10^{-4}K^{-1}$, $\frac{\partial\gamma}{\partial T}=10^{-7}Nm^{-1}K^{-1}$

tension forces start to dominate the flow at low currents and the loop created by the buoyancy force decreases, and finally disappears. Approximate Reynolds numbers for these three cases are 7, 12 and 80 respectively.

Figure 4.13 shows the overall qualitative structure of the flow for values of J and $\frac{\partial \gamma}{\partial T}$. The lower solid line denotes the boundary between solutions containing one loop and those consisting of two loops, labelled with 1 and 2 respectively. The upper solid line marks the highest current values for which a solution could be obtained for a given value of $\frac{\partial \gamma}{\partial T}$. The dotted line represents the breakdown current for the similarity solution. It can be seen from figure 4.13 that the buoyancy force is strong enough to create a counter-rotating loop provided $\frac{\partial \gamma}{\partial T}$ is less than $10^{-5.5}Nm^{-1}K^{-1}$.

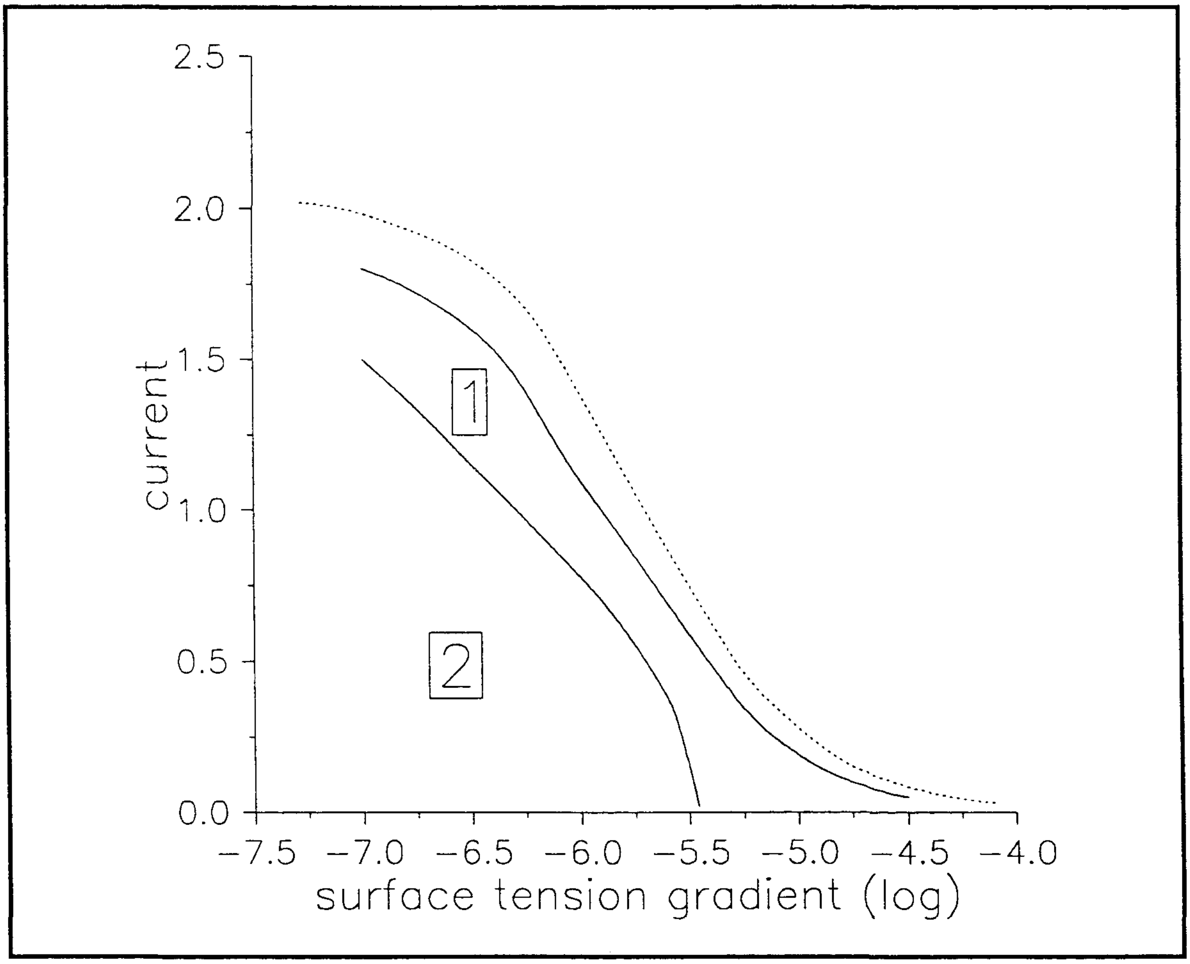

**Figure 4.13** - qualitative flow structure for positive $\frac{\partial \gamma}{\partial T}$

The loss of convergence of the method of solution seems to be due in all cases to a rapid increase in the velocity down the axis. Figures 4.14 and 4.15 show plots of the maximum value of G as the current increases for small and large values of $\frac{\partial \gamma}{\partial T}$, $10^{-7}\mathrm{Nm}^{-1}\mathrm{K}^{-1}$ and $10^{-5}\mathrm{Nm}^{-1}\mathrm{K}^{-1}$ respectively. In both cases there is a rapid increase in G, and hence fluid speed, approaching the value where it is impossible to obtain convergence. In Sozou and Pickering's solutions for the flow in a hemisphere under electromagnetic forces only, for both a point [ 103 ] and disk [ 104 ] current source, similar breakdown characteristics were displayed.

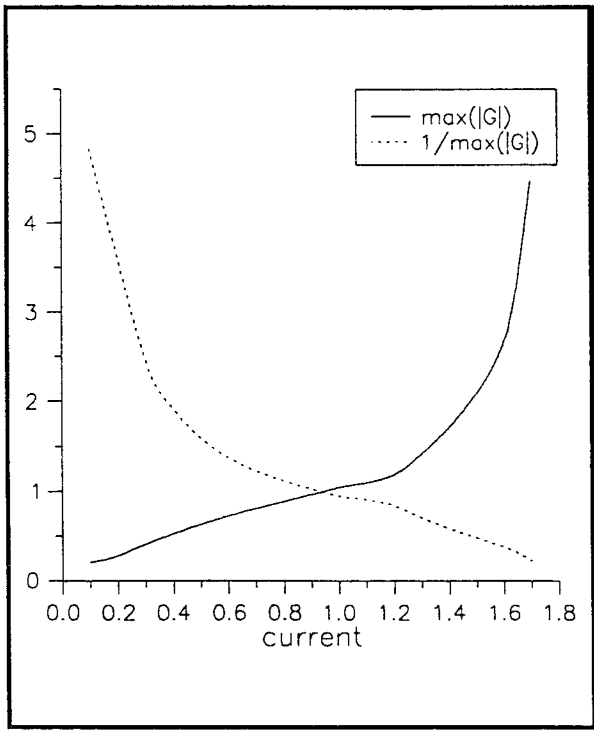

**Figure 4.14** - the chage in max(|G|) with current, for $\frac{\partial \gamma}{\partial T}=10^{-7}\mathrm{Nm}^{-1}\mathrm{K}^{-1}$

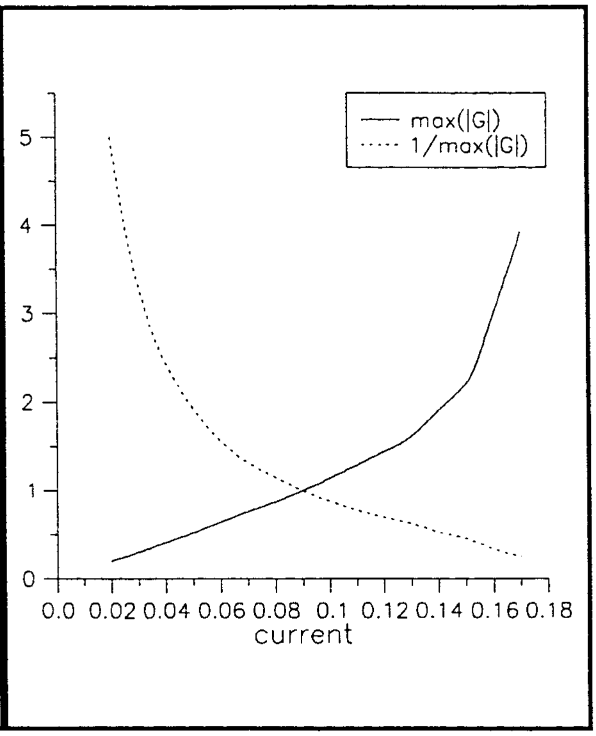

**Figure 4.15** - the chage in max(|G|) with current, for $\frac{\partial \gamma}{\partial T}=10^{-5}\mathrm{Nm}^{-1}\mathrm{K}^{-1}$

## 4.5.4: Case 2 : negative $\frac{\partial\gamma}{\partial T}$

In this case the surface tension force attempts to generate an outward flow on the top surface, opposing the Lorentz force.

At low currents, for all values of $\frac{\partial\gamma}{\partial T}$, the combined surface tension and buoyancy forces dominate over the Lorentz force, initially producing a circulation up the central axis and out along the top surface. As the current increases the structure of the flow changes, depending on the size of $\frac{\partial\gamma}{\partial T}$. For small values of $\frac{\partial\gamma}{\partial T}$ a counter rotating loop is produced at the origin, and this extends down the axis as the current is increased and the Lorentz force starts to dominate the other forces. When the current is increased further this second loop grows, but the solution stops converging before this second loop can dominate the entire flow. Figures 4.16 to 4.19 show the evolution of the flow for $\frac{\partial\gamma}{\partial T}= -2*10^{-7}Nm^{-1}K^{-1}$. Approximate Reynolds numbers for these cases are 1, 5, 7 and 28.

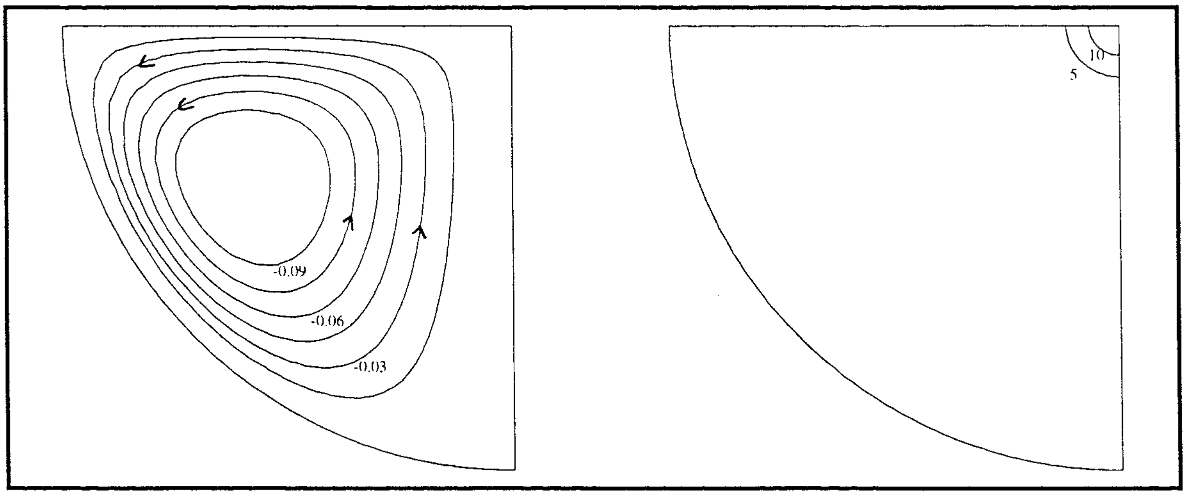

**Figure 4.16** - streamlines and isotherms for J=0.25A, $\beta=1.25*10^{-4}K^{-1}$, $\frac{\partial\gamma}{\partial T}=-2*10^{-7}Nm^{-1}K^{-1}$

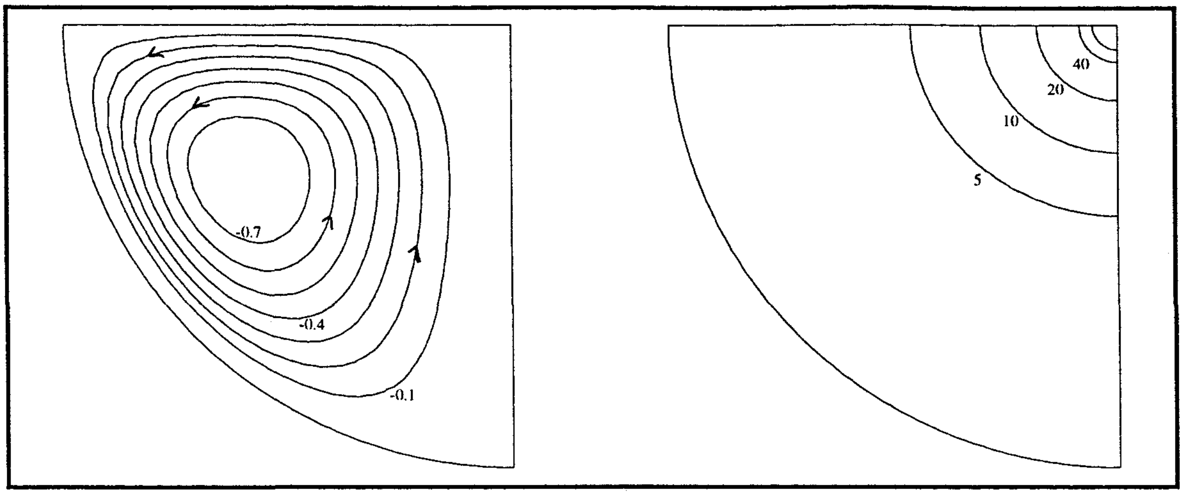

**Figure 4.17** - streamlines and isotherms for J=1.0A, $\beta=1.25*10^{-4}K^{-1}$, $\frac{\partial\gamma}{\partial T}=-2*10^{-7}Nm^{-1}K^{-1}$

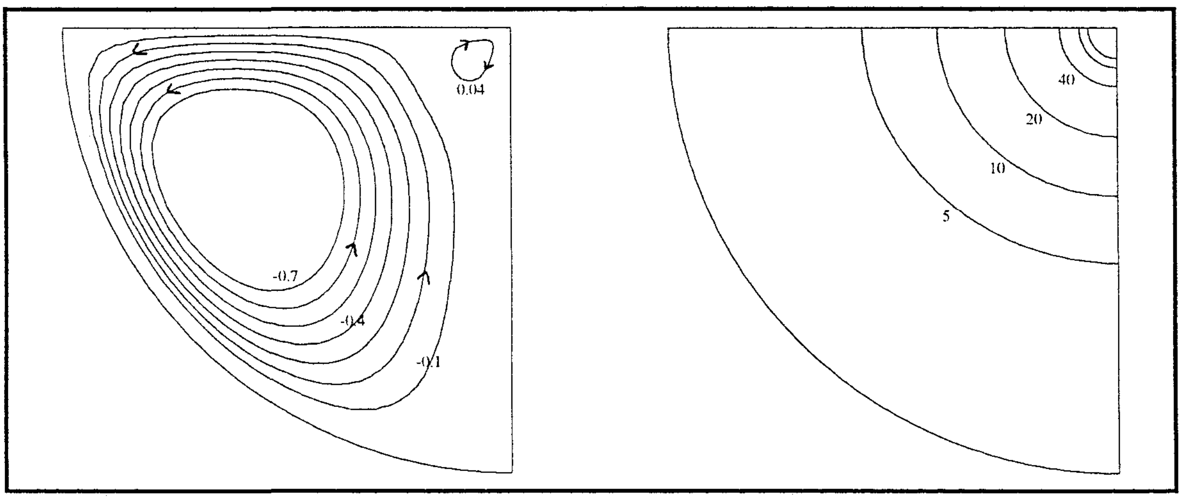

**Figure 4.18** - streamlines and isotherms for J=1.5A, $\beta=1.25*10^{-4}K^{-1}$, $\frac{\partial\gamma}{\partial T}=-2*10^{-7}Nm^{-1}K^{-1}$

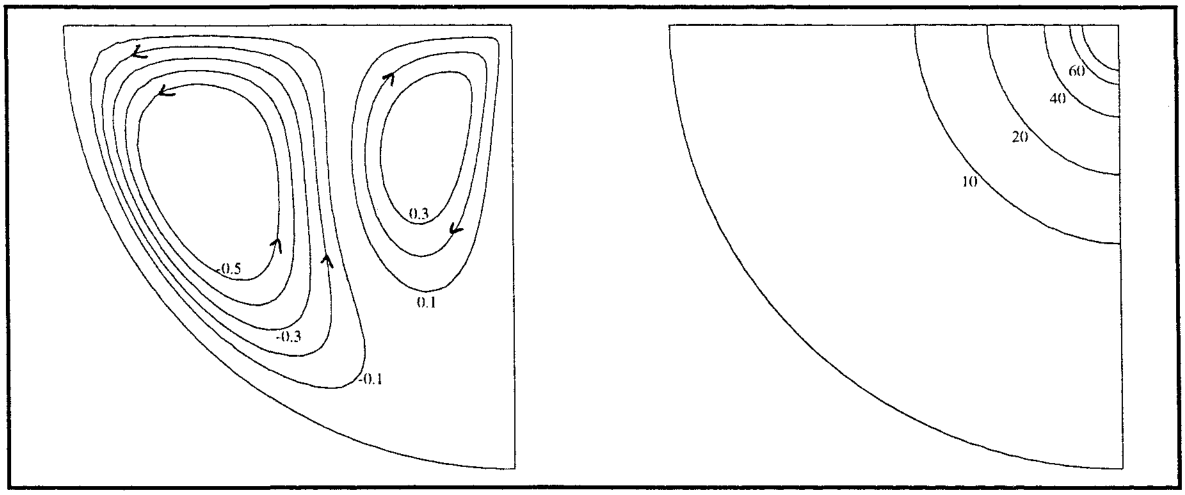

**Figure 4.19** - streamlines and isotherms for J=2.0A, $\beta=1.25*10^{-4}K^{-1}$, $\frac{\partial\gamma}{\partial T}=-2*10^{-7}Nm^{-1}K^{-1}$

For very large negative values of $\frac{\partial \gamma}{\partial T}$ another type of flow structure is observed. The surface tension force completely dominates the flow, producing a very strong outward jet flowing out along the top surface of the weld pool. The strength of this flow is such that it produces a strong circulating loop at the top of the weld pool, and a small slowly counter-rotating loop is produced at the base of the pool, figures 4.20 and 4.21. The pronounced irregularities in the streamlines and isotherms in these figures is due to the numerical method used to plot them and proved to be difficult to remove. They are not part of the actual flow structure. Approximate Reynolds numbers for the flows in these two cases are 90 and 450. The formation of two loops probably arises because the fast moving fluid has to turn through a sharp corner at the edge of the weld pool, and is then sucked back to the centre due to the large pressure differential between the centre and the edge of the weld pool. The fluid at the bottom of the pool, in comparison, has very little force acting on it since both the Lorentz and buoyancy forces are relatively small, especially at these low currents, and its motion is induced, therefore, by the rapidly moving fluid above it.

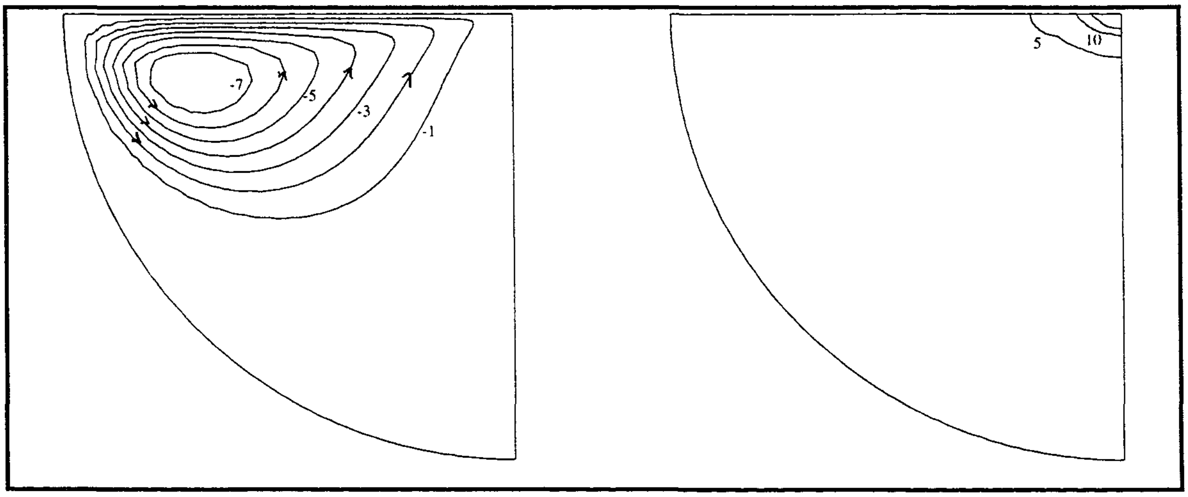

**Figure 4.20** - streamlines and isotherms for J=0.25A, $\beta=1.25*10^{-4}K^{-1}$, $\frac{\partial \gamma}{\partial T}=-10^{-4}Nm^{-1}K^{-1}$

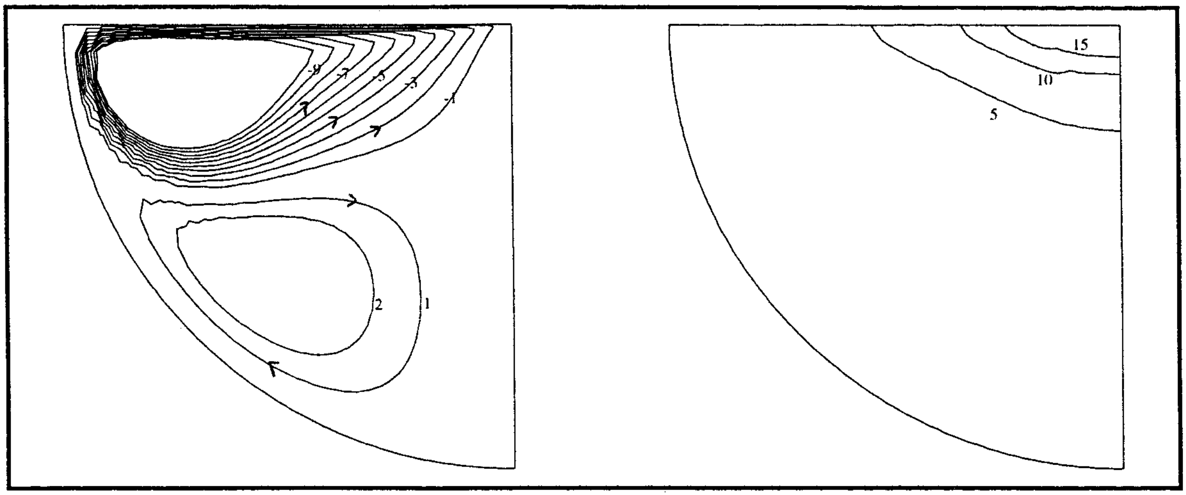

**Figure 4.21** - streamlines and isotherms for J=1.0A, $\beta=1.25*10^{-4}K^{-1}$, $\frac{\partial\gamma}{\partial T}=-10^{-4}Nm^{-1}K^{-1}$

The flow pattern discussed above is unlikely to occur in real weld pools, as a quick look at the isotherms makes obvious. The strong outward flow along the top surface would produce a weld pool that is wide and shallow, rather than the hemispherical shape specified here. As a consequence, the bottom part of the hemisphere, where the counter rotating loop occurs, would probably not be molten.

The qualitative structure of the flow at various parameter values is shown in figure 4.22.

The lower solid line denotes the boundary between the regions in parameter space which exhibit single- and double-looped flows, the regions labelled 1 and 2 respectively. The upper solid line denotes the largest current values at which a convergent solution was obtained, for a given value of $\frac{\partial\gamma}{\partial T}$. The dotted line indicates the current value at which the similarity solution breaks down, for comparison. Figure 4.22 suggests two possible reasons for the loss of convergence observed. For small negative values of $\frac{\partial\gamma}{\partial T}$ a solution can be found until the current value nears that of the breakdown of the similarity solution, indicating that the loss of convergence is due to the velocity tending towards infinity down the axis, as for positive values of $\frac{\partial\gamma}{\partial T}$.

For large negative $\frac{\partial\gamma}{\partial T}$, however, the loss of convergence occurs at a much lower current than the breakdown current for the similarity solution. This suggests that at high $\left|\frac{\partial\gamma}{\partial T}\right|$ the large velocity gradients at the top surface causes the numerical method to become unstable. Figure 4.23 shows a plot of the maximum value of G in the hemisphere versus the current, when $\frac{\partial\gamma}{\partial T}=-10^{-4}\mathrm{Nm^{-1}K^{-1}}$. From this figure it can be seen that the value of max(|G|) increases approximately linearly with the current, up to current values for which a solution cannot be obtained numerically. This is in contrast to the situations when $\frac{\partial\gamma}{\partial T}$ is either positive or small and negative, when a rapid increase in G is observed on approaching the current values for which solutions cannot be obtained.

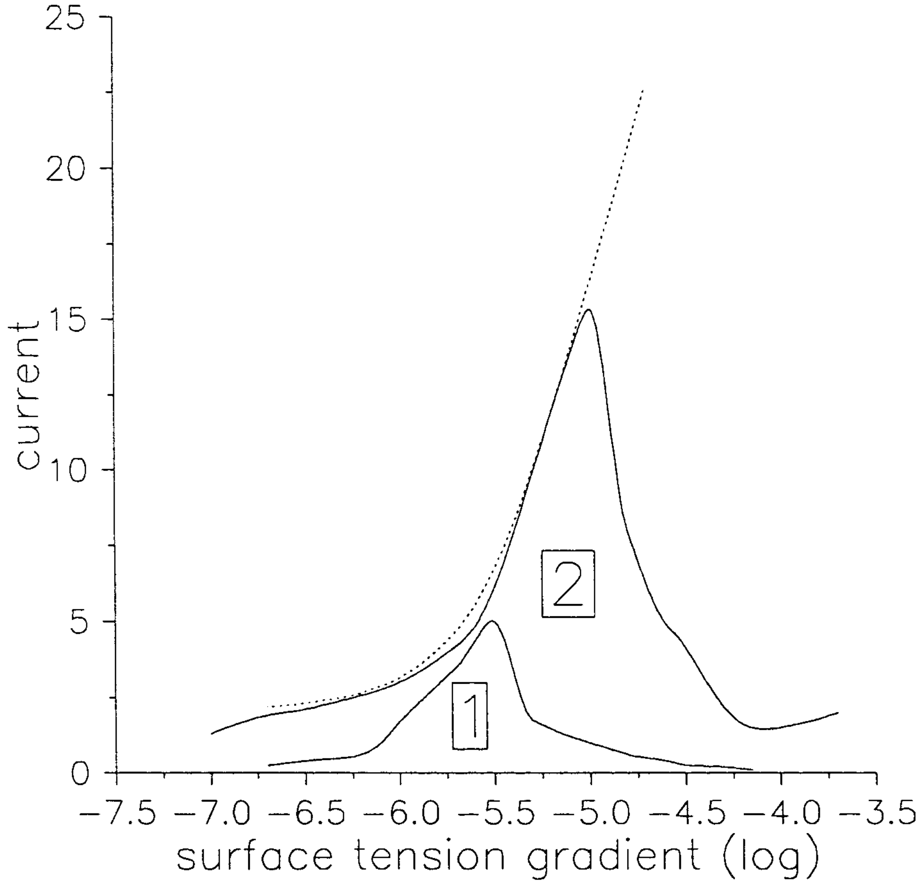

**Figure 4.22** - qualitative flow structure for negative $\frac{\partial\gamma}{\partial T}$

On considering the Reynolds numbers for the flow with $\frac{\partial \gamma}{\partial T}$=-$10^{-4}$Nm$^{-1}$K$^{-1}$ at J=0.25A and J=1.0A (figures 4.20 and 4.21) of 90 and 450 respectively, it can be seen that for the current value at which solutions can no longer be obtained the Reynolds number for the flow will be in the region of 1000. This would suggest that the flow may be becoming turbulent to some extent and this could be responsible for the non-convergence of the numerical scheme.

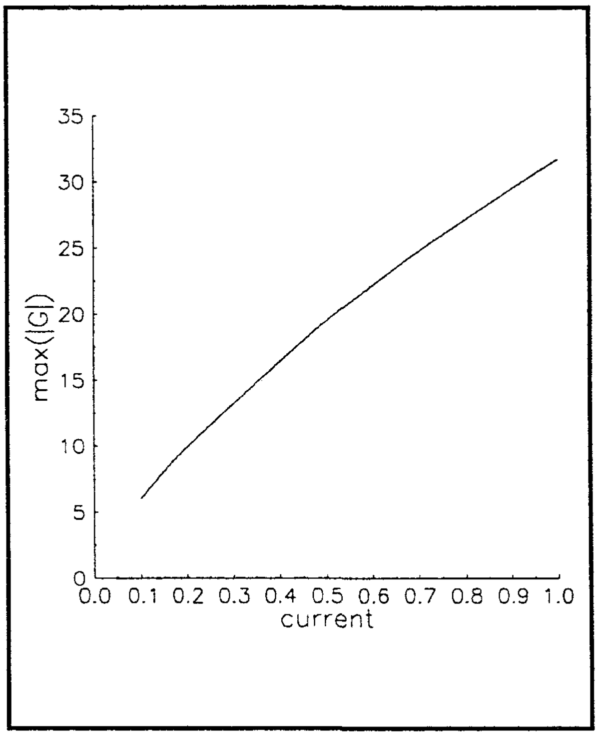

**Figure 4.23** - the chage in max(|G|) with current, for $\frac{\partial \gamma}{\partial T}$=-$10^{-4}$Nm$^{-1}$K$^{-1}$

# Chapter 5: Stability Analysis

## 5.1: Introduction

Researchers at Marchwood Laboratories noticed effects during welding experiments which they believed indicate the possible existence of multiple stable flows at a given welding current. Reinforcing this hypothesis, hysteresis effects have been observed in the size of the depression of the surface of the weld pool when the current is varied in the 200-300A region [ 62 ]. A stability analysis of the solutions found for the flow in the weld pool is therefore of great importance. However up to now there has been no published work on the stability of the solutions for the coupled heat and fluid flow obtained from the various models presented by many authors. A major problem in any such analysis is the fact that the basic flow is complicated and often obtained numerically. In this chapter a linear stability analysis is presented for the numerical solutions obtained in Chapter 4 for the flow in a hemisphere. A stability analysis for the similarity solution in Chapter 2 was not attempted because, as shown in the Appendix, there is no possibility of it bifurcating to a rotating flow, which has been shown to occur in experiments [ 11 ], [ 113 ].

The method of linear stability analysis was first introduced over a century ago by Lord Rayleigh [ 80 ], who developed a general linear stability theory for inviscid plane-parallel shear flows. In the years since then techniques have become more sophisticated, but in the majority of problems the fluid is either stationary, e.g. the onset of Benard-Marangoni convection in a layer of conducting fluid under the influence of a temperature gradient and magnetic field [ 111 ], or the fluid is undergoing motion which can be described analytically, often in a simple form, e.g. Taylor vortices in short cylinders [ 39 ][ 40 ], or convection in spherical annuli [ 30 ]. The most common methods of analysis used are the normal mode method, where the perturbations are expressed as a series of orthogonal functions in the coordinates, and one using energy considerations [ 17 ], [ 25 ].

Recently the method of geometrical optics has been applied to the flow of a non-viscous, incompressible fluid [ 26 ], [ 27 ] to analyse the stability of the flow to short wavelength perturbations. This method has shown that all axisymmetric flows such that the poloidal flow has a point of stagnation [ 60 ] and, also, all generic vortex rings [ 61 ] are unstable to short wavelength perturbations. However, these results do not carry over to viscous fluids since these perturbations will tend to be damped by the viscous forces, and hence the method is not applicable to the problem considered here.

In the stability analysis presented in this chapter the basic flow is only known numerically. Little analytic progress can be made, therefore, and the stability of the basic flow is investigated numerically.

A brief outline of linear stability analysis using the method of normal modes follows, as presented by Chandrasekhar [ 17 ]. This technique is then applied to the solution obtained in Chapter 4 for the flow in the hemisphere.

# 5.2: An introduction to linear stability theory

In many problems the equations of hydrodynamics allow simple flow patterns as stationary solutions. These flows can, however, only be realised for certain parameter values. The reason for this lies in their inherent instability, their inability to damp the small perturbations to which any physical system is subjected. Linear stability theory was introduced in an attempt to differentiate between the stable and unstable patterns of permissible flows. There follows a quick overview of the basic principles and concepts of the subject.

Suppose that we have a hydromagnetic system in a stationary state, described by a set of parameters $X_1,..X_j$. In determining the stability of the system we seek to determine the reaction of the system to small disturbances, specifically whether the disturbance will die down or if it will grow in amplitude such that the system departs from its initial state and never returns to it. If the former is true then the system is said to be stable with respect to the particular disturbance, otherwise it is unstable. Clearly a system can only be considered stable if it stable to all possible disturbances, i.e. there exists no mode for which it is unstable.

If all initial states are classified as stable or unstable, then in the space of parameters $X_1..X_j$, the locus which separates the two classes of states defines the marginal stability of the system (alternatively the state of neutral stability.) The determination of this locus is one of the prime objects of an investigation into stability.

It is often convenient to suppose that all parameters of the system are kept fixed, save one which is continuously varied. When this parameter reaches a particular critical value the system passes from a stable to an unstable state, which is called the point where instability sets in.

States of marginal stability can be of two kinds, corresponding to the way disturbances grow or are damped. They can grow (or be damped) aperiodically, or they can grow (or be damped) by oscillations of increasing (or decreasing) amplitude. In the former case the transition from stability to instability is via a marginal state exhibiting a stationary pattern of motions. In the latter the transition takes place via a marginal state showing oscillatory motions with a certain characteristic frequency. In the above statement it is assumed that the system is dissipative. For a non-dissipative and conservative system the results are different.

The linear stability analysis usually proceeds by taking a initial flow representing a stationary state, and supposing the various physical variables describing the flow suffer small (infinitesimal) perturbations. Equations are obtained governing these perturbations, and all products or powers greater than one are discarded leaving a set of linearised equations. Non-linear theories retain these terms and allow for perturbations of finite amplitude. All the work presented here is concerned only with infinitesimal perturbations.

For an investigation into stability to be complete it is necessary that the reaction to all possible disturbances be examined. This is normally done by expressing the perturbation by an expansion in terms of a superposition of basic modes (normal modes) and then examining the stability of this system with respect to each of these modes. The modes are chosen by considering the geometry of the system, and the symmetry of the initial solution.

If we denote the parameters describing the modes as **k**, then the perturbation A could be represented symbolically by

$$A(\boldsymbol{r},t) = \int A_k(\boldsymbol{r},t)\, dk\,.$$

The time dependence is eliminated by seeking solutions of the form

$$A_k(\boldsymbol{r},t) = A_k(\boldsymbol{r})e^{\sigma_k t},$$

where $\sigma_k$ is a constant to be determined. With this form for time dependence $\sigma_k$ will appear as a parameter in the equations which must be solved subject to appropriate boundary conditions. In general the equations will not allow non-trivial solutions for arbitrary $\sigma_k$. Requiring the existence of non-trivial solutions leads to a characteristic value problem for $\sigma_k$, and the original problem reduces to one of determining $\sigma_k$ for various modes **k**. In general the characteristic values for $\sigma_k$ will be complex, say,

$$\sigma_k = \sigma_k^{(r)} + i\,\sigma_k^{(i)},$$

where $\sigma_k^{(r)}$ and $\sigma_k^{(r)}$ will depend on the parameters $X_1,..X_j$ of the basic flow, as well as on **k**. The condition for stability is that $\sigma_k^{(r)}$ be negative for all **k**. The states of neutral stability will be characterised by

$$\sigma_k^{(r)}\left(X_1,..X_j\right)=0.$$

This condition defines a locus

$$\Sigma_k\left(X_1,..X_j\right)=0.$$

in $(X_1,..X_j)$-space, which separates the stable from the unstable states, for a particular mode **k**. It follows that the locus $\Sigma(X_1,..X_j)$ separating the regions of complete stability from the regions of instability in $(X_1,..X_j)$-space, the marginal stability curve, is the envelope of the loci $\Sigma_k$. Further when the system become unstable as we cross $\Sigma$ at some point, the mode of disturbance which will be manifested (at onset) will be the one whose locus $\Sigma_k$ touches $\Sigma$ at that point.

The distinction between the two kinds of marginal states (stationary or oscillatory) corresponds to whether the imaginary part of $\sigma_k$ vanishes with the real part. If $\sigma_k^{(r)}=0$ implies $\sigma_k^{(i)}=0$ then we have a stationary state, otherwise we will have overstability with $\sigma_k^{(i)}$ determining the characteristic frequency of the oscillations.

In practice evaluating $\sigma_k$ tends to be an extremely difficult task. Therefore, since the actual values of $\sigma_k^{(r)}$ are not needed, just the locus $\Sigma_k(X_1,..X_j)$, the value of $\sigma_k^{(r)}$ in the equations is set to zero and $\Sigma_k(X_1,..X_j)$ is calculated by looking for the existence of a non-trivial solution of the resulting equations, depending on the values of the parameters $X_1,..X_j$.

It is not always possible to check for all possible modes **k**. Hence, only the modes with the 'simplest' structure are often investigated, since in practical experiments the flow is likely to go through several changes in flow pattern as different modes become stable and unstable.

# 5.3: The stability of the hemisphere flow

## 5.3.1: Deriving the equations

The method outlined in the previous section is now applied to the flow in the hemisphere obtained in Chapter 4. If the 'stationary' solutions for velocity and temperature are denoted by **u** and $T_0$ respectively, and the infinitesimal perturbations to these solutions are denoted by **v** and T, then the new total velocity and temperature, denoted by **U** and $T_{tot}$, are

$$\mathbf{U} = \mathbf{v} + \mathbf{u}$$

and

$$T_{tot} = T + T_0.$$

These are now substituted into the time dependent form of the curl of the Navier-Stokes equation

$$\nabla\times\frac{\partial \mathbf{U}}{\partial t} = \nabla\times(\mathbf{U}\times(\nabla\times\mathbf{U})) - \nu\nabla\times\nabla\times\nabla\times\mathbf{U} + \frac{1}{\rho}\nabla\times\boldsymbol{F_B} + \frac{1}{\rho}\nabla\times(\boldsymbol{J}\times\boldsymbol{B})\,. \quad (5.1)$$

The latter is then expanded for **U** and $T_{tot}$, and any terms quadratic in the infinitesimal perturbations are discarded. The terms containing only **u** and $T_0$, and the **JxB** term, can be removed, since they form the stationary solution to equation (5.1). To reduce the algebraic complexity of the remaining equations a new variable **w**, the perturbation vorticity, is introduced, defined by **w**= curl **v**. Equation (5.1) then becomes

$$\frac{\partial \mathbf{w}}{\partial t} = \nabla\times(\mathbf{u}\times\mathbf{w}) + \nabla\times(\mathbf{v}\times(\nabla\times\mathbf{u})) - \nu\nabla\times\nabla\times\mathbf{w} + \frac{1}{\rho}\nabla\times\tilde{\boldsymbol{F}}_{\boldsymbol{B}}\,. \quad (5.2)$$

where $\tilde{\boldsymbol{F}}_{\boldsymbol{B}}$ is the bouyancy force due to the perturbed temperature.

Following the standard procedure the time dependence is set to be of the form $e^{\sigma t}$. The real part of $\sigma$, $\sigma^{(r)}$ ,is now set to zero and the existence of non-trivial solutions to the equations are sought. The parameter values where this occurs trace out the marginal stability curve, where $\sigma^{(r)}$ changes from negative to positive, ie. the curve in parameter space where the infinitesimal perturbations change from decaying to zero to growing exponentially. The value of the imaginary part of $\sigma$ was not sought, and hence only the real part of (5.2) was considered.

Each term in equation (5.2) is now expanded in terms of the components of **u**,**w** and **v**, with the subscripts denoting the relevant component of the vectors:

$$\mathbf{u}\times\mathbf{w} = \hat{\mathbf{r}}\, u_\theta w_\varphi - \hat{\theta}\, u_r w_\varphi + \hat{\Phi}\,(u_r w_\theta - u_\theta w_r).$$

$$\begin{aligned}
\nabla\times(\mathbf{u}\times\mathbf{w}) = {} & \hat{\mathbf{r}}\frac{1}{a\,\lambda\eta}\left(\frac{1}{2}\frac{\partial}{\partial\eta}\left[(u_r w_\theta - u_\theta w_r)\eta(2-\eta^2)^{1/2}\right] + \frac{1}{(2-\eta^2)^{1/2}}\frac{\partial}{\partial\varphi}\left(u_r w_\varphi\right)\right) \\
& + \hat{\theta}\frac{1}{a\,\lambda}\left(\frac{1}{\eta(2-\eta^2)^{1/2}}\frac{\partial}{\partial\varphi}\left(u_\theta w_\varphi\right) - \frac{\partial}{\partial\lambda}\left[\lambda\left(u_r w_\theta - u_\theta w_r\right)\right]\right) \\
& + \hat{\Phi}\frac{1}{a\lambda}\left(\frac{\partial}{\partial\lambda}\left(-\lambda u_r w_\varphi\right) - \frac{(2-\eta^2)^{1/2}}{2}\frac{\partial}{\partial\eta}\left(u_\theta w_\varphi\right)\right).
\end{aligned} \tag{5.3}$$

A new term u$_c$ is introduced, for convenience, defined by

$$\nabla\times\mathbf{u} = \hat{\Phi}\left(\frac{1}{a\lambda}\frac{\partial}{\partial\lambda}\left(\lambda u_\theta\right) - \frac{(2-\eta^2)^{1/2}}{2a\lambda}\frac{\partial u_r}{\partial\eta}\right) = \hat{\Phi}\, u_c,$$

and hence

$$\begin{aligned}
\nabla\times(\mathrm{v}\times\nabla\times\mathbf{u}) = {} & \hat{\mathbf{r}}\frac{1}{a\lambda\eta}\left(\frac{-1}{(2-\eta^2)^{1/2}}\frac{\partial}{\partial\varphi}(-\mathrm{v}_r u_c)\right) + \hat{\theta}\frac{1}{a\lambda}\left(\frac{1}{\eta(2-\eta^2)^{1/2}}\frac{\partial}{\partial\varphi}(\mathrm{v}_\theta u_c)\right) \\
& + \hat{\Phi}\frac{1}{a\lambda}\left(\frac{\partial}{\partial\lambda}\left(-\lambda\mathrm{v}_r u_c\right) - \frac{(2-\eta^2)^{1/2}}{2}\frac{\partial}{\partial\eta}\left(\mathrm{v}_\theta u_c\right)\right).
\end{aligned} \tag{5.4}$$

It also follows that

$$\begin{aligned}
\nabla\times\nabla\times\mathbf{w} = {} & \hat{\mathbf{r}}\frac{1}{a\lambda\eta}\Bigg(\frac{1}{2}\frac{\partial}{\partial\eta}\left[\frac{1}{a\lambda}\left\{\frac{\partial}{\partial\lambda}\left(\lambda w_\theta\right) - \frac{(2-\eta^2)^{1/2}}{2}\frac{\partial w_r}{\partial\eta}\right\}\eta(2-\eta^2)^{1/2}\right] \\
& -\frac{1}{(2-\eta^2)^{1/2}}\frac{\partial}{\partial\varphi}\left[\frac{1}{a\lambda}\left\{\frac{1}{\eta(2-\eta^2)^{1/2}}\frac{\partial w_r}{\partial\varphi} - \frac{\partial}{\partial\lambda}\left(\lambda w_\varphi\right)\right\}\right]\Bigg) \\
& + \hat{\theta}\frac{1}{a\lambda}\Bigg(\frac{1}{\eta(2-\eta^2)^{1/2}}\frac{\partial}{\partial\varphi}\left[\frac{1}{a\lambda\eta}\left\{\frac{1}{2}\frac{\partial}{\partial\eta}\left(w_\varphi\eta(2-\eta^2)^{1/2}\right) - \frac{1}{(2-\eta^2)^{1/2}}\frac{\partial w_\theta}{\partial\varphi}\right\}\right] \\
& \frac{-1}{a}\frac{\partial}{\partial\lambda}\left[\frac{\partial}{\partial\lambda}\left(\lambda w_\theta\right) - \frac{(2-\eta^2)^{1/2}}{2}\frac{\partial w_r}{\partial\eta}\right]\Bigg) \\
& + \hat{\Phi}\frac{1}{a^2\lambda}\Bigg(\frac{\partial}{\partial\lambda}\left[\frac{1}{\eta(2-\eta^2)^{1/2}}\frac{\partial w_r}{\partial\varphi} - \frac{\partial}{\partial\lambda}\left(\lambda w_\varphi\right)\right] \\
& \frac{-(2-\eta^2)^{1/2}}{2}\frac{\partial}{\partial\eta}\left[\frac{1}{\lambda\eta}\left\{\frac{1}{2}\frac{\partial}{\partial\eta}\left(w_\varphi(2-\eta^2)^{1/2}\eta\right) - \frac{1}{(2-\eta^2)^{1/2}}\frac{\partial w_\theta}{\partial\varphi}\right\}\right]\Bigg).
\end{aligned} \tag{5.5}$$

and **u** is given by

$$\mathbf{u} = \frac{\nu}{a\lambda}\left(\frac{g_\eta}{2\eta}, -\frac{(g+\lambda g_\lambda)}{\eta(2-\eta^2)^{1/2}}, 0\right) \qquad (5.6)$$

(c.f. equation (4.5)).

Since **u** and $T_0$ only depend on $\lambda$ and $\eta$, the perturbation can be chosen to be separable in $\phi$, and to have a $\phi$-dependence of the form $e^{im\varphi}$ so that $\frac{\partial}{\partial\varphi} \equiv im$, where m is a positive integer. The axisymmetric case, m=0, has not been considered since it changes the resulting equations considerably, although for a full analysis it should be included.

The perturbations can now be written as

$$w_r = \tilde{w}_r\,(\lambda,\eta)\; e^{(im\varphi+\sigma t)},$$

$$w_\theta = \tilde{w}_\theta\,(\lambda,\eta)\; e^{(im\varphi+\sigma t)},$$

$$w_\varphi = \tilde{w}_\varphi\,(\lambda,\eta)\; e^{(im\varphi+\sigma t)},$$

$$v_r = \tilde{v}_r\,(\lambda,\eta)\; e^{(im\varphi+\sigma t)},$$

$$v_\theta = \tilde{v}_\theta\,(\lambda,\eta)\; e^{(im\varphi+\sigma t)},$$

$$v_\varphi = \tilde{v}_\varphi\,(\lambda,\eta)\; e^{(im\varphi+\sigma t)},$$

$$T = \tilde{T}\,(\lambda,\eta)\; e^{(im\varphi+\sigma t)}.$$

These forms for the perturbations, together with equation (5.6) for **u**, are now substituted into (5.3), (5.4) and (5.5) , the tildes dropped and the equations divided through by $e^{(im\varphi+\sigma t)}$.

Equation (5.3) is then given by

$$\begin{aligned}\nabla\times(\mathbf{u}\times\ \mathbf{w}) = {}& \hat{\mathbf{r}}\,\frac{\nu}{2a^2\lambda^2\eta}\left(\frac{\partial}{\partial\eta}\left[\frac{(2-\eta^2)^{1/2}}{2}\,g_\eta w_\theta + (g+\lambda g_\lambda)w_r\right] + \frac{im}{\eta(2-\eta^2)^{1/2}}\,g_\eta w_\varphi\right)\\ & -\hat{\theta}\,\frac{\nu}{a^2\lambda\eta}\left(\frac{im}{\lambda\eta(2-\eta^2)}(g+\lambda g_\lambda)\,w_\varphi + \frac{\partial}{\partial\lambda}\left[\frac{g_\eta}{2}\,w_\theta + \frac{(g+\lambda g_\lambda)}{(2-\eta^2)^{1/2}}\,w_r\right]\right)\\ & +\hat{\Phi}\,\frac{\nu}{a^2\lambda}\left(\frac{(2-\eta^2)^{1/2}}{2\lambda}\,\frac{\partial}{\partial\eta}\left[\frac{(g+\lambda g_\lambda)}{\eta(2-\eta^2)^{1/2}}\,w_\varphi\right] - \frac{1}{2\eta}\,\frac{\partial}{\partial\lambda}\left(g_\eta w_\varphi\right)\right).\end{aligned}$$

On expanding the derivatives and collecting like terms in the perturbations this becomes

$$\begin{aligned}
\nabla\times(\mathbf{u}\times\ \mathbf{w}) = {} & \hat{\mathbf{r}}\,\frac{\nu}{2a^2\lambda^2\eta}\left(\frac{(2-\eta^2)^{1/2}}{2}\left(g_{\eta\eta}-\frac{\eta g_\eta}{(2-\eta^2)}\right)w_\theta+\frac{(2-\eta^2)^{1/2}}{2}\,g_\eta\frac{\partial w_\theta}{\partial\eta}+\left(g_\eta+\lambda g_{\lambda\eta}\right)w_r\right.\\
&\left.+(g+\lambda g_\lambda)\frac{\partial w_r}{\partial\eta}+\frac{im}{\eta(2-\eta^2)^{1/2}}\,g_\eta w_\varphi\right)\\
&-\hat{\theta}\,\frac{\nu}{a^2\lambda\eta}\left(\frac{im}{\lambda\eta(2-\eta^2)}\,(g+\lambda g_\lambda)\,w_\varphi+\frac{g_{\lambda\eta}}{2}\,w_\theta+\frac{g_\eta}{2}\frac{\partial w_\theta}{\partial\lambda}\right.\\
&\left.+\frac{(2g_\lambda+\lambda g_{\lambda\lambda})}{(2-\eta^2)^{1/2}}\,w_r+\frac{(g+\lambda g_\lambda)}{(2-\eta^2)^{1/2}}\frac{\partial w_r}{\partial\lambda}\right)\\
&+\hat{\Phi}\,\frac{\nu}{a^2\lambda}\left(-w_\varphi\left[\frac{(1-\eta^2)}{\lambda\eta^2(2-\eta^2)}(g+\lambda g_\lambda)-\frac{g_\eta}{2\lambda\eta}\right]+\frac{(g+\lambda g_\lambda)}{2\lambda\eta}\frac{\partial w_\varphi}{\partial\eta}-\frac{g_\eta}{2\eta}\frac{\partial w_\varphi}{\partial\lambda}\right).
\end{aligned}\tag{5.7}$$

Equation (5.4) is now given by

$$\begin{aligned}
\nabla\times(\mathbf{v}\times\nabla\times\mathbf{u}) = {} & \hat{\mathbf{r}}\,\frac{im}{a\lambda\eta(2-\eta^2)^{1/2}}\,v_r u_c+\hat{\theta}\,\frac{im}{a\lambda\eta(2-\eta^2)^{1/2}}\,v_\theta u_c\\
&-\hat{\Phi}\,\frac{1}{a\lambda}\left(\frac{\partial}{\partial\lambda}\left(\lambda v_r u_c\right)+\frac{(2-\eta^2)^{1/2}}{2}\frac{\partial}{\partial\eta}\left(v_\theta u_c\right)\right).
\end{aligned}\tag{5.8}$$

Making use of equation (5.6), $u_c$ can be expressed

$$u_c=-\frac{\nu}{a^2\lambda\eta}\left(\frac{(2g_\lambda+\lambda g_{\lambda\lambda})}{(2-\eta^2)^{1/2}}+\frac{(2-\eta^2)^{1/2}}{4\lambda}\left(g_{\eta\eta}-\frac{g_\eta}{\eta}\right)\right),$$

and so (5.8) becomes

$$\begin{aligned}
\nabla\times(\mathbf{v}\times\nabla\times\mathbf{u}) = {} & -\hat{\mathbf{r}}\,\frac{\nu im}{a^3\lambda^2\eta^2}\left(\frac{(2g_\lambda+\lambda g_{\lambda\lambda})}{(2-\eta^2)}+\frac{1}{4\lambda}\left(g_{\eta\eta}-\frac{g_\eta}{\eta}\right)\right)v_r\\
&-\hat{\theta}\,\frac{\nu im}{a^3\lambda^2\eta^2}\left(\frac{(2g_\lambda+\lambda g_{\lambda\lambda})}{(2-\eta^2)}+\frac{1}{4\lambda}\left(g_{\eta\eta}-\frac{g_\eta}{\eta}\right)\right)v_\theta\\
&+\hat{\Phi}\,\frac{\nu}{a^3\lambda}\left(\frac{(2-\eta^2)^{1/2}}{\eta}\left[\frac{(3g_{\lambda\lambda}+\lambda g_{\lambda\lambda\lambda})}{(2-\eta^2)}+\frac{1}{4\lambda}\left(g_{\lambda\eta\eta}-\frac{g_{\lambda\eta}}{\eta}\right)-\frac{1}{4\lambda^2}\left(g_{\eta\eta}-\frac{g_\eta}{\eta}\right)\right]v_r\right.\\
&+\frac{(2-\eta^2)^{1/2}}{\eta}\left[\frac{(2g_\lambda+\lambda g_{\lambda\lambda})}{(2-\eta^2)}+\frac{1}{4\lambda}\left(g_{\eta\eta}-\frac{g_\eta}{\eta}\right)\right]\frac{\partial v_r}{\partial\lambda}\\
&+\left[\frac{(2g_{\lambda\eta}+\lambda g_{\lambda\lambda\eta})}{\eta}-\frac{2(1-\eta^2)}{\eta^2(2-\eta^2)}\,(2g_\lambda+\lambda g_{\lambda\lambda})-\frac{1}{2\lambda\eta^2}\left(g_{\eta\eta}-\frac{g_\eta}{\eta}\right)\right.\\
&\left.+\frac{(2-\eta^2)}{4\lambda\eta}\left(g_{\eta\eta\eta}-\frac{g_{\eta\eta}}{\eta}+\frac{g_\eta}{\eta^2}\right)\right]\frac{v_\theta}{2\lambda}\\
&\left.+\frac{1}{2\lambda\eta}\left[\frac{(2-\eta^2)}{4\lambda}\left(g_{\eta\eta}-\frac{g_\eta}{\eta}\right)+(2g_\lambda+\lambda g_{\lambda\lambda})\right]\frac{\partial v_\theta}{\partial\eta}\right).
\end{aligned}\tag{5.9}$$

In an analogous way equation (5.5) can be written

$$\begin{aligned}
\nabla\times\nabla\times\mathbf{w} = {}& \hat{\mathbf{r}}\,\frac{1}{a^2\lambda^2\eta}\left(\frac{1}{2}\,\eta(2-\eta^2)^{½}\left[\frac{\partial w_\theta}{\partial\eta}+\lambda\frac{\partial^2 w_\theta}{\partial\lambda\partial\eta}\right]+\frac{(1-\eta^2)}{(2-\eta^2)^{½}}\left[w_\theta+\lambda\frac{\partial w_\theta}{\partial\lambda}\right]\right. \\
& \left.-\frac{1}{4}\left[(2-3\eta^2)\frac{\partial w_r}{\partial\eta}+\eta(2-\eta^2)\,\frac{\partial^2 w_r}{\partial\eta^2}\right]+\frac{m^2}{\eta(2-\eta^2)}\,w_r+\frac{im}{(2-\eta^2)^{½}}\left[\text{‘}w_\varphi+\lambda\frac{\partial w_\varphi}{\partial\lambda}\right]\right) \\
& +\hat{\theta}\,\frac{1}{a^2\lambda}\left(\frac{im}{\lambda}\left[\frac{1}{2\eta}\,\frac{\partial w_\varphi}{\partial\eta}+\frac{(1-\eta^2)}{\eta^2(2-\eta^2)}\,w_\varphi\right]+\frac{m^2}{\lambda\eta^2(2-\eta^2)}\,w_\theta-\left[2\,\frac{\partial w_\theta}{\partial\lambda}+\lambda\frac{\partial^2 w_\theta}{\partial\lambda^2}\right]\right. \\
& \left.+\frac{(2-\eta^2)^{½}}{2}\,\frac{\partial^2 w_r}{\partial\lambda\partial\eta}\right) \\
& +\hat{\Phi}\,\frac{1}{a^2\lambda}\left(\frac{im}{\eta(2-\eta^2)^{½}}\,\frac{\partial w_r}{\partial\lambda}-\left[2\,\frac{\partial w_\varphi}{\partial\lambda}+\lambda\frac{\partial^2 w_\varphi}{\partial\lambda^2}\right]-\frac{1}{4\lambda}\left[\frac{(2-3\eta^2)}{\eta}\,\frac{\partial w_\varphi}{\partial\eta}+(2-\eta^2)\,\frac{\partial^2 w_\varphi}{\partial\eta^2}\right.\right. \\
& \left.\left.-\frac{4w_\varphi}{\eta^2(2-\eta^2)}\right]+\frac{im}{2\lambda}\left[\frac{1}{\eta}\,\frac{\partial w_\theta}{\partial\eta}-\frac{2(1-\eta^2)}{\eta^2(2-\eta^2)}\,w_\theta\right]\right). \qquad (5.10)
\end{aligned}$$

Finally considering the buoyancy term,

$$\begin{aligned}
F_B &= \beta\rho g_e\,(\cos\theta\,,-\sin\theta\,,0\,)\;T \\
&= \beta\rho g_e\,(\,(1-\eta^2)\,,-\eta(2-\eta^2)^{½}\,,0\,)\;T\,, \\
\frac{1}{\rho}\,\nabla\times F_B &= \hat{\mathbf{r}}\,\frac{im\beta g_e}{a\lambda}\,T+\hat{\theta}\,\frac{(1-\eta^2)}{a\lambda\eta(2-\eta^2)^{½}}\,im\beta g_e\,T \\
&\quad-\hat{\Phi}\,\frac{\beta\rho g_e\,(2-\eta^2)^{½}}{a}\left(\eta\,\frac{\partial T}{\partial\lambda}+\frac{(1-\eta^2)}{2\lambda}\,\frac{\partial T}{\partial\eta}\right) \qquad (5.11)
\end{aligned}$$

Gathering together the components of equations (5.7), (5.9), (5.10) and (5.11) the three components of equation (5.2) can now be written down.

First the r-component, multiplied by $\frac{a^2\lambda^2\eta}{\nu}$, yields the equation

$$\begin{aligned}
& -\frac{ima\beta g_e\,\lambda\eta}{\nu}\,T+\mathrm{v_r}\,\frac{im}{a\eta}\left(\frac{(2g_\lambda+\lambda g_{\lambda\lambda})}{(2-\eta^2)}+\frac{1}{4\lambda}\left(g_{\eta\eta}-\frac{g_\eta}{\eta}\right)\right)+w_r\,\frac{1}{2}\left(\frac{2m^2}{\eta(2-\eta^2)}-\left(g_\eta+\lambda g_{\lambda\eta}\right)\right) \\
& +\frac{\partial w_r}{\partial\eta}\,\frac{1}{4}\left(-2(g+\lambda g_\lambda)-(2-3\eta^2)\right)+\frac{\partial^2 w_r}{\partial\eta^2}\left(\frac{-\eta(2-\eta^2)}{4}\right) \qquad (5.12) \\
& +w_\theta\,\frac{(2-\eta^2)^{½}}{4}\left(\frac{4(1-\eta^2)}{(2-\eta^2)}-g_{\eta\eta}+\frac{\eta g_\eta}{(2-\eta^2)}\right)+\frac{\partial w_\theta}{\partial\eta}\left(\frac{(2-\eta^2)^{½}\,(2\eta-g_\eta)}{4}\right) \\
& +\frac{\partial w_\theta}{\partial\lambda}\left(\frac{\lambda(1-\eta^2)}{(2-\eta^2)^{½}}\right)+\frac{\partial^2 w_\theta}{\partial\lambda\partial\eta}\left(\frac{\lambda\,\eta(2-\eta^2)^{½}}{2}\right)+w_\varphi\,\frac{im}{(2-\eta^2)^{½}}\,(1-\frac{g_\eta}{2\eta})+\frac{\partial w_\varphi}{\partial\lambda}\left(\frac{\lambda im}{(2-\eta^2)^{½}}\right)=0.
\end{aligned}$$

Next the θ-component, multiplied by $\frac{a^2\lambda\eta}{\nu}$, is given by

$$\begin{aligned}
&-\frac{ima\beta g_e\,(1-\eta^2)}{\nu(2-\eta^2)^{1/2}}\,T+\mathrm{v}_\theta\,\frac{im}{a\lambda\eta}\left(\frac{(2g_\lambda+\lambda g_{\lambda\lambda})}{(2-\eta^2)}+\frac{1}{4\lambda}\left(g_{\eta\eta}-\frac{g_\eta}{\eta}\right)\right)+w_r\left(\frac{(2g_\lambda+\lambda g_{\lambda\lambda})}{(2-\eta^2)^{1/2}}\right)\\
&+\frac{\partial w_r}{\partial\lambda}\left(\frac{(g+\lambda g_\lambda)}{(2-\eta^2)^{1/2}}\right)+\frac{\partial^2 w_r}{\partial\lambda\partial\eta}\left(\frac{\eta(2-\eta^2)^{1/2}}{2}\right)+w_\theta\left(\frac{m^2}{\lambda\eta(2-\eta^2)}+\frac{g_{\lambda\eta}}{2}\right)\\
&+\frac{\partial w_\theta}{\partial\lambda}\left(\frac{g_\eta}{2}-2\eta\right)+\frac{\partial^2 w_\theta}{\partial\lambda^2}\,(-\lambda\eta)+w_\varphi\left(\frac{im\,(\,(1-\eta^2)+(g+\lambda g_\lambda)\,)}{\lambda\eta(2-\eta^2)}\right)+\frac{\partial w_\varphi}{\partial\eta}\left(\frac{im}{2\lambda}\right)=0.
\end{aligned}\tag{5.13}$$

Finally the phi component, multiplied by $\frac{a^2\lambda\eta}{\nu}$, is given by

$$\begin{aligned}
&\frac{a\beta g_e\,(2-\eta^2)^{1/2}(1-\eta^2)\eta}{2\nu}\,\frac{\partial T}{\partial\eta}+\frac{a\beta\rho g_e\,(2-\eta^2)^{1/2}\eta^2\lambda}{\nu}\,\frac{\partial T}{\partial\lambda}+\frac{\partial w_r}{\partial\lambda}\left(\frac{im}{(2-\eta^2)^{1/2}}\right)+w_\theta\left(\frac{-im(1-\eta^2)}{\lambda\eta(2-\eta^2)}\right)\\
&+\frac{\partial w_\theta}{\partial\eta}\left(\frac{im}{2\lambda}\right)+w_\varphi\left(\frac{1}{\lambda\eta(2-\eta^2)}-\frac{g_\eta}{2\lambda}+\frac{(1-\eta^2)}{\lambda\eta(2-\eta^2)}\,(g+\lambda g_\lambda)\right)+\frac{\partial w_\varphi}{\partial\lambda}\left(\frac{g_\eta}{2}-2\eta\right)\\
&+\frac{\partial^2 w_\varphi}{\partial\lambda^2}\,(-\lambda\eta)+\frac{\partial w_\varphi}{\partial\eta}\left(\frac{-(g+\lambda g_\lambda)}{2\lambda}-\frac{(2-3\eta^2)}{4\lambda}\right)+\frac{\partial^2 w_\varphi}{\partial\eta^2}\left(\frac{-\eta(2-\eta^2)}{4\lambda}\right)\\
&+\mathrm{v}_\mathrm{r}\,\frac{(2-\eta^2)^{1/2}}{a}\left(\frac{1}{4\lambda^2}\left(g_{\eta\eta}-\frac{g_\eta}{\eta}\right)-\frac{1}{4\lambda}\left(g_{\lambda\eta\eta}-\frac{g_{\lambda\eta}}{\eta}\right)-\frac{(3g_{\lambda\lambda}+\lambda g_{\lambda\lambda\lambda})}{(2-\eta^2)}\right)\\
&+\frac{\partial \mathrm{v}_\mathrm{r}}{\partial\lambda}\,\frac{(2-\eta^2)^{1/2}}{a}\left(\frac{-(2g_\lambda+\lambda g_{\lambda\lambda})}{(2-\eta^2)}-\frac{1}{4\lambda}\left(g_{\eta\eta}-\frac{g_\eta}{\eta}\right)\right)\\
&+\mathrm{v}_\theta\,\frac{1}{2a\lambda}\left(\frac{2(1-\eta^2)}{\eta(2-\eta^2)}\left(2g_\lambda+\lambda g_{\lambda\lambda}\right)-\left(2g_{\lambda\eta}+\lambda g_{\lambda\lambda\eta}\right)-\frac{(2-\eta^2)}{4\lambda}\,g_{\eta\eta\eta}+\frac{(4-\eta^2)}{4\lambda\eta}\,g_{\eta\eta}-\frac{(4-\eta^2)}{4\lambda\eta^2}\,g_\eta\right)\\
&+\frac{\partial \mathrm{v}_\theta}{\partial\eta}\,\frac{1}{2a\lambda}\left(\frac{-(2-\eta^2)}{4\lambda}\left(g_{\eta\eta}-\frac{g_\eta}{\eta}\right)-\left(2g_\lambda+\lambda g_{\lambda\lambda}\right)\right)=0.
\end{aligned}\tag{5.14}$$

Since **w** is defined as curl **v**, vector identities give div **w** = 0. This fact can be used to eliminate $w_\phi$ and its derivatives from equations (5.12), (5.13), (5.14):

$$\nabla.\mathbf{w}=\frac{1}{a\lambda^2}\frac{\partial}{\partial\lambda}\left(\lambda^2 w_r\right)+\frac{1}{2a\lambda\eta}\frac{\partial}{\partial\eta}\left(w_\theta\,\eta(2-\eta^2)^{1/2}\right)+\frac{1}{a\lambda\eta(2-\eta^2)^{1/2}}\frac{\partial w_\varphi}{\partial\varphi}=0, \tag{5.15}$$

so

$$w_\varphi=\frac{i}{m}\left(\eta(2-\eta^2)^{1/2}\left[2w_r+\lambda\frac{\partial w_r}{\partial\lambda}\right]+(1-\eta^2)\,w_\theta+\frac{\eta(2-\eta^2)}{2}\frac{\partial w_\theta}{\partial\eta}\right) \tag{5.16}$$

Diffentiating equation (5.16) leads to

$$\frac{\partial w_\varphi}{\partial \lambda} = \frac{i}{m}\left(\eta(2-\eta^2)^{1/2}\left[3\frac{\partial w_r}{\partial \lambda} + \lambda\frac{\partial^2 w_r}{\partial \lambda^2}\right] + (1-\eta^2)\frac{\partial w_\theta}{\partial \lambda} + \frac{\eta(2-\eta^2)}{2}\frac{\partial^2 w_\theta}{\partial \lambda \partial \eta}\right) \tag{5.17}$$

and

$$\begin{aligned}\frac{\partial w_\varphi}{\partial \eta} = \frac{i}{m}\Bigg(&\eta(2-\eta^2)^{1/2}\left[2\frac{\partial w_r}{\partial \eta} + \lambda\frac{\partial^2 w_r}{\partial \lambda \partial \eta}\right] + \frac{2(1-\eta^2)}{(2-\eta^2)^{1/2}}\left[2w_r + \lambda\frac{\partial w_r}{\partial \lambda}\right] \\ &- 2\eta w_\theta + \frac{(4-5\eta^2)}{2}\frac{\partial w_\theta}{\partial \eta} + \frac{\eta(2-\eta^2)}{2}\frac{\partial^2 w_\theta}{\partial \eta^2}\Bigg)\end{aligned} \tag{5.18}$$

To make equations (5.16) to (5.18) purely real, the substitutions $w_r = i\,\tilde{w}_r$ and $w_\theta = i\,\tilde{w}_\theta$ are introduced. Equations (5.12) and (5.13) are multiplied through by i, the tildes dropped, and finally $w_\phi$ and its derivatives are eliminated using (5.16), (5.17), and (5.18). This leads to the final equations

$$\begin{aligned}&\frac{ma\beta g_e\,\lambda\eta}{\nu}T - \mathrm{v}_r\frac{m}{a\eta}\left(\frac{(2g_\lambda + \lambda g_{\lambda\lambda})}{(2-\eta^2)} + \frac{1}{4\lambda}\left(g_{\eta\eta} - \frac{g_\eta}{\eta}\right)\right) - w_r\left(\frac{(g_\eta - \lambda g_{\lambda\eta})}{2} + \frac{m^2}{\eta(2-\eta^2)} - 2\eta\right) \\ &+ \frac{\partial w_r}{\partial \lambda}\lambda\left(\frac{-g_\eta}{2} + 4\eta\right) + \frac{\partial^2 w_r}{\partial \lambda^2}\left(\lambda^2\eta\right) + \frac{\partial w_r}{\partial \eta}\left(\frac{(g + \lambda g_\lambda)}{2} + \frac{(2-3\eta^2)}{4}\right) \\ &+ \frac{\partial^2 w_r}{\partial \eta^2}\left(\frac{\eta(2-\eta^2)}{4}\right) + w_\theta\frac{(2-\eta^2)^{1/2}}{4}\left(\frac{-g_\eta}{\eta} + g_{\eta\eta}\right) = 0\end{aligned} \tag{5.19}$$

and

$$\begin{aligned}&\frac{ma\beta g_e\,(1-\eta^2)}{\nu(2-\eta^2)^{1/2}}T - \mathrm{v}_\theta\frac{m}{a\lambda\eta}\left(\frac{(2g_\lambda + \lambda g_{\lambda\lambda})}{(2-\eta^2)} + \frac{1}{4\lambda}\left(g_{\eta\eta} - \frac{g_\eta}{\eta}\right)\right) \\ &+ w_r\frac{1}{(2-\eta^2)^{1/2}}\left(\frac{2g}{\lambda} + \frac{4(1-\eta^2)}{\lambda} - \lambda g_{\lambda\lambda}\right) + \frac{\partial w_r}{\partial \lambda}\left(\frac{2(1-\eta^2)}{(2-\eta^2)^{1/2}}\right) + \frac{\partial w_r}{\partial \eta}\left(\frac{\eta(2-\eta^2)^{1/2}}{\lambda}\right) \\ &+ w_\theta\frac{1}{(2-\eta^2)}\left(\frac{(2\eta^4 - 4\eta^2 + 1)}{\lambda\eta} - \frac{m^2}{\lambda\eta} - \frac{(2-\eta^2)}{2}g_{\lambda\eta} + \frac{(1-\eta^2)}{\lambda\eta}\left(g + \lambda g_\lambda\right)\right) + \frac{\partial w_\theta}{\partial \lambda}\left(\frac{-g_\eta}{\eta} + 2\eta\right) \\ &+ \frac{\partial^2 w_\theta}{\partial \lambda^2}(\lambda\eta) + \frac{\partial w_\theta}{\partial \eta}\frac{1}{4\lambda}\left(6-7\eta^2 + 2\left(g + \lambda g_\lambda\right)\right) + \frac{\partial^2 w_\theta}{\partial \eta^2}\left(\frac{\eta(2-\eta^2)}{4\lambda}\right) = 0.\end{aligned} \tag{5.20}$$

As equation (5.16) can be used to solve for $w_\phi$ if required, the equations used to solve for **w** are (5.19), (5.20) and (5.16) can be used to recover the values for $w_\phi$ if needed. Taking the curl of the Navier Stokes equation to obtain equation (5.1) eliminates the pressure from the problem. This can be easily recovered if required from the $\phi$-component of the original Navier Stokes equation. This means that we have one more equation than is necessary and so the equation for the phi component (5.14) can now be discarded.

The perturbation equation for the temperature is given by

$$\frac{\partial T}{\partial t} + \mathbf{v}.\nabla T_0 + \mathbf{u}.\nabla T - \kappa\nabla^2 T = 0. \qquad (5.21)$$

Since we are looking at the case of marginal stability, the first term in the above equation is zero. The stationary temperature distribution, found in Chapter 4, can be written

$$T_0 = \frac{T_m\, a}{\lambda}\, t\,(\lambda,\eta),$$

with the perturbation given by

$$T = T_m\, \tilde{T}\,(\lambda,\eta)\; e^{(im\varphi + \sigma t)}.$$

The forms of these variables, and those for **v** and **u**, are substituted into equation (5.21) and the tildes dropped to give for each of its terms the following expressions

$$\mathbf{v}.\nabla T_0 = \mathrm{v}_{\mathrm{r}} T_m \left( \frac{t_\lambda}{a^2\lambda} - \frac{t}{a^2\lambda^2} \right) + \mathrm{v}_\theta \frac{(2-\eta^2)^{1/2}}{2a^2\lambda^2}\, T_m\, t_\eta,$$

$$\mathbf{u}.\nabla T = \frac{T_m \nu g_\eta}{2a^2\lambda\eta}\frac{\partial T}{\partial\lambda} - \frac{T_m \nu(g+\lambda g_\lambda)}{2a^2\lambda^2\eta}\frac{\partial T}{\partial\eta},$$

$$\nabla^2 T = \frac{T_m}{a^2}\left[ \frac{\partial^2 T}{\partial\lambda^2} + \frac{2}{\lambda}\frac{\partial T}{\partial\lambda} + \frac{(2-3\eta^2)}{4\lambda^2\eta}\frac{\partial T}{\partial\eta} + \frac{(2-\eta^2)}{4\lambda^2}\frac{\partial^2 T}{\partial\eta^2} - \frac{m^2}{\lambda^2\eta^2(2-\eta^2)}\, T \right].$$

Collecting the above terms together and multiplying by $2a^2\lambda/T_m$ gives as the final equation:

$$2\mathrm{v}_{\mathrm{r}}\left(t_\lambda - \frac{t}{\lambda}\right) + \mathrm{v}_\theta \frac{(2-\eta^2)^{1/2}}{\lambda}\, t_\eta + \frac{\nu g_\eta}{\eta}\frac{\partial T}{\partial\lambda} - \frac{\nu(g+\lambda g_\lambda)}{\lambda\eta}\frac{\partial T}{\partial\eta}$$
$$-\,\kappa\left( 2\lambda\frac{\partial^2 T}{\partial\lambda^2} + 4\frac{\partial T}{\partial\lambda} + \frac{(2-3\eta^2)}{2\lambda\eta}\frac{\partial T}{\partial\eta} + \frac{(2-\eta^2)}{2\lambda}\frac{\partial^2 T}{\partial\eta^2} - \frac{2m^2}{\lambda\eta^2(2-\eta^2)}\, T \right) = 0. \qquad (5.22)$$

The final equation used to solve for the perturbation comes from the definition of **w**,

$$\begin{aligned}\mathbf{w} = \nabla\times\mathbf{v} = \hat{\mathbf{r}}\frac{1}{a}&\left(\frac{(2-\eta^2)^{1/2}}{2\lambda}\frac{\partial \mathrm{v}_\varphi}{\partial\eta} + \frac{(1-\eta^2)}{\lambda\eta(2-\eta^2)^{1/2}}\mathrm{v}_\varphi - \frac{im}{\lambda\eta(2-\eta^2)^{1/2}}\mathrm{v}_\theta\right)\\ +\hat{\theta}\frac{1}{a}&\left(\frac{im}{\lambda\eta(2-\eta^2)^{1/2}}\mathrm{v}_\mathrm{r} - \frac{\mathrm{v}_\varphi}{\lambda} - \frac{\partial \mathrm{v}_\varphi}{\partial\lambda}\right)\\ +\hat{\Phi}\frac{1}{a}&\left(\frac{\mathrm{v}_\theta}{\lambda} + \frac{\partial \mathrm{v}_\theta}{\partial\lambda} - \frac{(2-\eta^2)^{1/2}}{2\lambda}\frac{\partial \mathrm{v}_\mathrm{r}}{\partial\eta}\right).\end{aligned} \tag{5.23}$$

Since the flow is considered to be incompressible, div **v** = 0. Hence $\mathrm{v}_\phi$ and its derivatives can be eliminated in the same way as $\mathrm{w}_\phi$ and its derivatives were removed following (5.16).

The r component of (5.23) becomes

$$\begin{aligned}w_r\, ma = \mathrm{v}_\mathrm{r}&\left(\frac{4(1-\eta^2)}{\lambda}\right) + \frac{\partial \mathrm{v}_\mathrm{r}}{\partial\lambda}(2(1-\eta^2)) + \frac{\partial \mathrm{v}_\mathrm{r}}{\partial\eta}\left(\frac{\eta(2-\eta^2)}{\lambda}\right) + \frac{\partial^2 \mathrm{v}_\mathrm{r}}{\partial\lambda\partial\eta}\left(\frac{\eta(2-\eta^2)}{2}\right)\\ + \mathrm{v}_\theta&\left(\frac{(1-4\eta^2+2\eta^4-m^2)}{\lambda\eta(2-\eta^2)^{1/2}}\right) + \frac{\partial \mathrm{v}_\theta}{\partial\eta}\left(\frac{(2-\eta^2)^{1/2}(6-7\eta^2)}{4\lambda}\right) + \frac{\partial^2 \mathrm{v}_\theta}{\partial\eta^2}\left(\frac{\eta(2-\eta^2)^{3/2}}{4\lambda}\right),\end{aligned} \tag{5.24}$$

and the theta component leads to

$$\begin{aligned}-w_\theta\, ma = \mathrm{v}_\mathrm{r}&\frac{(2-\eta^2)^{1/2}}{\lambda}\left(\frac{-m^2}{\eta(2-\eta^2)} + 2\eta\right) + \frac{\partial \mathrm{v}_\mathrm{r}}{\partial\lambda}(4\eta(2-\eta^2)^{1/2}) + \frac{\partial^2 \mathrm{v}_\mathrm{r}}{\partial\lambda^2}(\lambda\eta(2-\eta^2)^{1/2})\\ + \mathrm{v}_\theta&\left(\frac{(1-\eta^2)}{\lambda}\right) + \frac{\partial \mathrm{v}_\theta}{\partial\lambda}(1-\eta^2) + \frac{\partial \mathrm{v}_\theta}{\partial\eta}\left(\frac{\eta(2-\eta^2)}{2\lambda}\right) + \frac{\partial^2 \mathrm{v}_\theta}{\partial\lambda\partial\eta}\left(\frac{\eta(2-\eta^2)}{2}\right).\end{aligned} \tag{5.25}$$

The values for $\mathrm{v}_\phi$ can be recovered from div **v** = 0 (c.f. $\mathrm{w}_\phi$ ), so again only these two equations have to be solved.

## 5.3.2: The boundary conditions

The following conditions come from considering the physical situation:

$\mathrm{v}_\mathrm{r} = \mathrm{v}_\theta = \mathrm{v}_\phi = 0$ on $\lambda = 0$ and 1, (5.26)

$\mathrm{T} = 0$ on $\lambda = 0$ and 1, (5.27)

$\mathrm{v}_\theta = 0$ on $\eta = 0$ and 1, (5.28)

$$\frac{\partial T}{\partial \theta} = 0 \Rightarrow \frac{\partial T}{\partial \eta} = 0 \qquad \text{on } \eta = 0 \text{ and } 1. \qquad (5.29)$$

Conditions (5.26) comes from requiring no fluid motion on the outer hemisphere, and allowing no perturbations from the prescribed flow at the origin.

Equation (5.27) results from fixing the outer boundary to be at the melting temperature and allowing no perturbation from the prescribed temperature at the origin.

The velocity condition (5.28) arises from allowing no motion across the axis nor across the top surface, requiring the latter to be flat.

In addition condition (5.29) comes from requiring no heat flux across the axis and none across the top surface.

Considering the stresses on the top surface, the following conditions are obtained:

$$\begin{aligned}\sigma_{r\theta} &= \frac{\rho\nu}{a}\left(\frac{1}{\lambda}\frac{\partial \mathrm{v}_r}{\partial \theta} - \frac{\mathrm{v}_\theta}{\lambda} + \frac{\partial \mathrm{v}_\theta}{\partial \lambda}\right) \\ &= \frac{\rho\nu}{2a\lambda}\frac{\partial \mathrm{v}_r}{\partial \eta} = \frac{1}{a}\frac{\partial \gamma}{\partial T}\frac{\partial T}{\partial \lambda}, \end{aligned} \qquad (5.30)$$

and

$$\begin{aligned}\sigma_{\varphi\theta} &= \frac{\rho\nu}{a\lambda}\left(\frac{(2-\eta^2)^{1/2}}{2}\frac{\partial \mathrm{v}_\varphi}{\partial \eta} - \frac{(1-\eta^2)}{\eta(2-\eta^2)^{1/2}}\mathrm{v}_\varphi + \frac{im}{\eta(2-\eta^2)^{1/2}}\mathrm{v}_\theta\right) \\ &= \frac{\rho\nu}{2a\lambda}\frac{\partial \mathrm{v}_\varphi}{\partial \eta} = \rho\nu w_r = 0. \end{aligned} \qquad (5.31)$$

Considering the equations (5.19), (5.20), (5.22), (5.24) and (5.25) and requiring that none of the vorticity or velocity components, or the temperature, become infinite on the boundaries gives some additional boundary conditions that must be satisfied. Only those conditions that are required to solve the equations are listed below, additional derivatives of the perturbations can also be shown to be zero on the boundaries. Use is made of L'Hopital's rule where appropriate.

Firstly consider the axis, $\eta = 0$.

From equation (5.23) the following is found:

$$\mathbf{w} = \hat{\mathbf{r}}\,\frac{1}{2^{1/2}a\lambda}\left(\frac{\partial \mathrm{v}_\varphi}{\partial \eta} + \frac{\mathrm{v}_\varphi}{\eta} - im\,\frac{\partial \mathrm{v}_\theta}{\partial \eta}\right)$$

$$+\,\hat{\theta}\,\frac{1}{a}\left(\frac{im}{2^{1/2}\lambda}\frac{v_r}{\eta} - \frac{\mathrm{v}_\varphi}{\lambda} - \frac{\partial \mathrm{v}_\varphi}{\partial \lambda}\right) + \hat{\Phi}\left(-\frac{1}{2^{1/2}\lambda}\frac{\partial \mathrm{v}_r}{\partial \eta}\right),$$

$$\Rightarrow \mathrm{v}_\varphi = \mathrm{v}_r = 0 \text{ on } \eta = 0, \text{ otherwise } w_r\,,\, w_\theta \to \infty. \tag{5.32}$$

This result then also implies that

$$\mathrm{w}_\theta = 0. \tag{5.33}$$

From equation (5.19) we obtain

$$-\,w_r\,\frac{m^2}{2\eta} + \frac{1}{2}\frac{\partial w_r}{\partial \eta} = 0,$$

$$\Rightarrow w_r = 0. \tag{5.34}$$

From the temperature equation (5.22) we obtain

$$T\,\frac{\kappa m^2}{\lambda \eta^2} + \frac{\partial T}{\partial \lambda}\,(\nu g_{\eta\eta} - 4\kappa) + \frac{\partial^2 T}{\partial \lambda^2}\,(-\,2\kappa\lambda) + \frac{\partial^2 T}{\partial \eta^2}\left(\frac{-\,2\kappa}{\lambda}\right) = 0,$$

$$\Rightarrow T = 0. \tag{5.35}$$

Now let us look at the origin, $\lambda$=0.

Firstly, from equation (5.20) we obtain

$$-\,\frac{\partial \mathrm{v}_\theta}{\partial \lambda}\,\frac{m}{a\eta}\left(\frac{2g_\lambda}{(2-\eta^2)} + \frac{1}{4\lambda}\left(g_{\eta\eta} - \frac{g_\eta}{\eta}\right)\right) + w_r\left(\frac{2g_\lambda}{(2-\eta^2)^{1/2}}\right) + \frac{\partial w_r}{\partial \lambda}\left(\frac{g}{(2-\eta^2)^{1/2}}\right) + \frac{\partial^2 w_r}{\partial \lambda \partial \eta}\left(\frac{-\,\eta(2-\eta^2)^{1/2}}{2}\right)$$

$$+\,w_\theta\left(\frac{m^2}{\lambda\eta(2-\eta^2)} - \frac{g_{\lambda\eta}}{2}\right) + \frac{\partial w_\theta}{\partial \lambda}\left(\frac{-\,g_\eta}{\eta} - 2\eta\right) + \frac{w_\varphi}{\lambda}\,\frac{im}{(2-\eta^2)}\left(\frac{(1-\eta^2)}{\eta} - \frac{g}{\eta}\right) + \frac{\partial w_\varphi}{\partial \eta}\left(\frac{im}{2\lambda}\right) = 0,$$

$$\Rightarrow \frac{\partial \mathrm{v}_\theta}{\partial \lambda} = w_\theta = w_\varphi = 0. \tag{5.36}$$

From the identity div **w** = 0, (5.15), it follows that

$$\frac{2w_r}{\lambda}+\frac{\partial w_r}{\partial\lambda}+(2-\eta^2)\frac{\partial^2 w_\theta}{\partial\lambda\partial\eta}+\frac{(1-\eta^2)}{\eta(2-\eta^2)}\frac{\partial w_\theta}{\partial\lambda}+\frac{im}{\eta(2-\eta^2)^{1/2}}\frac{\partial w_\varphi}{\partial\lambda}=0,$$

$$\Rightarrow\ w_r=0. \tag{5.37}$$

Finally, looking at the outer surface of the hemisphere, $\lambda = 1$, equation (5.23) implies that

$$w_r=0. \tag{5.38}$$

Thus, the complete set of boundary conditions for the perturbation are

On $\eta = 0$ (the axis):

$$\begin{gathered} v_r = 0,\ v_\theta = 0,\ v_\phi = 0, \\ w_r = 0,\ w_\theta = 0,\ w_\phi = 0, \\ T = 0; \end{gathered} \tag{5.39}$$

on $\eta = 1$ (the top surface):

$$\begin{gathered} v_\theta = 0, \\ \frac{\rho\nu}{2a\lambda}\frac{\partial v_\varphi}{\partial\eta} = \rho\nu w_r = 0; \end{gathered} \tag{5.40}$$

on $\lambda = 0$ (the origin):

$$\begin{gathered} v_r = 0,\ v_\theta = 0,\ v_\phi = 0, \\ w_r = 0,\ w_\theta = 0,\ w_\phi = 0, \\ T = 0; \end{gathered} \tag{5.41}$$

on $\lambda = 1$ (the outer hemisphere):

$$\begin{gathered} v_r = 0,\ v_\theta = 0,\ v_\phi = 0, \\ T = 0. \end{gathered} \tag{5.42}$$

This list obviously does not contain a sufficient number of conditions for all the variables on all the boundaries, and so equations (5.20) and (5.22) have to be solved on particular boundaries.

Equation (5.20) is solved on $\eta = 1$ where, making use of boundary conditions (5.40), it becomes

$$
\frac{\partial w_r}{\partial \eta}\left(\frac{1}{\lambda}\right)+w_\theta\left(\frac{-m^2}{\lambda}-\frac{g_{\lambda\eta}}{2}-\frac{1}{\lambda}\right)+\frac{\partial w_\theta}{\partial \lambda}(2-g_\eta)
+\frac{\partial^2 w_\theta}{\partial \lambda^2}\lambda+\frac{\partial w_\theta}{\partial \eta}\left(\frac{-1}{4\lambda}\right)+\frac{\partial^2 w_\theta}{\partial \eta^2}\left(\frac{1}{4\lambda}\right)=0. \tag{5.43}
$$

In a similar way on $\lambda=1$, using boundary conditions (5.42), equation (5.20) leads to

$$
\frac{\partial w_r}{\partial \lambda}\left(\frac{2(1-\eta^2)}{(2-\eta^2)^{½}}\right)+w_\theta\frac{1}{(2-\eta^2)}\left(\frac{(2\eta^4-4\eta^2+1)}{\eta}-\frac{m^2}{\eta}\right)+\frac{\partial w_\theta}{\partial \lambda}2\eta+\frac{\partial^2 w_\theta}{\partial \lambda^2}\eta
+\frac{\partial w_\theta}{\partial \eta}\left(\frac{(6-7\eta^2)}{4}\right)+\frac{\partial^2 w_\theta}{\partial \eta^2}\left(\frac{\eta(2-\eta^2)}{4}\right)=0. \tag{5.44}
$$

The temperature equation (5.22) is solved on $\eta = 1$ where, making use of boundary conditions (5.40), it becomes

$$
2\mathrm{v}_\mathrm{r}\left(\frac{t}{\lambda}-t_\lambda\right)-T\left(\frac{2\kappa m^2}{\lambda}\right)-\frac{\partial T}{\partial \lambda}\left(\nu g_\eta-4\kappa\right)+\frac{\partial^2 T}{\partial \lambda^2}(2\lambda\kappa)+\frac{\partial^2 T}{\partial \eta^2}\left(\frac{\kappa}{2\lambda}\right)=0 \tag{5.45}
$$

# 5.4: Method of solution

The problem can now be stated as finding the locus of the parameter values $(J,\frac{\partial\gamma}{\partial T})$ where there exists a non-zero solution to the equations (5.19), (5.20), (5.22), (5.24), (5.25) subject to the boundary conditions (5.39),(5.40), (5.41) and (5.42). Due to the fact that the perturbation cannot be written in an analytic form, this is a far from trivial problem. The existence of a solution has to be investigated numerically, since in this problem the original solution whose stability is being checked is a numerical solution in $(\lambda,\eta)$. The method chosen was to write the problem in finite difference form as a matrix equation $\mathbf{Ax}= \mathbf{0}$, where $\mathbf{x}$ is a vector of the values of the perturbation functions on an 11 by 11 equally spaced grid of points in $(\lambda,\eta)$ space, excepting those points where the value of the variables are known from the boundary conditions. $\mathbf{A}$ is a matrix containing the coefficients in the finite difference equations.

For a given value of $\frac{\partial\gamma}{\partial T}$ the current value, J, is increased from zero in small steps. For each value of J the solution to the problem in Chapter 4 is calculated, and this is then used to specify the elements in the matrix $\mathbf{A}$, whose determinant is then calculated using a NAG routine. When a change of sign of the determinant occurs as J increases, this means that the determinant has gone through zero, and hence a non-trivial solution to $\mathbf{Ax} = \mathbf{0}$ was possible in this range, ie. a non-zero solution to the perturbation equations is possible. The prescribed values of J and $\frac{\partial\gamma}{\partial T}$ provide a point on the marginal stability curve.

This method was chosen for its simplicity and speed. A major disadvantage, however, is the amount of memory storage space required for the matrix $\mathbf{A}$. Since this space grows with the square of the total number of grid points used, and the time taken to calculate the determinant with the cube, it proved impossible to use significantly more grid-points than the chosen 11 by 11 grid.

In solving the system of equations, (5.19), (5.20), (5.22), (5.24) and (5.25) are converted to finite difference form using the method introduced in Chapter 4. That is, in the equation for which a variable is solved, its first derivatives are approximated using the QUI method in the interior of the region, and using one-sided differences one point in from the boundary. The second derivatives are approximated using central differences. All derivatives of other variables in an equation are approximated using central differences.

Where a differential equation for a given variable needs to be solved on a boundary, the first derivatives of this variable are approximated using one-sided differences. The first derivatives of other variables are approximated using central differences, provided this would not require a point outside the region, otherwise one-sided differences are used. The finite difference forms of the equations in most of the region are not presented, since their derivation is time consuming and follows the method shown in Chapter 4. Special consideration has to be given for some second derivatives on the boundaries, as set out below.

First consider equation (5.43), which is solved along the boundary $\eta=1$, except for the end points $\lambda=0$ and 1. To avoid the need for points outside the boundary, the $g_{\lambda\eta}$ term is evaluated on $\eta=1$ by considering a central $\lambda$ derivative of a one-sided $\eta$ derivative, the appropriate term becoming

$$-w_\theta\left(\frac{m^2}{\lambda}+\frac{g_{\eta\lambda}}{2}+\frac{1}{\lambda}\right):$$

$$-w_\theta\left(\frac{m^2+1}{\lambda_i}-\left(\frac{g_{i+1,j-1}-g_{i-1,j-1}}{4(\Delta\lambda)(\Delta\eta)}\right)\right),$$

and second derivative $\frac{\partial^2 w_\theta}{\partial\eta^2}$ term is approximated using a first order one-sided method to give

$$\frac{\partial^2 w_\theta}{\partial\eta^2}\left(\frac{1}{4\lambda}\right):$$

$$\left(\frac{w_\theta-2w_{\theta,j-1}+w_{\theta,j-2}}{(\Delta\eta)^2}\right)\frac{1}{4\lambda_i}\,.$$

## 5.5: Results and discussion

The values of the determinants calculated for each given value of $\frac{\partial\gamma}{\partial T}$ varied smoothly as the current was increased. For the mode m=1 figures 5.24 and 5.25 show the values of the current at which, for a given $\frac{\partial\gamma}{\partial T}$, the determinant went through zero, i.e. the figures display the marginal stability curves. A few points were calculated with m=2 for both positive and negative $\frac{\partial\gamma}{\partial T}$, but the current values obtained were in all cases considerably above those for the case m=1, and hence the m=1 instability mode is likely to manifest first.

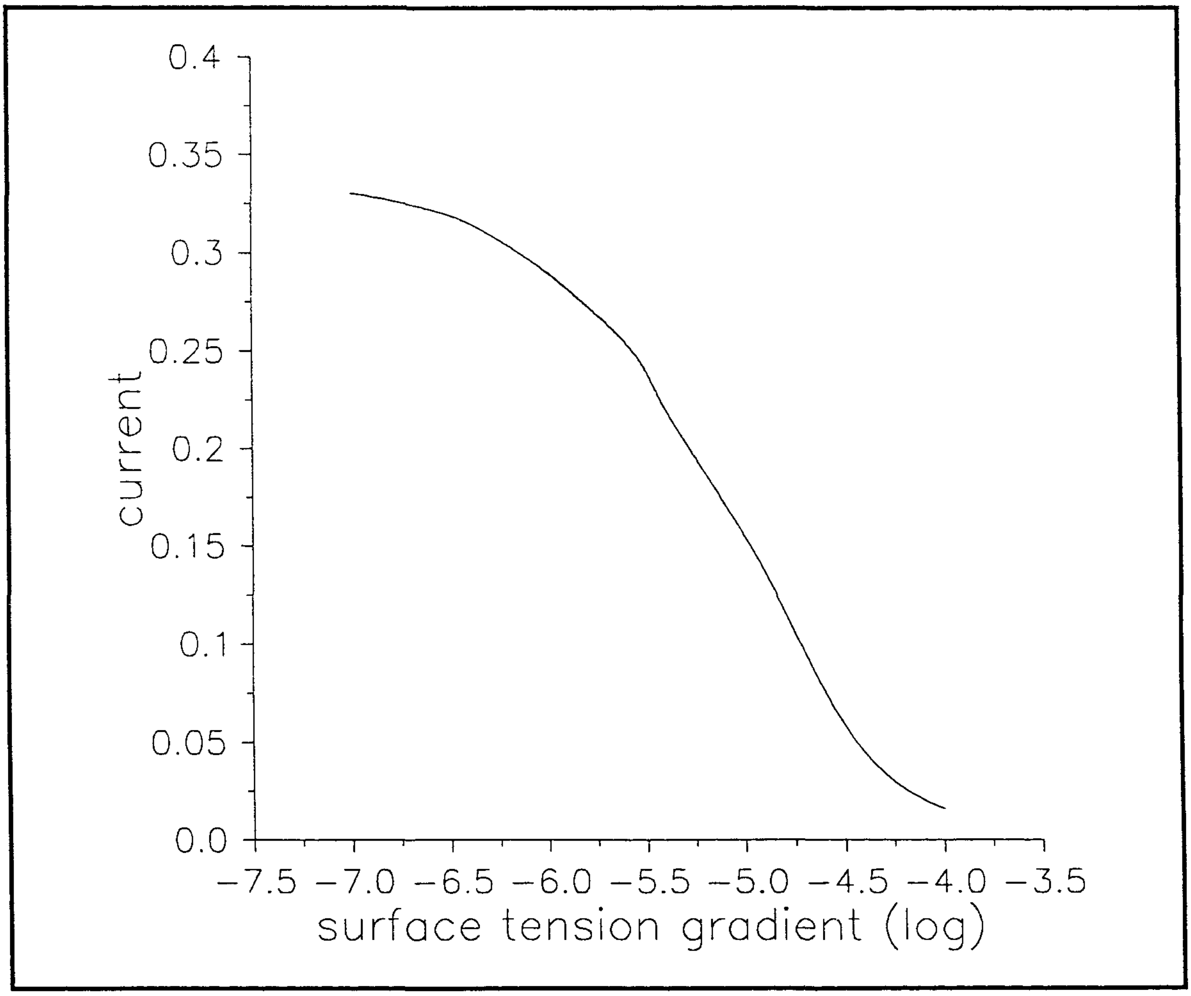

**Figure 5.24** - marginal stability curve for $\frac{\partial\gamma}{\partial T}$ positive

Comparing figure 5.24 with the earlier figure 4.13 it can be seen that the loss of stability for a prescribed $\frac{\partial \gamma}{\partial T}$ occurs at a current value much lower than that at which it becomes impossible to obtain a converged numerical solution.

In an analogous way comparing figure 5.25 with 4.22 also reveals instability at current values at which numerical solutions exist. In addition, it is observed that the peak in figure 5.25 corresponds with the peak in the current at which the solution breaks down, displayed in figure 4.22. This suggests that the drop in current on the left-hand side of figure 5.25 arises from the rapid increase in velocities caused by the increasingly large surface tension forces.

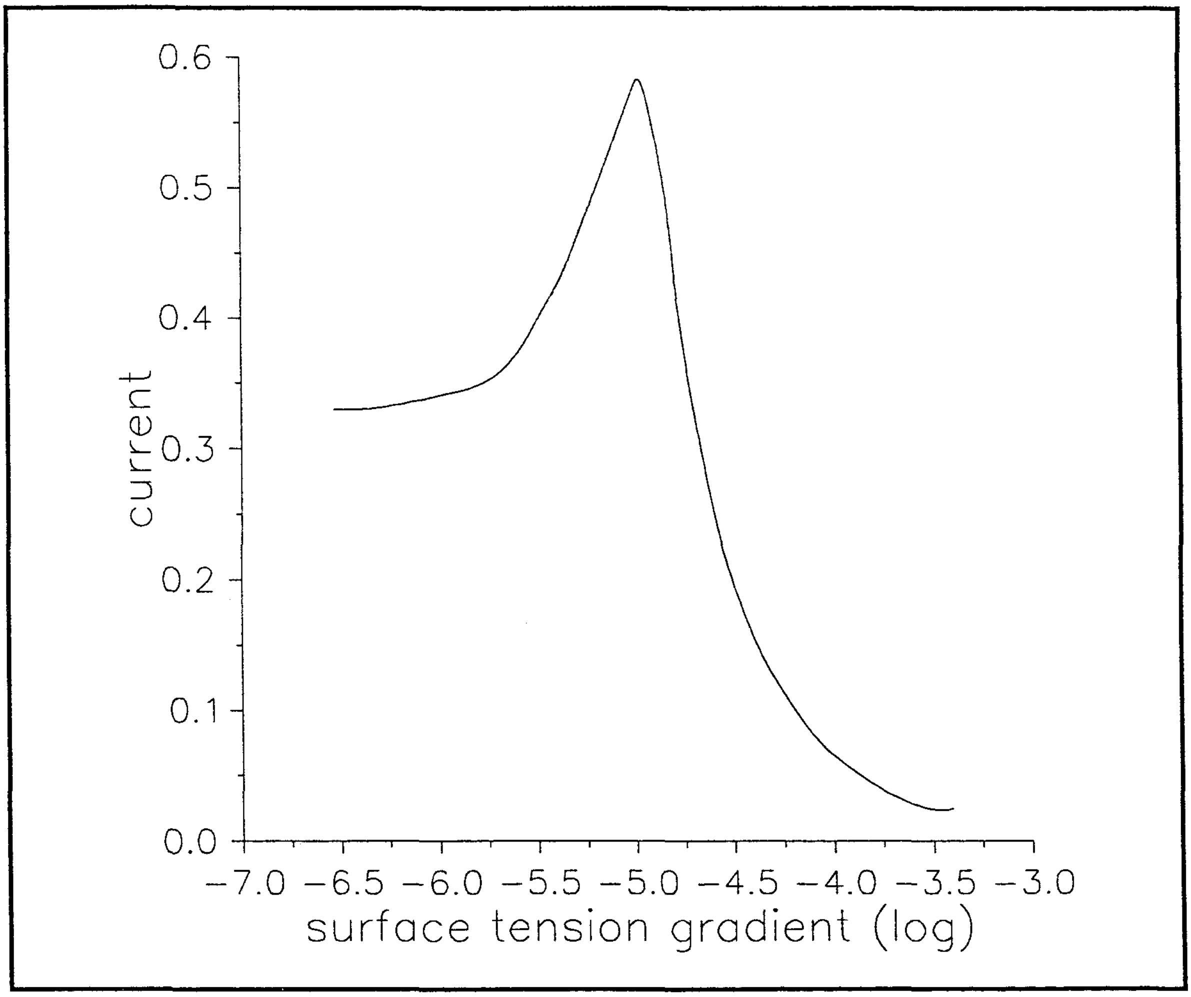

**Figure 5.25** - marginal stability curve for $\frac{\partial \gamma}{\partial T}$ negative

For a few particular values of $\frac{\partial\gamma}{\partial T}$ the eigen-problem **Ax=σx** is solved in the region of the loss of stability. In each case one of the eigenvalues was seen to pass through zero. The associated eigenvector then contains the form for the perturbation which will be manifested at the loss of stability. Figures 5.26 to 5.30 contain plots of the maximum values of the poloidal velocity and azimuthal velocity obtained from these eigenvectors. It should be stressed that, due to the limited number of grid points used in calculating the perturbations, these plots do not give more than a general indication of the structure of the flow and the irregularities in the presented curves are a result of this. In all figures the velocities have been rescaled by the maximum poloidal velocity calculated for that case. The azimuthal velocities are shown in the right-hand plot on each figure.

Figure 5.26 displays the results for $\frac{\partial\gamma}{\partial T}=-10^{-4}\mathrm{Nm^{-1}K^{-1}}$ and J=0.05A. In this case the basic stationary flow is purely surface tension driven, with a strong outward loop at the top of the hemisphere and a much weaker counter rotating loop at the bottom.

When $\frac{\partial\gamma}{\partial T}=-10^{-5}\mathrm{Nm^{-1}K^{-1}}$ and J=0.6A (the parameter values for figure 5.27) the basic flow now contains a single, strong, surface tension driven loop.

Figures 5.28 and 5.29 refer respectively to the cases $\frac{\partial\gamma}{\partial T}=-10^{-6}\mathrm{Nm^{-1}K^{-1}}$ and J=0.3A, when the basic flow is a fairly slow single loop driven by the surface tension and buoyancy forces, and $\frac{\partial\gamma}{\partial T}=10^{-7}\mathrm{Nm^{-1}K^{-1}}$ and J=0.35A, for which the stationary flow contains two loops, one driven by surface tension and electromagnetic forces near the origin and one driven by buoyancy near the outer hemisphere.

Finally, figure 5.30 displays the results when $\frac{\partial\gamma}{\partial T}=10^{-5}\mathrm{Nm^{-1}K^{-1}}$ and J=0.13A, when the stationary flow is dominated by surface tension forces, and a single inward loop is observed.

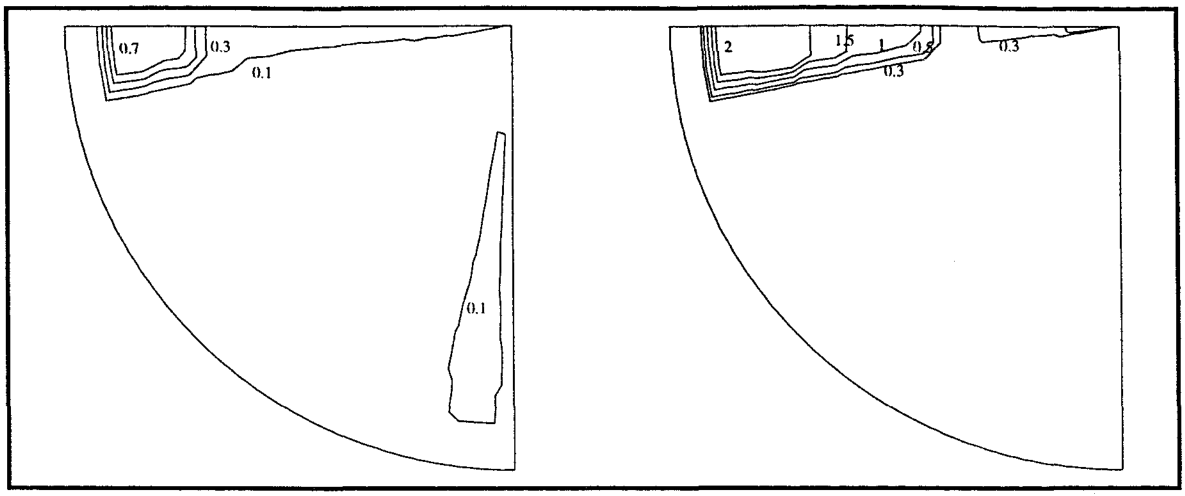

**Figure 5.26** - poloidal and azimuthal velocities at loss of stability for $\frac{\partial\gamma}{\partial T}=-10^{-4}\mathrm{Nm^{-1}K^{-1}}$

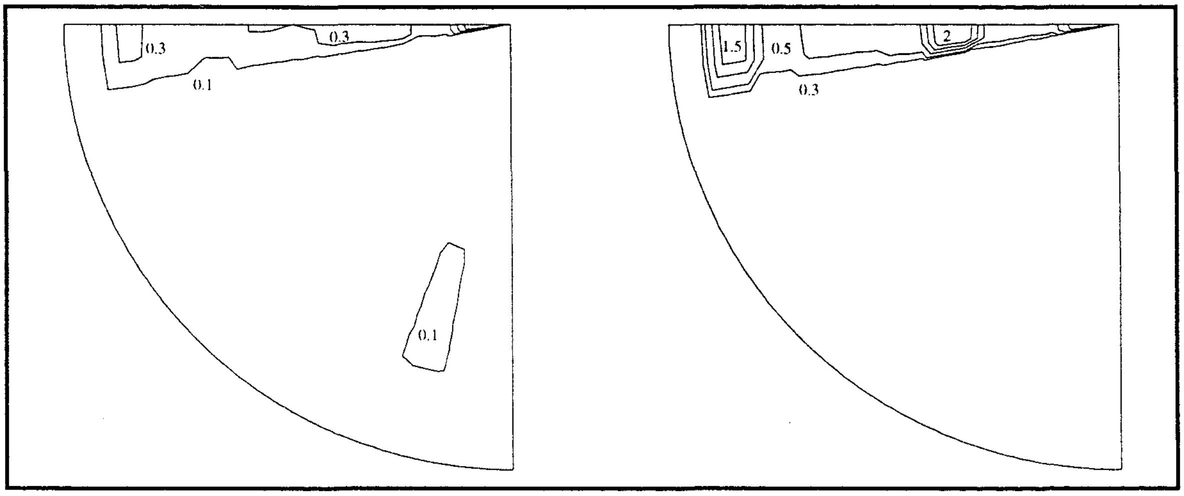

**Figure 5.27** - poloidal and azimuthal velocities at loss of stability for $\frac{\partial\gamma}{\partial T}=-10^{-5}\mathrm{Nm^{-1}K^{-1}}$

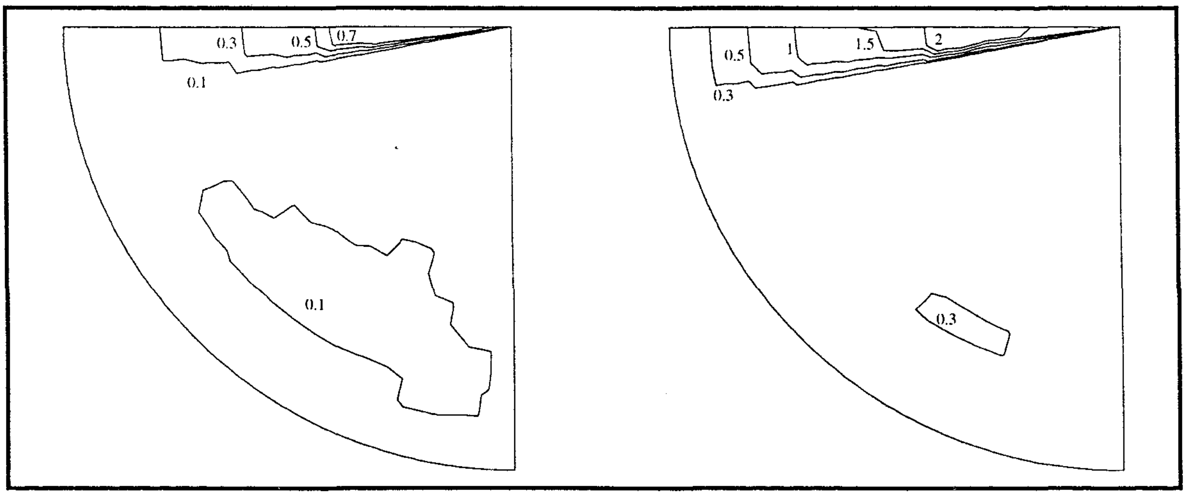

**Figure 5.28** - poloidal and azimuthal velocities at loss of stability for $\frac{\partial\gamma}{\partial T}=-10^{-6}\mathrm{Nm^{-1}K^{-1}}$

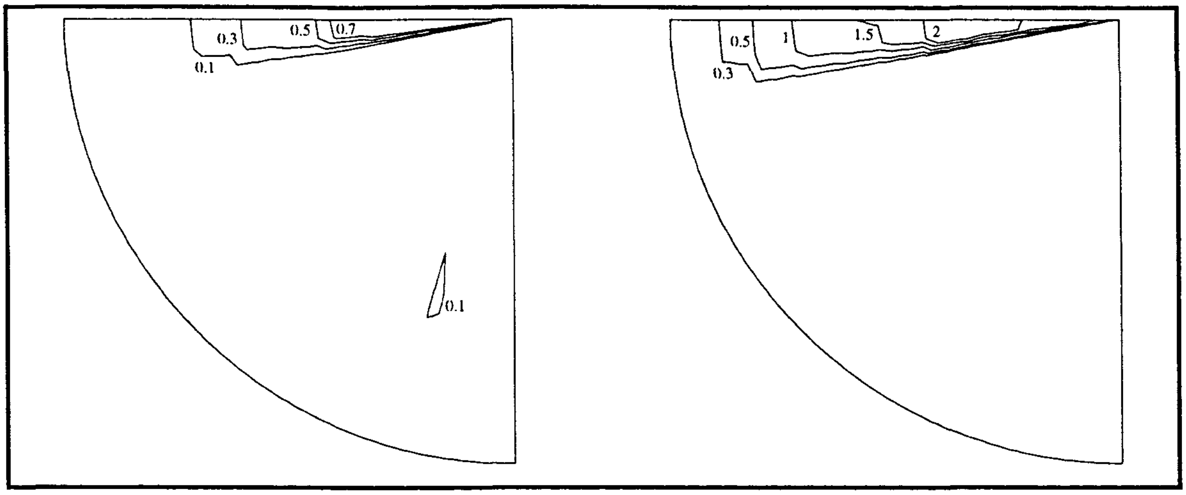

**Figure 5.29** - poloidal and azimuthal velocities at loss of stability for $\frac{\partial\gamma}{\partial T}=10^{-5}\mathrm{Nm^{-1}K^{-1}}$

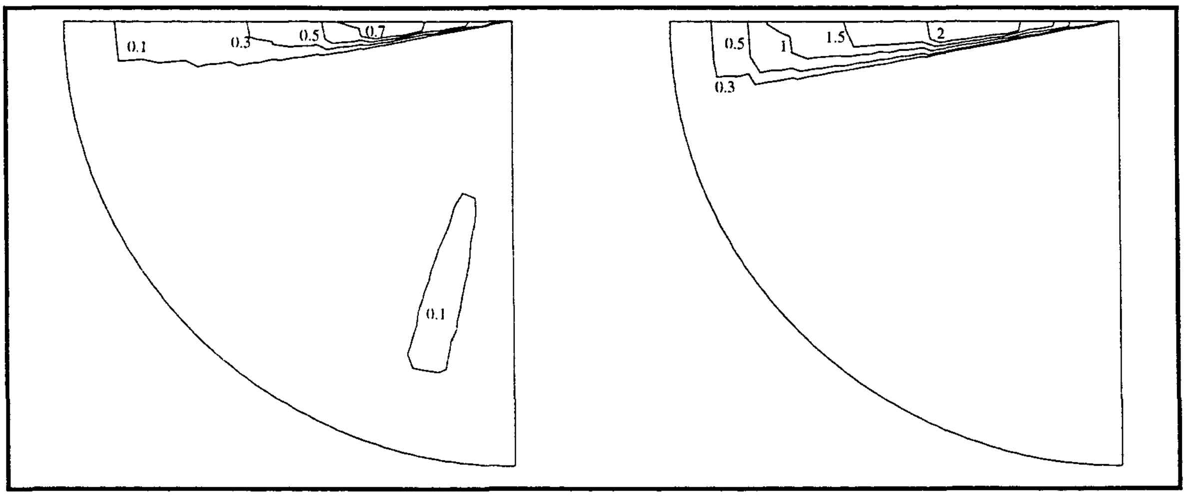

**Figure 5.30** - poloidal and azimuthal velocities at loss of stability for $\frac{\partial\gamma}{\partial T}=10^{-7}\mathrm{Nm^{-1}K^{-1}}$

There are two common features in figures 5.26 to 5.30. Firstly the azimuthal velocity components are larger than the poloidal perturbation components, which indicates that at the point at which stability is lost the fluid is likely to start to rotate with a significant velocity. Secondly, the maximum velocities occur at the top surface of the weld pool, although considering that the perturbation velocity is fixed at zero on the other boundaries this is not surprising. It is also observed that the poloidal velocity reaches a significant size near the axis and towards the outer hemisphere, with, in figure 5.28, this region extending up the hemisphere.

From figures 5.26 and 5.27, where the basic flow is strongly outwards, it can be seen that the maximum velocities occur at the edge of the hemisphere, where the fluid has to turn a sharp corner and go down.

In the other three figures the basic flow is either moving slowly outward (figure 5.28), or moving inward (figures 5.29 and 5.30), and the maximum velocities are seen to occur near the origin.

# Chapter 6: Concluding remarks

In this thesis we have presented models for the flow of fluid and heat in a weld pool due to electromagnetic, surface tension and buoyancy forces, and have investigated the possibility of the poloidal fluid flow undergoing a bifurcation to a rotating flow pattern.

In Chapter 2 the flow in a semi-infinite region of thermally and electrically conducting fluid caused by coincident point sources of heat and current, and including electromagnetic forces in the body of the fluid and a surface tension force along the top surface, was investigated, and similarity solutions for the stream function and temperature were obtained. The surface tension force proved to be of great importance in determining the fluid flow, with the flow pattern being dominated by it when $\left|\frac{\partial \gamma}{\partial T}\right| > 10^{-5} \mathrm{Nm}^{-1} \mathrm{K}^{-1}$ for most values of the applied current. The breakdown of the solution with the appearance of an infinite velocity down the axis of symmetry, which Sozou [ 97 ] had observed for his similar model including just the electromagnetic forces, was also observed. However, it was shown in Chapter 2 that the breakdown current can be changed by over an order of magnitude through the addition of the surface tension forces with $\left|\frac{\partial \gamma}{\partial T}\right| > 10^{-5} \mathrm{Nm}^{-1} \mathrm{K}^{-1}$. For the case $\frac{\partial \gamma}{\partial T} < 0$, solutions without singularities can be found up to realistic welding currents. Since the value of $\left|\frac{\partial \gamma}{\partial T}\right|$ for molten steel can be $O(10^{-4})$ and either positive or negative, the particular value of $\frac{\partial \gamma}{\partial T}$ appropriate for a given type of steel greatly affects the surface tension force and is very important, therefore, in determining the fluid flow.

In Chapter 3 the effect on the solutions obtained in Chapter 2 caused by adding a small azimuthal component to the electromagnetic force was studied. It was shown that below the breakdown current for a given $\frac{\partial\gamma}{\partial T}$ the azimuthal rotation produced by this force was very small and did not appreciably affect the flow pattern. On approaching the breakdown current the azimuthal velocity started to increase rapidly, and the fluid started to spin. For $\left|\frac{\partial\gamma}{\partial T}\right|$ less than approximately $2*10^{-6}\mathrm{Nm}^{-1}\mathrm{K}^{-1}$ the increase in azimuthal velocity was found to produce a centrifugal force which slowed down the poloidal flow and prevented the fluid velocity becoming infinite down the axis. For $\left|\frac{\partial\gamma}{\partial T}\right|$ greater than approximately $2*10^{-6}\mathrm{Nm}^{-1}\mathrm{K}^{-1}$ it proved impossible to obtain solutions above the breakdown values of the current, although it was not possible to prove whether this was due to the azimuthal velocity not being able to grow sufficiently rapidly or due to the chosen numerical method being unable to converge because of the large velocity gradients present. Without some component of force in the azimuthal direction it is not possible to obtain a spontaneous generation of swirl using a similarity solution, as shown in the Appendix.

In Chapter 4 a model for a finite weld pool was presented, in which the flow of fluid and heat in a hemisphere was investigated under the influence of electromagnetic, surface tension and buoyancy forces arising from coincident point sources of heat and current. The addition of the buoyancy force was shown to produce significant differences in the flow pattern when values of the applied current and $\left|\frac{\partial\gamma}{\partial T}\right|$ are small. Since the similarity solution of Chapter 2 was being used to obtain one of the boundary conditions for this model it is not surprising that, for most values of $\left|\frac{\partial\gamma}{\partial T}\right|$, the solutions broke down due to a rapid increase in fluid velocity down the axis of symmetry. For $\frac{\partial\gamma}{\partial T}<-10^{-5}\mathrm{Nm}^{-1}\mathrm{K}^{-1}$, however, it proved impossible to obtain solutions for current values high enough for this breakdown to occur, since the numerical method failed to converge. The Reynolds numbers of the flows at this point were almost 1000 and thus the flows may be becoming turbulent to some extent, and this could be responsible for the non-convergence of the numerical scheme.

In Chapter 5 a linear stability analysis of the solution obtained in Chapter 4 was presented. The perturbations were given a $\phi$-dependence of the form $e^{im\phi}$ and the solutions were seen to undergo bifurcations at small current values for all values of $\left|\frac{\partial\gamma}{\partial T}\right|$ when m=1. The case m=2 was also investigated, but the basic flow did not lose stability with this mode until higher values of the applied current were used. Ideally the case m=0 should have been done in addition, however the derivation of the equation would have been greatly changed and considerable time whould have been needed to complete this.

Although the hemispherical model does not provide solutions for the current values used in real welding conditions, the loss of stability of the basic flow occurs at such low values of the applied current that, unless this is purely due to the use of the point source, there is some doubt as to the accuracy of any other model which excludes the possibility of azimuthal rotation. It would be instructive to perform a stability analysis for a model with Gaussian distributions for the heat and current sources, to see whether instability occurs at similar current values.

# Appendix A: Linear stability of the similarity solution

Although the spontaneous generation of a rotating flow without a corresponding force to create it has been observed many times, eg. in sink hole flow [ 48 ], there has been no work published analysing the flows generated in the welding problem. In a related MHD problem, Shtern, Goldshtik and Hussain have shown that it is possible it to generate a swirling flow in a conically similar flow without an azimuthal force being present [ 95 ]. They considered the case of the Zeleny-Taylor cone, which is used to model electrosprays, for example, with motion induced by a radial surface tension force. A linear stability analysis showed that a swirling flow is generated when the Reynolds number is large enough. However, if the cone half-angle is taken to be $\pi/2$, ie. a flat plane, to match the weld pool geometry, the generation of the swirling flow no longer occurs.

The appropriate part of the analysis related to the welding problem is presented below. Much of the derivation of the equations is omitted, since it is virtually identical to Chapters 2 and 3.

The velocity is assumed to be given by

$$\mathbf{v} = -\frac{\nu}{r}\left(f'(\mu)\,,\ \frac{f(\mu)}{(1-\mu^2)^{1/2}}\,,\ \frac{l\,(\mu)}{(1-\mu^2)^{1/2}}\right) \tag{A.1}$$

as in Chapter 3, where $l(\mu)$ is now infinitesimal. Unlike Chapter 3 no additional magnetic field is applied, and on substituting (A.1) into the Navier-Stokes equation, and eliminating the term quadratic in l, the following equations are obtained

$$\left(f^2\right)'' = 4f'' + 2\,[f''(1-\mu^2)]'' - \frac{J_0^2\,\mu_0}{\pi^2\nu^2\rho(1+\mu)}\,, \tag{A.2}$$

$$(1-\mu^2)l'' - f\,l' = 0. \tag{A.3}$$

Using the definition (A.1), the stress in the azimuthal direction is given by

$$\sigma_{\varphi\theta} = -\frac{\rho\nu^2}{r^2}\left(\frac{2l\mu}{1-\mu^2} + l'\right). \tag{A.4}$$

Evaluating (A.4) at the top surface, μ=0, the first term in the bracket disappears. This is the important difference between the model for a weld pool, and that of the cone used by Shtern, Goldshtik and Hussain, since for the outer surface being at μ≠0 the first term in (A.4) is still present and the following does not apply.

In model for the weld pool, zero applied stress in the azimuthal direction, leads to the simple condition of

$$l'(0) = 0. \tag{A.5}$$

In order that the azimuthal velocity is finite on the axis μ=1, it follows from (A.1) that

$$l(1) = 0. \tag{A.6}$$

Equation (A.2) is identical to (2.18) and in the same manner as in Chapter 2 can be integrated three times, and simplified by the introduction of a new variable u(μ), defined by

$$f(\mu) = -2(1-\mu^2)\,\frac{u'(\mu)}{u(\mu)}. \tag{A.7}$$

Using this form for f, equation (A.3) becomes

$$(1-\mu^2)l'' + 2(1-\mu^2)\,\frac{u'l'}{u} = 0. \tag{A.8}$$

This can be integrated once with respect μ to give

$$l'u^2 = c, \tag{A.9}$$

where c is the constant of integration. Evaluating equation (A.9) at μ=0, and making use of (A.5), shows that c=0. Since u cannot be zero, because f would then be infinite, $l'$ must be identically zero. Hence $l$ is a constant, and from the boundary condition (A.6), this constant must be zero.

It is therefore not possible to find a transition to a swirling flow using a model based on the similarity solution.

# References

[ 1 ] Nonlinear fluid motions in a container due to the discharge of an electric current
J. Fluid Mech. 1984 v148 p285-300
O.O.Ajayi, C.Sozou and W.M.Pickering

[ 2 ] Liquid metals - chemistry and physics
M. Dekker Inc., New York. 1972 ch4 pp161-212
B.C. Allen (ed. S.Z. Beer)

[ 3 ] American welding society statement
USA Today, 22 March 1992

[ 4 ] Fluid flow in a hemisphere induced by a distributed source of current
J. Fluid Mech. 1978 v84 pp281-290
J.G. Andrews and R.E. Craine

[ 5 ] Fluid flow in a hemisphere induced by a distributed source of current
CEGB report R/M/N919
J.G.Andrews and R.E.Craine

[ 6 ] Nonlinear convection in an imposed magnetic field
Geophys. Astrophys. Fluid Dynamics, 1983 v25 p259-292
W.Arter

[ 7 ] A mathematical model for fluid flow in a weld pool at high currents
J. Fluid Mech. 1980 v98 pp787-802
D.R. Atthey

[ 8 ] A study of vision-based measurements of weld joint shape incorporating the neural-network
Proc. IME, part B, J Engineering Manufacture 1994 v208 pp61-69
K.Y. Bae and S.J. Ny

[ 9 ] An introduction to fluid dynamics
Cambridge University Press, 1967
G.K. Batchelor

[ 10 ] Azimuthal rotation in the axisymmetric meridonal flow due to an electric-current source
J. Fluid Mech. 1983 v126 p413-430
V.Bojarevics and E.V.Shcherbinin

[ 11 ] Electrically induced vortical flows
Kluwer Acad. Pub. 1989
V. Bojarevics, Ya. Freibergs, E.L. Shilova and E.V. Shcherbinin

[ 12 ] Interactions between impurities and welding variables in determining GTA weld shape
Weld. J. 1986 v65 pp150s-155s
P. Burgardt and C.R. Heiple

[ 13 ] Measurement of the force exerted by a welding arc
Met. Trans. 1983 v14A pp1223-1224
T.D. Burleigh and T.W. Eagar

[ 14 ] Magnetohydrodynamics 1975 v11 p395
I.E. Butsenieks, Ya.Yu. Kompan, V.I. Sharamkin, E.I.Shilova and E.V.Shcherbinin

[ 15 ] Magnetohydrodynamics 1976 v16 p70
I.E. Butsenieks, D.E. Peterson, V.I. Sharamkin and E.V. Shcherbinin

[ 16 ] A two-dimensional transient model for convection in laser melted pool
Met. Trans. A 1984 v15 pp2175-2184
C. Chan, J. Mazumder and M.M. Chen

[ 17 ] Hydrodynamic and hydromagnetic stability
Oxford Univ. Press 1968
S. Chandrasekhar

[ 18 ] Universal bifurcation problems
Mechanics of Solids, Rodney Hill 60th Aniversary issue
D.R.J.Chillingworth

[ 19 ] The possible role of turbulence in GTA weld pool behavior
Weld. J. 1994 v73 pp 25s-31s
R.T.C. Choo and J. Szekely

[ 20 ] On determining the shape of weld pools
Appl. Sci. Res. 1987 v40 p261-275
R.E.Craine

[ 21 ] Fluid flow in a hemispherical container induced by a distributed source of current and a superimposed uniform magnetic field
J. Fluid Mech. 1980 v56 pp1-11
R.E. Craine and N.P. Weatherill

[ 22 ] Interaction between standing and travelling waves and steady states in magnetoconvection
Physics Letters A, 1986 v117 no. 8 p394
G.Dangelmayr and E.Knobloch

[ 23 ] The Takens-Bogdanov bifurcation with 0(2)-symmetry
Phil. Trans. R. Soc. Lond. A, 1987 v322 p243-279
G.Dangelmayr and E.Knobloch

[ 24 ] Physical processes in fusion-welding
Reviews of Modern Physics 1995 v67 pp85-112
T. Debroy and S.A. David

[ 25 ] Hydrodynamic stability
Cambridge Univ. Press 1981
P.G. Drazin and W.H. Reid

[ 26 ] On stability for symmetric hyperbolic systems, I
J. Diff. Eqn. 1981 v40 pp94-115
K.S. Eckhoff

[ 27 ] On stability for symmetric hyperbolic systems, II
J. Diff. Eqn. 1982 v43 pp281-304
K.S. Eckhoff

[ 28 ] A simple model for the vacuum arc-remelting process
National Physical Laboratory, DMM(A)61 1992
D.H.Ferriss and P.N.Quested

[ 29 ] Surface tension measurements on pure liquid iron and nickel by an oscillating drop technique
Met. Trans. 1971 v2 pp817-825
M.E. Fraser, W-K. Lu, A.E. Hamielel and R. Murarka

[ 30 ] Linear stability of natural convection in spherical annuli
J. Fluid Mech. 1990 v221 pp105-129
D.R. Gardner, R.W. Douglas and S.A. Trogdon

[ 31 ] Hydrodynaic stability theory
Nijhoff 1985
A. Georgescu

[ 32 ] The use of electrostatic probes to measure the temperature profiles of welding arcs
J. Phys. D 1973 v6 pp1941-1949
A.E.F. Gick, M.B.C Quigley and P.H. Richards

[ 33 ] A paradoxical solution of the Navier-Stokes equation
Appl. Mat. Mech. 1960 v24 pp91-106
M.A. Goldshtik

[ 34 ] Conical flows of fluid with variable viscosity
Proc. R. Soc. Lond. A 1988 v419 pp91-106
M.A. Goldshtik and V.N. Shtern

[ 35 ] Collapse in conical viscous flows
J. Fluid Mech. 1990 v218 pp483-508
M.A. Goldshtik and V.N. Shtern

[ 36 ] Temperature distribution in solids of variable thermal properties heated by moving heat sources
Quart. Appl. Math. 1955 v13 pp161-167
R.J. Grosh, E.A. Trabant and G.A. Hawkins

[ 37 ] Technique for simultaneous real-time measurements of weld pool surface geometry and arc force
Weld. J. 1992 v71 pp 473s-482s
A.C. Guu and S.I. Rokhlin

[ 38 ] Temperature determinations in a free-burning arc: I. Experimental techniques and results in argon
J. Phys. D 1984 v17 pp1189-1196
G.N. Haddad and A.J.D. Farmer

[ 39 ] Centrifugal instabilities of circumferential flows in finite cylinders: linear theory
Proc. R. Soc. Lond. A 1979 v365 pp191-207
P. Hall and P.J. Blennerhassett

[ 40 ] Centrifugal instabilities in finite containers: a periodic model
J. Fluid Mech. 1980 v99 pp575-596
P. Hall

[ 41 ] Effect of selenium on GTAW fusion zone geometry
Weld. J. 1981 v60 pp143s-145s
C.R.Heiple and J.R. Roper

[ 42 ] Mechanisms for minor element effect on GTA fusion zone geometry
Weld. J. 1982 v61 pp97s-102s
C.R.Heiple and J.R.Roper

[ 43 ] Surface active element effects on the shape of GTA, laser and electron beam welds
Weld. J. 1983 v62 pp72s-77s
C.R. Heiple, J.R. Roper, R.T. Stagner and R.J. Aden

[ 44 ] Two-temperature modelling of the free burning, high intensity arc
J. Appl. Phys 1983 v54 pp4359 4366
K.C. Hsu and E. Pfender

[ 45 ] The effect of sidewall imperfections on pattern formation in Lapwood convection
Nonlinearity, 1990 v3 pp197-230
M.D.Impey, D.S.Riley and K.H.Winters

[ 46 ] Elementary stability and bifurcation theory
Springer-Verlag, 1990
G. Iooss and D.D. Joseph

[ 47 ] The effect of plate thickness and radiation on heat flow in welding and cutting
Welding J. 1962 v41 pp12s-16s
P. Jhaveri, W.G. Moffatt and C.M. Adams Jr.

[ 48 ] Formation of a vortex around a sink: a kind of phase transition in a non-equilibrium system
Phys. Lett. A 1978 v68 pp65-66
T. Kawokubo, Y. Tsuchiya, M. Subaya and K. Matsumura

[ 49 ] Surface properties of liquid metals and their effects on weldability
Materials Sci. and Tech. 1985 v1 pp568-571
B.J. Keene, K.C. Mills and R.S. Brooks

[ 50 ] Bifurcation in nonlinear stability
SIAM review 1975 v17 no.4 pp653-683
K. Kirchgasser

[ 51 ] Nonlinear periodic convection in double diffusive systems
J. Fluid Mech., 1981v108 pp921-316
E.Knobloch and M.R.E.Proctor

[ 52 ] Oscillatory and steady convection in a magnetic field
J. Fluid Mech. 1981 v113 pp153-186
E.Knobloch, N.O.Weiss and L.N.DaCosta

[ 53 ] On convection in a horizontal magnetic field with periodic boundary conditions
Geophys. Astrophys. Fluid Dynamics, 1986 v36 p161-177
E.Knobloch

[ 54 ] Welding of thin plates of aluminium alloys - a quantitative heat-flow analysis
Weld. J. 1982 v61 pp175s-181s
S. Kou, T. Kanevsky and S. Fyfitch

[ 55 ] Fluid flow and penetration in stationary arc welds
Metall. Trans A 1986 v16 pp203-213
S. Kou and D.K. Sun

[ 56 ] Machine vision recognition of weld pool in gas tungsten arc welding
Proc. IME, part B, J Engineering Manufacture 1995 v209 pp85-112
R. Kovacevic and Y.M. Zhang

[ 57 ] The stability of meridional liquid flow induced by a gradient of surface tension or electromagnetic forces.
International Institue of Welding, Doc 212-692-87
J.F. Lancaster

[ 58 ] Flow in the weld pool
International Institute of Welding, Doc 212-718-89
J.F.Lancaster

[ 59 ] A stable and accurate convective modelling procedure based on quadratic upstream interpolation
Computer Methods in Applied Mechanics and Engineering, 1979 v19
B.P.Leonard

[ 60 ] On the instabilities of 3-dimensional flows of an ideal incompressible fluid
Physics Letters A 1992 v167 pp465-474
A. Lifschitz

[ 61 ] Instabilities of ideal fluids and related topics
ZAMM 1995 v75 pp411-422
A. Lifschitz

[ 62 ] Influence of arc pressure on weld pool geometry
Weld. J. 1985 v64 pp163s
M.L. Lin and T.W. Eagar

[ 63 ] Power and current distributions in gas tungsten arcs
Weld. J. 1988 v67 pp29s-34s
M. Lu and S. Ku

[ 64 ] Moving boundary problems in heat flow
D. Longworth

[ 65 ] Heat transfer and fluid flow in the welding arc
Met. Trans. A 1986 v17 pp1139-1148
J. McKelliget and J. Szekely

[ 66 ] Effect of electromagnetic stirring on GTA welds in austenitic stainless steel
Weld. J. 1990 v69 pp 52s-59s
M. Malinowski-Brodnicka, G. den Ouden and W.J.P. Vink

[ 67 ] Arc and pool instabilities in GTA welding
Weld. J. 1977 v56 pp133s-139s
J.C. Metcalf and M.B.C. Quigley

[ 68 ] Analysis of a high manganese stainless steel weldability problem
Weld. J. 1977 v56 pp186s-188s
G.S. Mills

[ 69 ] Fundamental mechanisms of penetration in GTA welding
Weld. J. 1979 v58 pp21s-24s
G.S. Mills

[ 70 ] The surface tensions of 304 and 316 type stainless steels and their effect on weld penetration
Report of The National Physical Laboratory, Teddington, Middex. U.K. 1984
K.C. Mills, B.J. Keene, R.F. Brooks and A. Olusanya

[ 71 ] Some problems in magnetohydrodynamics of liquid metals
ZAMM 1978 v58 ppT65-T71
H.K.Moffatt

[ 72 ] Magnetohydrodynamics of conical flows
Phys. Fluids 1971 v14 pp2687-2692
J.P. Narain and M.S. Uberoi

[ 73 ] Fluid motions caused by conical currents
Phys. Fluids 1973 v16 pp940-942
J.P. Narain and M.S. Uberoi

[ 74 ] J. Appl. Phys 1962 v33 pp1638
O.H. Nestor

[ 75 ] Heat- and fluid- flow phenomena in weldpools
J. Fluid Mech. 1984 v147 pp53-79
G.M. Oreper and J.Szekely

[ 76 ] Numerical simulation of incompressible flows with simple boundaries. I Galerkin (Spectral) representations
Studies in Appl. Maths. 1971 v50 no. 4 pp292-327
S.A.Orszag

[ 77 ] Numerical simulation of viscous incompressible flows
Annual Review of Fluid Mechanics 1974 v6 pp281-318
S.A. Orszag and M. Israeli

[ 78 ] Vision-based weld pool width control
Trans. ASME, J. Engineering for Industry 1994 v116 pp86-92
K.A. Pietrzak and S.M. Packer

[ 79 ] A mathematical model of heat conduction in a prolate spheroidal co-ordinate system with applications to the theory of welding
J. Phys. D 1993, v26 pp563-573
N. Poastacioglu, P. Kapadia and J. Dowden

[ 80 ] On the stability, or instability, of certain fluid motions
Scientific Papers of Lord Rayleigh I, pp474-487
Dover, New York 1964
Lord Rayleigh

[ 81 ] A numerical bifurcation study of natural convection in a tilted 2-D porous cavity
J. Fluid Mech., 1990 v215 p309-329
D.S.Riley and K.H.Winters

[ 82 ] Hydrodynamic stability of the melt during the solidification of a binary alloy with small segregation coefficient
Physica D, 1989 v39 pp231-238
D.S.Riley and S.H.Davis

[ 83 ] Long wave morphologies in directional solidification
Appl. Mech. Rev. 1990 v43 no. 5 pt 2 p585
D.S.Riley

[ 84 ] Long-wave morphological instabilities in the direction solidification of a dilute binary mixture
SIAM J. Appl. Maths, 1990 v50 no. 2p 420-436
D.S.Riley and S.H.Davis

[ 85 ] Finite difference methods for the steady state Navier-Stokes equation
Proc. Third Int'l Conf. on Numerical Methods in Fluid Dynamics, Paris, France
July 3rd-7th, 1972
P.J.Roache

[ 86 ] Computational Fluid Dynamics
Hermosa, Albuquerque, 1972
P.J.Roache

[ 87 ] A study of arc force, pool depression and weld penetration during gas tungsten arc-welding
Weld. J. 1993 v72 pp381s-390s
S.I. Rokhlin

[ 88 ] Mathematical theory of heat distribution during welding and cutting
Welding Journal 1941 v20 p220s
D.Rosenthal

[ 89 ] The theory of moving sources of heat and its application to metal treatments
Trans. ASME 1946 v68 pp849-866
D. Rosenthal

[ 90 ] Influence of sulphur and welding conditions on penetration in thin strip stainless-steel
Weld. J. 1995 v74 pp69s-76s
P.R. Scheller, R.F. Brooks and K.C. Mills

[ 91 ] Surface phenomena in metals and alloys
Pergamón Press inc.
V.K.Sememchenko

[ 92 ] Computation of temperatures in thin tantalum sheet welding
Metall. Trans. B 1980 v11 pp257-265
Y. Sharir, A. Grill and J. Pelleg

[ 93 ] A textbook of magnetohydrodynamics
Pergamon Press, 1965
J.A. Shercliff

[ 94 ] Fluid motions due to an electric current source
J. Fluid Mech. 1970 v40 pp241-250
J.A. Shercliff

[ 95 ] Generation of swirl due to symmetry breaking
Phys. Review E 1994 v49 pp2881-2886
V. Shtern, M. Goldshtik and F. Hussain

[ 96 ] Uch. zap. MGU Sci. Rec.
Moscow State Univ, 1934, no. 2 (In Russian)
N.A Slezkin

[ 97 ] On fluid motions induced by an electric current source
J. Fluid Mech. 1971 v46 pp25-32
C. Sozou

[ 98 ] On some similarity solutions in magnetohydrodynamics
J. Plasma Phys. 1971 v6 pp331-341
C. Sozou

[ 99 ] Fluid motions induced by an electric current discharge
Proc. R. Soc. Lon. 1972 A329 pp71-81
C. Sozou and H. English

[ 100 ] Fluid motions induced by an electric current jet
Phys. Fluids 1972 v15 pp272-276
C. Sozou

[ 101 ] MHD flows generated by an electric current discharge
J. Fluid Mech. 1974 v63 pp665-671
C. Sozou

[ 102 ] The development of magnetohydrodynamic flow due to an electric current discharge
J. Fluid Mech. 1975 v70 pp509-517
C. Sozou and W.M. Pickering

[ 103 ] Magnetohydrodynamic flow due to the discharge of an electric current in a hemispherical container
J. Fluid Mech. 1976 v73 pp641-650
C. Sozou and W.M. Pickering

[ 104 ] Magnetohydrodynamic flow in a container due to the discharge of an electric current from a finite size electrode
Proc Roy. Soc. Lond. A 1978 v362 pp509-523
C. Sozou and W.M. Pickering

[ 105 ] Temperature distribution around a moving cylindrical source
J. Heat Transfer 1974 pp427-428
R. Trivedi and S.R. Srinivason

[ 106 ] Electromagnetic-force-induced convection in weld pools with a free surface
Weld. J. 1990 v69 pp241s-246s
M.C. Tsai and S. Kou

[ 107 ] On finite amplitude instability in thermohaline convection
J. Marine Res. 1965 v23 no. 1 p1
G.Veronis

[ 108 ] Magnetohydrodynamic flow in a weldpool
Ph.D. thesis, Southampton, 1979
N.P. Weatherill

[ 109 ] Metals and Materials 1968, Rev 124
D.W.G. White

[ 110 ] Electromagnetic control of fluid motion in TIG weld pools
Proc. Int. Conf. Arc Physics and Weld Pool Behavior 1979 pp361-373
R.A. Willgoss

[ 111 ] The effect of a uniform magnetic field on the onset of steady Benard-Marangoni convection in a layer of conducting fluid
J. Engeneering Maths. 1993 v27 pp161-188
S.K. Wilson

[ 112 ] Fourth order differential equations
Aeronautical Quarterly 1954 v5 pt3 p176
L.C.Woods

[ 113 ] Motion in the weld pool in arc welding
Weld. J. 1971 v50 pp163s-173s
R.A. Woods and D.R. Milner